Role of Abdominal Aortic Aneurysm Wall Biomechanics in Endovascular Repair Assessment

Zinan He

Department of Biomedical Engineering
McGill University
Montréal, Québec, Canada

August 2020

A thesis submitted to the Faculty of Graduate Studies and Research
in partial fulfilment of the requirements of the degree of

Doctor of Philosophy

ABSTRACT

Cardiovascular disease is a leading cause of death around the world (1). In particular, abdominal aortic aneurysm (AAA) is a top silent killer and even claimed the life of our eminent scientist Albert Einstein. Symptoms often only appear in the late stages, and since AAA involves the main artery carrying blood from the heart to the torso, it may trigger catastrophic events such as rupture and coincides with a mortality up to 90% (2). The prevalence in western countries is especially high, around 20,000 patients are diagnosed with AAA every year in Canada (3), and AAA rupture has been ranked the 15th leading cause of death for the past two decades in the United Sates (4). Endovascular repair (EVAR), a minimally invasive AAA treatment, was introduced in the 90's and is considered as a promising option compared to the traditional open surgery. Regardless of the significant reduction in surgical risks and recovery time, no difference has been reported for the long-term outcome, mainly due to graft related complications (5). Therefore, better understanding the biomechanics of AAA, particularly in contact with endovascular devices, will provide an essential path to improve endovascular treatments.

Although the biomechanics of AAA has been extensively investigated, efforts have mostly been devoted to the risks of major AAA characteristics associated with vascular rupture, such as stiffened wall, gigantic thrombus and calcification. The roles of those characteristics during the interaction with endovascular devices remain to be elucidated. Moreover, controversial understanding on the role of calcification (Ca) persists, partly due to its complicated nature and morphological variability, often resulting in oversimplification or exclusion from clinical evaluations. The intrinsic property of Ca has always been considered, however the combined effects of Ca shapes and locations have been questioned but not yet addressed. Besides, most studies have focused on major AAA characteristics, but rarely on the surrounding tissues, such as the abdominal fat despite its high prevalence. Hence, further research on the biomechanical response of AAA during EVAR, taking into account both the major AAA characteristics and the surrounding tissues, is sought.

Consequently, the main objective of this thesis is to provide insight into the role of AAA wall biomechanics, specifically for the aortic Ca and surrounding tissues, in EVAR assessment. A novel quantitative and qualitative analysis, using 3D models reconstructed from clinical data to describe the extent, shape and location of Ca, has been conducted to investigate the effects of Ca morphological characteristics on EVAR outcomes. In addition, a series of hydrogel-based anthropomorphic mockups simulating the mechanical, anatomical and pathological characteristics of AAA have been developed for the first time, in order to evaluate the biomechanical interaction between endovascular devices and AAA, with and without the presence of surrounding abdominal fat. Results from Ca analysis confirmed that, not only the intrinsic properties but also the morphological characteristics of Ca, can together alter the global behavior of AAA, thus playing an essential role in EVAR assessment. Specifically, including the combined effects from Ca morphological characteristics can lead to very different prediction compared to conventional assessment, where the intrinsic property is merely considered. Furthermore, results from AAA mockup analysis highlighted the indispensable role of surrounding tissues, not only the spine but also the abdominal fat, as to account for realistic interactions with endovascular devices. The discoveries and novel approaches within the scope of this thesis have potential clinical significance which, with future revisions and validation, could improve the current knowledge in AAA biomechanics and EVAR assessment.

RÉSUMÉ

Les maladies cardiovasculaires sont l'une des principales causes de décès dans le monde (1). En particulier, l'anévrisme de l'aorte abdominale (AAA) est un tueur silencieux majeur dont les symptômes apparaissent principalement à un stade avancé, ce qui a même coûté la vie à notre éminent scientifique Albert Einstein. Étant la principale artère transportant le sang du cœur vers le torse, l'AAA peut conduire à un événement catastrophique en cas de rupture, avec un taux de mortalité aussi élevé que 90% (2). La prévalence dans les pays occidentaux est particulièrement élevée, environ 20,000 patients reçoivent un diagnostic d'AAA chaque année au Canada (3), et la rupture de l'AAA a été classée au 15e rang des principales causes de décès au cours des deux dernières décennies aux États-Unis (4). La réparation endovasculaire de l'anévrisme de l'aorte (EVAR), un traitement mini-invasif des AAA, a été introduit dans les années 90 est considéré comme une option prometteuse par rapport à la chirurgie ouverte traditionnelle. Indépendamment de la réduction significative des risques chirurgicaux et du temps de récupération, aucune différence n'a été rapportée pour le résultat à long terme, principalement en raison de complications liées à la greffe (5). Par conséquent, une meilleure compréhension de la biomécanique des AAA, en particulier en contact avec les dispositifs endovasculaires, permettra une voie essentielle pour améliorer les traitements endovasculaires.

Si la biomécanique de l'AAA a longtemps été étudiée dans le monde, des efforts ont été consacrés aux risques de caractéristiques majeures de l'AAA (paroi raidie, thrombus gigantesque et calcification) associés à la rupture vasculaire, alors que les rôles de ces caractéristiques lors de l'interaction avec les dispositifs endovasculaires restent à être élucidés. En outre, la compréhension controversée sur le rôle de la calcification (Ca) persiste, en partie en raison de sa nature compliquée et de sa variabilité morphologique, entraînant souvent une simplification excessive ou une exclusion des évaluations cliniques. Il est à noter que la propriété intrinsèque du Ca a toujours été considérée, alors que la question de la combinaison des effets des formes et des emplacements du Ca a été soulevée mais pas encore abordée. En revanche, la plupart des études se sont concentrées sur les principales caractéristiques des AAA, mais rarement sur les tissus environnants, comme la graisse abdominale malgré sa forte prévalence. Par conséquent, des recherches supplémentaires

sur la réponse biomécanique de l'AAA pendant EVAR, en tenant compte à la fois des principales caractéristiques de l'AAA et des tissus environnants, sont requises.

Par conséquent, l'objectif principal de cette thèse est de fournir un aperçu du rôle de la biomécanique de la paroi AAA, en particulier pour le Ca aortique et les tissus environnants, dans l'évaluation EVAR. En tant que tel, une nouvelle analyse quantitative et qualitative, utilisant des modèles 3D reconstruits à partir de données cliniques pour décrire l'étendue, la forme et l'emplacement du Ca, a été menée pour étudier les effets des caractéristiques morphologiques du Ca sur les résultats EVAR. De plus, une série de maquettes anthropomorphiques à base d'hydrogel simulant les caractéristiques mécaniques, anatomiques et pathologiques de l'AAA ont été développées pour la première fois, afin d'évaluer l'interaction biomécanique entre les dispositifs endovasculaires et l'AAA, avec et sans la présence de la graisse abdominale. Les résultats de l'analyse du Ca ont confirmé que, non seulement les propriétés intrinsèques mais aussi les caractéristiques morphologiques du Ca, peuvent ensemble modifier le comportement global de l'AAA, jouant ainsi un rôle essentiel dans l'évaluation EVAR. Plus précisément, l'inclusion des effets combinés des caractéristiques morphologiques du Ca peut conduire à une prédiction très différente par rapport à l'évaluation conventionnelle, où la propriété intrinsèque est simplement considérée. En outre, les résultats de l'analyse des maquettes AAA ont mis en évidence le rôle indispensable des tissus environnants, non seulement la colonne vertébrale mais aussi la graisse abdominale, pour rendre compte des interactions réalistes avec les dispositifs endovasculaires. Les découvertes et les nouvelles approches dans le cadre de cette thèse ont une signification clinique potentielle qui, avec des révisions et des validations futures, pourrait améliorer les connaissances actuelles en biomécanique AAA et en évaluation EVAR.

ACKNOWLEDGEMENTS

First, I would like to express my most sincere gratitude to my supervisors, Prof. Rosaire Mongrain and Dr. Gilles Soulez, for the inspiration of this project, generous support and valuable guidance throughout my years of PhD study. Prof. Mongrain, your creative ideas and confidence in me gave me the opportunity to widely explore and share with the scientific community. Dr. Soulez, your encouragement and patience in guiding me into the clinical research allowed me to gain more knowledge in the field of medicine, shaping this work more clinically significant.

I would also like to acknowledge my supervisory committees, Prof. Richard Leask, Prof. Damiano Pasini, Prof. Satya Prakash and Prof. Robert Kearney, for all their helpful advices. The assistance from Biomedical Engineering Department is also very appreciated, especially from my dearest Pina Sorrini. Finally, my deepest gratitude to Dr. W. Robert J. Funnell, who has not only given me positive impacts intellectually, but more importantly being an invaluable mentor guiding me through the ups and downs of this journey.

From the bottom of my heart, I am forever grateful to my parents, Jiqiang and Lizhen, for their unconditional love, support, encouragement, understanding and believing in me. You are the backbone to my success. I also feel extremely blessed to have my Chinese Medicine Master, Dr. Chan, as well as Dr. Candace Y. W. Lee, being my wishbone and motivating me to always be my best. Last but not least, I am truly grateful to have good friends being my funny bone, especially Victoria, without whom lots of milestones would not have been achieved.

I would also like to thank lots of colleagues or now friends, especially David Roy, Simon Lessard, Boris Chayer, Hossein Mohammadi, Gilbert Jabbour, Dr. Emre Aslan and Dr. William Fortin, for their technical collaborations, inspired conversations and thoughtful suggestions.

CONTRIBUTIONS OF AUTHOR

REFERRED PUBLICATIONS

He Z, Mongrain R, Lessard S, Chayer B, Cloutier G, Soulez G (2020). Anthropomorphic and biomechanical mockup for abdominal aortic aneurysm. *Medical Engineering and Physics*, 77:60-68. DOI: 10.1016/j.medengphy.2019.12.005

He Z, Mongrain R, Lessard S, Soulez G (2017). Extents, locations and geometrical configurations of calcification in abdominal aortic aneurysm. *IFMBE Proceedings*, 65:639-642, DOI: 10.1007/978-981-10-5122-7_160

REFERRED CONFERENCE ABSTRACTS

He Z, Mongrain R, Chayer B, Cloutier G, Soulez G (2018). Tissue-mimicking mockup for abdominal aortic aneurysm – effect of surrounding tissue. *8th World Congress of Biomechanics.* July 8-12, 2018, Dublin, Ireland.

He Z, Mongrain R, Lessard S, Soulez G (2018). A quantitative and qualitative analysis of calcification in abdominal aortic aneurysm. *8th World Congress of Biomechanics.* July 8-12, 2018, Dublin, Ireland.

Mongrain R, **He Z**, Mohammadi H, Frattolin J, Soulez G (2018). Friction characterization between catheters and vascular tissue for Newtonian and non-Newtonian fluids. *8th World Congress of Biomechanics.* July 8-12, 2018, Dublin, Ireland.

He Z, Mongrain R, Lessard S, Soulez G (2018). Morphological analysis of calcification in abdominal aortic aneurysm. 10th *European Solid Mechanics Conference (ESMC2018).* July 2-6, 2018, Bologna, Italy.

He Z, Mongrain R, Chayer B, Cloutier G, Soulez G (2017). Reverse engineering: a tissue-mimicking mockup for abdominal aortic aneurysm. *5th International Conference on Computational and Mathematical Biomedical Engineering (CMBE2017)*. April 10-12, Pittsburgh, USA.

He Z, Mongrain R, Soulez G (2017). Tissue-mimicking mockup (TMM) for abdominal aortic aneurysm (AAA). *65ème Journées Francophones de Radiologie – Diagnostique et Interventionnelle, Congrès International d'imagerie Médicale (JFR2017)*. Octobre 13-16, 2017, Paris, France.

He Z, Mongrain R, Lessard S, Soulez G (2017). Extents, locations and geometrical configurations of calcification in abdominal aortic aneurysm. *17e Congrès Annuel de la Société des Sciences Vasculaires du Québec (SSVQ2017)*. November 24-25, 2017, Québec City, Canada.

He Z, Mongrain R, Soulez G (2016). Tissue-mimicking mockup for abdominal aortic aneurysm. *16e Congrès Annuel de la Société des Sciences Vasculaires du Québec (SSVQ2016)*. November 18-19, 2016, Montréal, Canada.

CONTRIBUTIONS TO ORIGINAL KNOWLEDGE

To date, the roles of calcification (Ca) morphology and surrounding tissues of abdominal aortic aneurysm (AAA) with regards to endovascular repair (EVAR) treatments have not been investigated. The original contributions to the generally knowledge and novel technology, in the context of hypotheses and objectives of this study, are outlined as follows.

First, to the best of the author's knowledge, this thesis presented the first thorough morphological characterization of Ca in AAAs, in terms of their volumes, shapes and locations. Unlike conventional methods in clinical evaluations of vascular Ca, a novel strategy, combining the quantitative analysis using 3D reconstructions from clinical CTs and the qualitative analysis through subsequent classifications of Ca shapes and locations, was proposed. Moreover, it allowed for the first successful attempt to study the combined effects of Ca morphological characteristics on the risk factors of AAA and EVAR complications. Such knowledge also provides a different perspective for the future investigations in AAA pathophysiology, as well as a more comprehensive evaluation of AAA rupture risk. As a result, by considering specific combinations of Ca morphological data, the concerns raised from other clinical studies regarding the influence of Ca in EVAR is confirmed and further refined, which also provides insight to address the debatable role of Ca in AAA.

Second, a novel hydrogel based anthropomorphic perfused mockup for AAA was presented in this thesis. Being mechanically, anatomically and pathologically realistic, this mockup provides an ideal means to reverse engineer the biomechanical interaction of AAA and endovascular devices, while the cross-species and cross-specimen variabilities are eliminated. As such, the indispensable role of surrounding tissues, not only the spine but also the surrounding tissue, was discovered through EVAR experiments with this mockup. Such knowledge provides essential guidelines to refine the current computational models employed to study the biomechanics of AAA, as well as those in surgical planning platforms.

Furthermore, a novel image rendering strategy, as well as two different approaches to include Ca in the anthropomorphic mockup were proposed. Such methodology may not only assist in developing a patient-specific mockup to address questions that are challenging to answer from

clinical studies or numerical simulations, but also provide a valuable guideline to the design of patient-specific medical devices.

In summary, the original contributions from this thesis present potentially important implications to improve the overall quality of AAA evaluations, EVAR planning, as well as outcome predictions.

LIST OF ABBRIVIATIONS

AAA	Abdominal aortic aneurysm
AAC	Abdominal aortic calcifications
ABS	Acrylonitrile butadiene styrene
AMM	Anthropomorphic mockup
BAT	Brown adipose tissue
BMI	Body mass index
Ca	Calcifications
CAD	Coronary artery disease
CAD_{ENG}	Computer aided design (engineering)
CBCT	Cone beam computerized tomography
CKD	Chronic kidney disease
COF	Coefficient of friction
COPD	Chronic obstructive pulmonary disease
CRD	Chronic renal disease
CT	Computerized tomography
DLP	Dyslipidemia
EC	Endothelial cells
EVAR	Endovascular repair
FEA	Finite element analysis
GFR	Glomerular filtration rate

Ha	Hydroxyapatite
HFT	High fat diet
ILT	Intraluminal thrombus
MRI	Magnetic resonance imaging
MV	Matrix vesicles
NYHA	New York Heart Association
OR	Odds ratio
OSR	Open surgical repair
PSI	Percutaneous sheath introducers
PVAT	Perivascular adipose tissue
PVA	Polyvinyl alcohol
PVA-C	Cryogenic polyvinyl alcohol hydrogel
PVD	Peripheral vascular disease
ROI	Region of interest
SG	Stent graft
SMC	Smooth muscle cells
TAA	Thoracic aortic aneurysm
VSMC	Vascular smooth muscle cells
WAT	White adipose tissue
2D	Two dimensional
3D	Three dimensional

LIST OF FIGURES

LIST OF TABLES

TABLE OF CONTENTS

1

INTRODUCTION

Cardiovascular disease remains the leading cause of death around the world (1). In particular, abdominal aortic aneurysm (AAA) is a top silent killer presenting no symptom until late stage. As the main branch delivering blood from the heart to the lower body, rupture of AAA is often fatal with the mortality rate as high as 90% (2). In Canada, it is estimated that 20,000 patients are diagnosed with AAA every year and 1,244 died from it (3). In the United States, aortic aneurysm rupture was ranked the 15th leading cause of death from 1999 to 2015, especially in seniors (4). As a minimally invasive AAA treatment compared to the traditional open surgery, endovascular repaired (EVAR) was first introduced in 1990 and becomes a popular option nowadays. Regardless of the promising evolution in medical technology, the trends in AAA mortality for the past few decades continued to increase in some developed countries (6). Consequently, to better understand the biomechanics of AAA, particularly in contact with endovascular devices, provides an essential path to improve endovascular treatments.

In this Chapter, a brief overview of the main clinical background regarding AAA and EVAR is presented, as well as the treatment limitation manifested by EVAR failures. The current knowledge in AAA biomechanics is summarized, elucidating the blind spots in characterizing the biomechanical interaction between AAA and endovascular devices. The motivation driving the scope of work in this thesis is thereupon defined, with proposed hypothesis and detailed objectives. The outline of thesis is also described at the end of this chapter.

1.1 Rationale

1.1.1 Clinical background

1.1.1.1 Abdominal aortic aneurysm

Abdominal aortic aneurysm (AAA) is characterized by the dilation of abdominal aorta due to progressive wall degeneration, enlarging the aortic artery from its healthy state of 3 cm in diameter to over 10 cm in some severe cases. Surgical treatments are often recommended when the AAA diameter grows beyond 5 cm in females and 5.5 cm in males. The thickness of AAA wall normally falls in the range of 1.5 to 2 mm, and may increase up to 20 mm in the case of inflammation (7). There are two main configurations of AAA: the saccular and the fusiform. Saccular form is often the shape of a pseudoaneurysm, which bulges out only on one side of the aorta as a result of blood filling in between the layers of aortic wall (intima, media and adventitia). Whereas the latter is usually a true aneurysm, which dilates more symmetrically and involves all three layers of the aortic wall (8). The most common location of AAA is below the kidneys, referred to as infrarenal AAA, and may extend distally into the common iliac arteries.

AAA is an asymptomatic condition that can lead to aneurysm rupture which carries an in-hospital mortality rate of more than 50% (9). It has a higher prevalence in Caucasian male over 65 years of age (10). Common risk factors include but are not limited to: smoking, hypertension, obesity, dyslipidemia, coronary artery disease, cerebrovascular disease, peripheral artery disease (11), respiratory disease (12) and some genetic conditions such as Marfan syndrome and Ehlers-Danlos syndrome (13).

Major pathological changes as a results of AAA wall degeneration consist of the weakened aortic wall, the development of intraluminal thrombus (ILT) and calcifications (Ca). A clinical study confirmed that, at the media layer of AAA, the volume fractions of the elastin and vascular smooth muscle cells (VSMCs) decrease by 20.3% and 20.4% respectively, whereas that of the collagen and ground substance increases by 40.2% (14). In fact, the proteolytic process plays an essential role in the pathogenic mechanism of AAA. It not only initiates the media degradation through the elimination of elastin, but also contributes to the disruption of collagen organization

at the adventitia, resulting in a generally weakened aortic wall (15,16). On the other hand, ILT develops in almost 80% of AAA patients owing to the hemodynamically induced damage on endothelial cells and platelet activation (17). It often grows into an inhomogeneous multilayer clot retaining aggregated platelets in a fibrin network, exhibiting various stiffness from the luminal side to the abluminal side (18). By adhering to the aortic wall, thick ILT is believed to impose a hypoxic effect on the underlying wall, thereby triggering subsequent inflammatory and proteolytic mechanisms, weakening the AAA wall. Similar to the ILT, considerable calcifications (Ca) can be found in about 80% of AAAs. Aortic Ca are believed to be initiated from cell death and trans-differentiated from VSMCs (19–25). They are mostly heterogeneously distributed and located in the medial layer near the luminal surface, and occasionally within or lateral to the ILT; Ca are also frequently found in the common iliac arteries (26). An in-depth analysis of the composition, morphology and mechanical property of Ca in AAA has confirmed that the aortic Ca are mainly composed of calcium and phosphorus, similar to hydroxyapatite and appeared as spherical crystals growing along the direction of blood flow (27). Although the severity of Ca has found to be inversely correlated with AAA expansion (28), its role in AAA rupture remains debatable.

1.1.1.2 Endovascular repair

The concept of EVAR was introduced about three decades ago and is now becoming a promising minimally invasive alternative for both patients and practitioners. It prevents AAA rupture by excluding the aneurysm sac through the implantation of stent-grafts (SG). Numerous clinical trials worldwide have investigated the short and long term results between EVAR and open surgical repair (OSR) in AAAs. EVAR has proven to offer better early results in AAAs, particularly within the first two years, but no significant mid and long-term advantage was reported in terms of survival, quality of life and costs (29–32). Consistent data has confirmed that EVAR not only minimizes the time, blood loss, transfusion requirements, morbidity and mortality during operation, but also reduces the length of hospital stay and the need for intensive care. However, higher rates of graft-related complications and secondary interventions were also reported in EVAR (8,33–37). Hence, EVAR is considered as a safer option for patients with higher risk factors, whereas OSR is expected to be a more durable option for young and relatively fit patients, which is a less common scenario (38–41).

The quality of EVAR is strongly depending on careful evaluation on the patient's vascular anatomy, appropriate implant selection and procedure planning. The first major failure of the EVAR approach occurs during the delivery stage, where the access of catheter is limited by the hostile anatomies at the distal end of AAA and the common iliac arteries, increasing the risk of vessel injuries during delivery (8). Not only the vessel diameter and tortuosity, but also the degree of Ca and ILT are critical to both successful device navigation and adequate distal sealing (42). More recently, EVAR is advanced to an even less invasive level owing to a percutaneous access technique, where the degree of Ca has been reported the key for success, as percutaneous catheterization and the use of closure device can be difficult with the presence of Ca at the anterior vessel wall (43–45).

The second major failure occurs during the deployment stage, where the SG cannot be landed and adhered properly on the AAA attachment site. In general, Ca, ILT, the angulation at attachment sites and the vessel tortuosity are important factors to be evaluated before EVAR (46). Anatomical fit between the SG and AAA is an essential criterion for a successful EVAR (42). A tight seal between the SG and attachment site is required to avoid complications such as endoleak, endotension and SG migration (47). Severe neck Ca has already been associated with a higher rate of endoleak (48,49). Type I endoleak corresponds to the failure of the circumferential seal at either the proximal or distal side of the SG, causing direct perfusion to the aneurysm sac and higher risk of rupture. Unfavorable neck anatomies such as angulation and significant Ca are thought to have important contributions for developing type I endoleak (50–52). On the other hand, ILT with its softer nature may provide a snugger adhesion between the vessel wall and SG.

The third major failure occurs after the operation, either in short or long-term, such as SG kinking or thrombosis, SG migration and failure of AAA sac shrinkage, which may lead to AAA or SG rupture (53). Ca in the aneurysm wall has long been speculated to be a contributing factor for failure in aneurysm shrinkage, especially in the case of complete circular Ca in the outer wall of AAA (54–56). Considering endotension, having persistent pressure inside the aneurysm sac after EVAR, has been used to explain the failure of sac shrinkage, it is therefore suggested that Ca may also promote endotension (57).

1.1.2 Biomechanics of AAA

The scientific community has conducted a considerable amount of studies, both experimentally and numerically, to better understand the biomechanics of AAA, with the main focus on the roles of aortic wall, ILT and Ca. Albeit the high rate of obesity in AAA population, which imposes a non-trivial condition to withstand the global deformation of AAA, study on the role of soft tissue surrounding the AAA remains very limited (58,59).

Progressive medial degeneration is an important predisposing factor for AAA, which may induce extensive loss of VSMCs and elastin, compromising the elasticity of the aortic wall (60). In addition, the significant increase of collagen fibre and ground substance in the media layer also reduces the distensibility of the aortic wall (14). The assumption of neglecting viscoelasticity in AAA modelling is therefore justified (61,62). On the other hand, at the adventitia which bears most of the load and restricts aneurysm expansion, collagen degeneration directly hampers the tensile strength of the aortic wall, making it more susceptible to rupture (15).

At abdominal aortic bifurcations, pulse waves can create an amplified echo which promotes vascular dilation (63). Subsequently, flow stagnation, blood recirculation, low wall shear stress and platelet aggregation in that region may trigger the formation of ILT (64). As described earlier, the ILT is an inhomogeneous, non-linear elastic and isotropic material, it consists of multiple layers in which the luminal side is the stiffest with the Young's modulus up to 0.54 MPa (65). However, numerical models of the ILT are often simplified as homogeneous and linear elastic material with Young's modulus of 0.11 MPa (66). Thus far, researchers have not yet reached a consensus on the biomechanical effect of ILT. Some believe that the ILT provides a protective effect as a pressure shield decreasing wall stresses (67,68), whereas others argue that the porous nature of the ILT allows blood flow and pressure to be transmitted, reducing the cushion effect (62,69). Further study in the porosity and permeability of ILT may help clarify this topic.

Calcified deposits in the aortic wall act as geometric singularities that create heterogeneity in the wall structure, the resulted stress concentration may greatly affect the mechanical behaviour of AAA wall. Patient-specific finite element analysis (FEA) and fluid structure interaction (FSI) models have been developed by researchers worldwide to investigate the biomechanical effect of

Ca on AAA; however, results remains controversial. Some discover that Ca increases peak wall stress and imposes strong stress gradient propagating around the Ca, thereby claiming Ca as a stress concentrator, increasing both AAA rupture risk and challenge in EVAR (27,67,70,71). Whereas others reveal that Ca provides a load-bearing effect to the adjacent wall, especially large plaque-like Ca can stabilize the aneurysm wall (72,73). One potential reason for these contradicting interpretations is the wide range of mechanical strength in aortic Ca. Depending on the density and the location of Ca, its elastic modulus has a range from 4 to 450MPa (73–76), and even up to 22 GPa in the extreme case (27). Although mechanical properties of Ca may be of critical importance to the wall stress analysis, relevant experimental measurements remain very limited. Another reason is the characterization of Ca-wall interface, which may differ from one study to another. Finally, as all current numerical studies are done with a relatively small population, where the large variation in Ca shapes and locations among those patient-specific cases may result in biased analysis. Nevertheless, neglecting large Ca in AAA modelling may lead to crucial errors is commonly agreed.

1.1.3 Summary

The pathophysiology and the biomechanics of AAA, especially with the focus on stiffened aortic wall and ILT, have been well characterized over the past decades. This serves as a backbone to improve diagnosis and to drive the evolution of corresponding medical treatments. However, current failures in EVAR reflect our inadequate knowledge about the biomechanical interaction between AAA and the endovascular devices. Although Ca possesses a high prevalence in AAA population, its complicated nature manifested through morphological variability renders the proper assessment on the biomechanical role of Ca very difficult. As such, this essential element remains often omitted or over simplified in clinical evaluation and academic investigation. To date, scientific research has been mostly focused on the intrinsic properties of aortic Ca, whereas the question of considering the combined effect of Ca shapes and locations has been raised but not yet addressed. To our knowledge, although computational models may provide important guidelines for strategic planning in EVAR, limitations such as proper material characterization and the consideration of surrounding tissues persists. Further study on the biomechanical responses of AAA during EVAR, taking both major pathological characteristics and the surrounding tissues into account, is sought.

1.2 Hypothesis and objectives

The motivation behind the work of thesis is to better understand the role of wall biomechanics, specifically the aortic Ca and surrounding tissues, in EVAR assessment. One hypothesis is that not only the intrinsic properties of Ca, but also the morphological characteristics of Ca (volume, location and geometrical configuration), together alter the global behavior of aortic wall and play an essential role in EVAR assessment. It is also hypothesized that incorporating the surrounding tissues improves the estimation of AAA deformation during EVAR.

The global objective of this study was to gain more knowledge, via clinical and experimental means, about the biomechanical effects of aortic Ca and surrounding tissues during EVAR treatment. Such knowledge could provide insight to refine the current computational models employed in surgical planning platforms and better predict complications, improving the overall quality of EVAR. As such, two sets of objectives are determined as follows.

- Conduct a quantitative and qualitative analysis of aortic Ca from clinical data. Describe the morphological characteristics of aortic Ca in terms of the extent, locations and geometrical configurations. Define models representing the most common and severe scenario of aortic Ca. Correlations between these morphological characteristics and AAA risk factors, as well as EVAR complications are sought. Develop simplified FEA models to elucidate the combined effects of Ca morphological characteristics on the wall biomechanics.
- Develop a series of anthropomorphic mockup (AMM) well representing the mechanical, anatomical and pathological characteristics of AAA, with and without the surrounding tissues. Evaluate the quality of catheter navigation and SG implantation with those AMM. Investigate the effects of surrounding tissues on EVAR assessment during pre-delivery and deployment stages.

1.3 Outline of the thesis

In Chapter 2, relevant clinical background, namely the pathophysiology of AAA and the evolution as well as complications of EVAR, is presented. A thorough literature review on the clinical, experimental and numerical studies of AAA wall biomechanics, with more focus on the aortic Ca and surrounding tissue, is also provided. The limitations on our current knowledge is summarized at the end of the chapter, followed by the areas to be improved towards a better understanding of the biomechanical interaction between AAA and endovascular devices.

Chapter 3 presents the quantitative and qualitative analysis of Ca performed to address the first set of objectives. Specifically, patient selection criteria and the methodology to collect relevant comorbidities and EVAR complications are explained. An overview on the current methods to quantify Ca in human vessel is also provided, followed by a detailed description of the segmentation and quantification method proposed for this study. The statistical analysis performed to characterize the morphological characteristics of Ca, and to illustrate correlations between those characteristics and the risk factors of AAA as well as EVAR complications is discussed. Simulations with simplified FEA models to investigate the combined effect of Ca volume and shape are presented, results and implications are also discussed.

Chapter 4 covers the development of AMM and the corresponding EVAR experiments, where the second set of objectives are fulfilled. An overview of the hydrogel selected for this AMM is presented, followed by a detailed description of the design concepts, material properties evaluations and adjustments, main challenges during the AMM development. EVAR experiments with this AMM to evaluate the biomechanical effects of surrounding tissues is described. The method applied to measure positions of endovascular devices is reported, and experimental results are also compared with clinical data to elucidate the effects of surrounding tissues.

Chapter 5 presents the proof of concept study for a patient-specific AMM. Specifically, a specific strategy to create 3D native smooth surfaces from 2D coarse clinical scans, revisions in mold design and development, as well as different approaches to develop calcified PVA-C hydrogel are described.

Finally, Chapter 6 summarizes the results of Ca analysis and AMM experiments, followed by a general discussion on those findings. The original contributions in knowledge as well as the technological novelty are emphasized. Limitations and challenges throughout the scope of work is discussed, and the directions for future endeavors are outlined.

2

BACKGROUND

This chapter presents both the clinical and biomechanical background related to the thesis. First, the pathophysiology of AAA is overviewed, specifically the anatomy, morphology, classification, demographics and major pathological characteristics. A review of AAA treatment options is followed, with an emphasis on EVAR evolution and treatment complications. Besides, current knowledge in biomechanics regarding the AAA wall, ILT, Ca and surrounding tissues is presented. In addition, tissue mimicking mockups developed to investigate the biomechanical role of AAA are described. At the end this chapter, limitations in the current knowledge are summarized, which conjointly contribute to the main motivation of the research.

2.1 Pathophysiology of AAA

Human vascular walls regularly remodel through a well-balanced mechanism combining the synthesis, degradation, damage repair of the extracellular matrix, to maintain its structural integrity and normal functionality. As such, any alterations during vascular remodeling may compromise the structure or function of the connective tissue, weaken the vascular wall and create aneurysm. AAA is a pathological condition commonly associated with abdominal aortic wall degeneration, resulting in a weakened wall that continues to dilate overtime, along with the development of intraluminal thrombus and calcifications in the enlarged aorta.

2.1.1 Anatomy of healthy abdominal aorta

The same as all arterial structures, the abdominal aorta has three layers: intima, media and adventitia, as shown in Figure 2.1 (77). The intima is the thinnest layer with a layer of endothelial cells; it is the inner-most layer. The media is composed of abundant smooth-muscle cells, elastin, collagen and proteoglycans; it provides a decent elasticity for the arterial wall to contract and expend in a healthy rhythm over each cardiac cycle. Specifically, elastin acts as a load bearing element to resist aneurysm formation, and collagen strengthens the vessel to prevent aneurysm ruptures. As a result, medial degeneration may damage these proteins and promote AAA formation. The adventitia, the outer layer, consists mainly of collagen, fibroblasts, a variety of cells for immunomodulation and adrenergic nerves; it is responsible to maintain structural integrity and provide additional support to the aorta (78).

As the main artery supplying blood to most of the major organs, abdominal aorta begins from the diaphragm and distally extends to the iliac bifurcation in the lower abdominal region. The diameter of aorta decreases from its thoracic portion (averaged 2.8 cm) to its abdominal portion (averaged 2 cm; normally, women smaller than men (79)). In addition, a reduction (~58% less) in the amount of elastin and collagen is seen in the medial layer of the abdominal aorta compared to the thoracic aorta (79). These anatomical characteristics together may increase the mechanical tension in the aortic wall, making the abdominal aorta more susceptible to aneurysmal diseases (compare to the thoracic aorta).

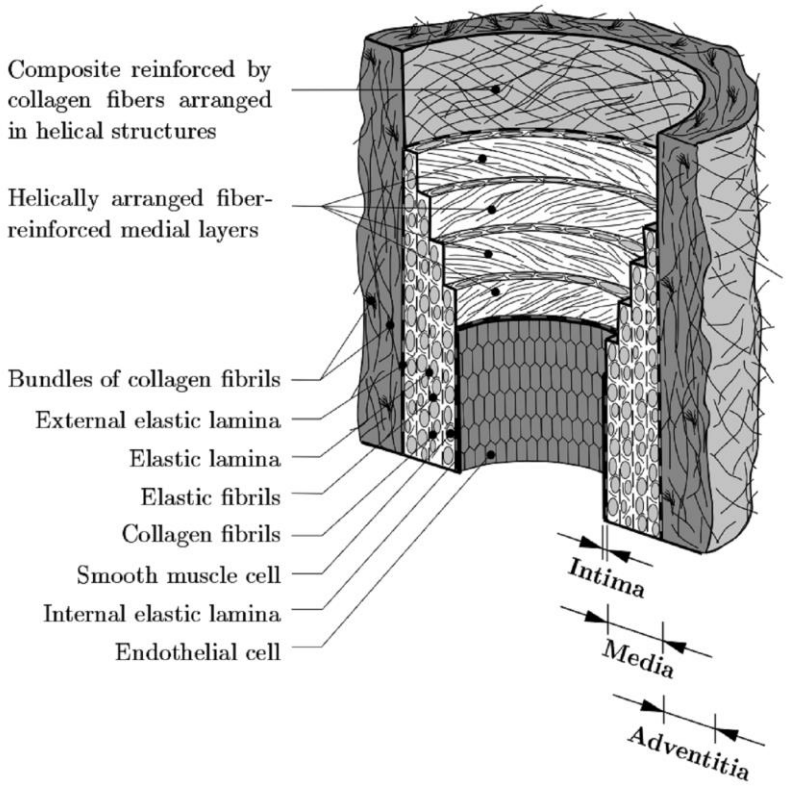

Figure 2.1: Histological composition of the aortic wall.
(Image source: Gerhard A. Holzapfel et al., 2000 [77])

Another interesting anatomical feature of abdominal aorta that may contribute to the etiology of aneurysm is the reduced number of vasa vasorum in this region. Being a network supplying blood and nutrients to large vessels, the vasa vasorum normally surrounds and penetrates the adventitia, and further extends into the media. However, it has been reported that the vasa vasorum appears absence in the media of human abdominal aorta (80,81), decreasing essential nutrient and oxygen supply to the abdominal aortic wall. Consequently, this avascular region exhibits high propensity for atherosclerosis which often relates to the development of AAA, suggesting that the blood supply from vasa vasorum may have a protecting role against aneurysm formation (82,83).

2.1.2 AAA morphology & classifications

An aneurysm is a localized abnormal dilation of a blood vessel that can be either congenital or acquired, potentially leading to catastrophic consequence once it is ruptured. Aneurysms can be found not only along the vascular network, such as the aorta (thoracic and abdominal), vessels in the brain, heart, kidneys and legs, but also inside the heart (ventricular aneurysm). About 90% of

AAAs are located below the renal arteries and above the aortic bifurcation, called infrarenal AAA, and may extend distally into the common iliac arteries and form smaller aneurysms (79). Due to this common location of AAAs, the renal arteries as well as the superior and inferior mesenteric arteries can be occasionally affected by direct extension of aortic wall or by the occlusion of those vessel ostia with thrombus (84).

The abdominal aorta is considered an aneurysm when its diameter increases at least 50% over the normal range, specifically, greater than 5 cm and up to 20 cm in the severe case (84). Most AAAs grow at a rate of 0.2~0.3 cm/year, whereas about 20% of all AAAs can grow faster. The risk of rupture is directly proportional to the size of the AAA. For AAAs with diameters varying less than 4 cm, between 4 to 5 cm, 5 to 6 cm, and greater than 6 cm, the corresponding risks of rupture are 0%, 1%, 11% and 25% per year (84). AAA is a pathological condition associated with the weakening and degeneration of the abdominal aortic wall, particularly within the tunica media. The thickness of AAA wall normally falls in the range of 1.5 to 2 mm, which may increase up to 20 mm in the case of inflammation (85).

Aneurysms are often classified according to their macroscopic shape (Fig. 2.2): saccular or fusiform (84). In saccular aneurysms (Fig. 2.2 B), only a portion of the vessel wall locally bulges out and hence giving a spherical shape; intraluminal thrombus can be often found in this type of aneurysm. In fusiform aneurysms (Fig. 2.2 C), the vessel wall is dilated in a circumferential manner over a relatively long vascular segment. The length of resulting “spindle shape” AAAs varies up to 25 cm as it may involve great portions of the descending and abdominal aorta, as well as the iliac arteries (84). A true aneurysm involves all layers of the vessel wall that are becoming thinned but remain relatively intact, which is always seen in fusiform AAAs. In contrast, a false aneurysm (Fig. 2.2 D), also called pseudo-aneurysm, occurs when there is a defect in the vessel wall resulting in a collection of blood (hematoma) bounded externally by extravascular connective tissues. Of note, this is not rare in saccular AAAs where not all layers of the aortic wall are dilated (8). As a consequence, vascular dissections (Fig. 2.2 E) can happen while the blood tears the intima and separates the vessel layers overtime. This type of aneurysm is usually caused by trauma that punctures the vessel wall, for example during the percutaneous surgical procedure or vascular grafting. Note that regardless of the variations in morphology, these classifications do not correspond to any specific disease or clinical manifestation (84).

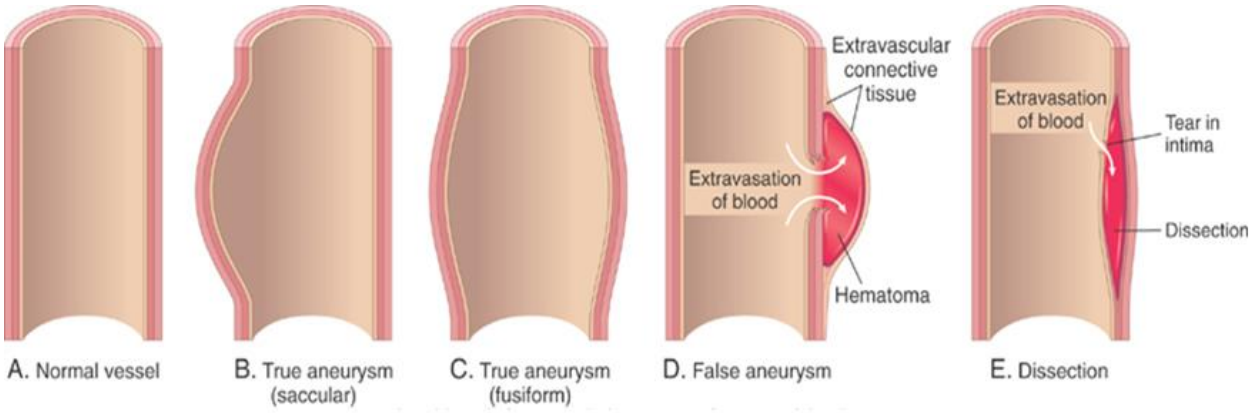

Figure 2.2: AAA classifications according to shapes.

(Image source: Vinay Kumar et al., 2015 [84])

In general, most AAAs exhibit atherosclerotic characteristics which not only compromise the structural integrity of the aortic wall, but also contribute to attenuation of the aortic media. Besides, three other types of AAAs with unusual features are discussed as follows (84).

- *Inflammatory AAA*

  This type of AAA particularly occurs in young patients, accounting for 5-10% of all AAAs. Its clinical manifestations include back pain and elevated inflammatory markers in the plasma. Scaring in the aortic wall may develop in this case, as a result of inflammation with abundant macrophages, which can also extend into the retroperitoneum. The cause is thought to be the localized immune response to a specific location of the aortic wall.

- *Immunoglobulin G4 (IgG4) Related Disease*

  This is a subset of inflammatory AAAs, but with excessive level of IgG4 and signs of frequent infiltration of IgG4-expressing cells in the plasma. This disorder can affect other tissues (salivary gland, biliary system and pancreas) and often cause aortitis and periaortitis, weakening the aortic wall and eventually lead to aneurysm. Fortunately, it responds well with steroid therapy, hence recognition of such disorder is important.

- *Mycotic AAA*

  Lesions infected by the circulating microorganisms in the vessel wall, the adjacent suppurative process or a septic embolus, may all give rise to this type of AAAs. As the

media is further destroyed by suppuration, aortic wall dilation may be accelerated, increasing the risk of rupture.

2.1.3 Demographic & comorbidities

With the increasing prevalence and high propensity for vascular rupture, AAA is a leading cause of death worldwide. However, it is often asymptomatic and discovered incidentally due to a pulsating abdominal mass during physical exams or diagnostic imaging (ultrasonography). Typical clinical presentations of AAAs include the followings.

- Obstruction of the branching vessels along the AAA, causing ischemic injury to the supplied organs (kidney, gastro-intestinal tract) and body parts (legs, spinal cord)
- Impingement on an adjacent tissue (ureter compression, vertebrae erosion)
- Embolism from ILT or atheroma
- Rupture into peritoneal cavity or retroperitoneal tissue, leading to severe hemorrhage

Major risk factors associated with AAA include age, gender, tobacco use and ethnicity (11). The risk of AAA is 4~6 times higher in men than women, with the prevalence increases by 2%~4% per decade after 60 years of age; it is most frequently found in Caucasian ethnicity. Smoking is the strongest risk factor, the prevalence of AAA increases with the number of years of tobacco use and decreases with the number of years after quitting smoking (86).

On the other hand, a positive family history, hypertension and atherosclerosis are also considered important predisposing factors for AAA(11). It has been demonstrated that the risk of AAA is elevated by 66% for patients with hypertension (87). Although it remains unclear whether the association between atherosclerosis and AAA is a result of common risk profiles, the incidence of coronary artery disease (CAD) in AAA patients ranges from 27% to 53% (88). Moreover, medical treatments to manage dyslipidemia has been suggested to reduce the risk of asymptomatic AAA (11). In the contrary, other atherosclerosis associated epidemiology such as diabetes mellitus and peripheral artery disease (PAD), are negatively associated with the AAA growth despite a positive correlation with the AAA presence (89). Chronic kidney disease (CKD), as another

common risk factor for atherosclerotic cardiovascular pathology, is also positively correlated to the presence of AAA and potentially AAA growth; however, further investigation is required in the pathophysiological pathways linking CKD to AAA (90). As smoking being a major risk factor for both AAA and chronic obstructive pulmonary disease (COPD), their association has long been in question. Increased prevalence of COPD in AAA patients, independent from smoking status, has been demonstrated; however, the incidence of COPD often remains underdetermined in AAA patients, because symptoms such as shortness of breath are usually unnoticed in elderly patients due to low physical activity (91). Finally, other less common factors causing AAA include infections, trauma, anastomotic disruption, cystic medial necrosis, congenital defects and genetic predisposition (11).

In addition, since AAA may also occur when the structure or function of connective tissues within the vessel wall is deteriorated by inherited connective tissue disorders, some typical cases are further discussed below (84).

Poor intrinsic quality of connective tissue

- Marfan syndrome is a common example of genetic disorder that affects connective tissue. The mutation in FBN1 gene causes either dysfunctional or less abundant fibrillin, resulting in fewer functional microfibrils in the certain connective tissues, which compromises the elasticity, integrity and strength of tissues, and ultimately promotes progressive vessel dilation (84).

- Loeys-Dietz syndrome is another example of this kind, where the TGF-beta receptors mutate and undergo defective synthesis of elastin and collagens I and III, making the aneurysms more prone to rupture even in small diameters.

- Ehlers-Danlos syndrome in the vascular form is another great example with poor vessel wall because of defective synthesis of collagen III.

- Vitamin C deficiency is an example in the nutritional aspect, which alters collagen cross-linking and facilitate aneurysm development.

2.1.4 Pathology

The pathogenesis of AAA is complicated and not yet fully understood. It is believed to involve multi-factorial mechanisms which still remain to be elucidated. Many of these aspects involve very complex biological pathways and still require extensive evaluations in experimental, animal and clinical studies.

2.1.4.1 AAA formation & development

AAA is often characterized by the thinning of vessel wall due to the loss of smooth muscle cells in the aortic media, the destruction of elastin and collagen, as well as the infiltration of lymphocytes and macrophages in both media and adventitia.

Atherosclerosis is originally considered an inciting factor for AAA formation as it may mechanically weaken the aortic wall, by decreasing elastic recoil and inducing ischemic degenerative response on the aortic wall. Although atherosclerosis is the most common underlying feature associated with AAAs, clinical evidences have shown that AAA and atherosclerosis do not always co-exist (92). On the other hand, atherosclerosis can be widespread throughout the vasculature but affects primarily the intima, whereas AAA only developed at specific locations in certain individuals but affecting both the media and the adventitia; it further implies that atherosclerosis may be a risk factor but absolutely not the main driving force in AAA formation.

Progressive medial degeneration is another important predisposing factor, which may incur extensive loss of vascular smooth muscle cells (VSMCs) and elastins in the aortic wall (60). It is further confirmed by He and Roach (14) from a clinical study over eight AAA that the volume fractions of the elastin and VSMCs decrease 20.3% and 20.4% respectively, whereas that of the collagen and ground substance increases 40.2%. The significantly loss of VSMCs and elastins compromises the vascular elasticity in AAA wall (61,93,94).

Although the primary triggering factor is still undetermined, it is clear that genetic predisposition exists, and that AAAs develop subsequent to medial degeneration which widens the lumen and deteriorates the structural integrity. A variety of other factors are therefore believed to collaborate and weaken the aortic media. Apart from the risk factors for general aneurysm

development that are mentioned in the previous sections, other biological factors contributing to AAA formation include: loss of elastin and collagen in the media and adventitia, smooth muscle cells apoptosis and necrosis, neovascularization, inflammation-induced lymphocytes and macrophages infiltration. Combining the current multidisciplinary knowledge of AAAs, four key mechanisms are identified as follows for the formation and progression of AAA (95).

I. Proteolytic Degradation of Aortic Wall

AAA formation involves a complicated proteolytic process which mainly degrades the aortic media, as well as the supporting lamina. This process, being well-balanced with the activities of proteolytic inhibitors, is indeed essential to maintain regular aortic wall remodeling. In AAAs, the expressions of some proteases are reported significantly higher than those of the proteolytic inhibitors, which favor the degradation of elastin and collagen, decreasing both elasticity and tensile strength of the aortic wall. These protease are mostly secreted from aortic smooth-muscle cells and macrophages into the extracellular matrix. However, the biological mechanisms that shift the balance towards proteolytic activity and encourage AAA development remain unclear.

Matrix metalloproteinases (MMPs), is a typical example of the proteases that involve in AAA formation, where pharmacological use of tissue inhibitors of MMPs (TIMPs) have proven to suppress AAA formation in animal studies. Another example of those proteases is the cysteine protease (cathepsin S, K and L), which are highly expressed in human AAAs and often known as elastolytic enzymes.

II. Inflammation & Immune Responses

Degradation of the aortic wall can induce the release of certain inflammatory factors, resulting in further inflammation in the aorta. Histologic analysis of AAAs confirms a chronic inflammatory infiltration of macrophages and lymphocytes in both media and adventitia, subsequently triggering the release of some inflammatory cytokines. These cytokines then activate smooth-muscle cells to secrete MMPs and further allow proteolytic degradation in the aortic wall.

Besides, the presence of immunoreactive proteins, considerable infiltration of lymphocytes, monocytes and dendritic cells into the abdominal aortic wall, all suggest again the existence of a

chronic immune response, which further support the hypothesis that AAA formation is in fact an autoimmune response. Certain bacterium which stimulate the synthesis of similar immunoreactive proteins are also reported in up to 55% of AAAs, implying an infectious cause in AAA formation and development.

Two shear-induced signaling molecules, nitric oxide (NO) and reactive oxygen species (ROS), are also considered to play an important role in the formation and progression of AAAs.

- NO is responsible for cellular signaling in many physiological and pathological pathways such as immune response and vascular remodeling (96). Increasing evidences have indicated that NO triggers a cascade of vascular degradation and then facilitate the formation of AAAs (97); in contrast, inhibition of NO expressions can restrict the expansion of AAA regardless of the presence of other risk factors (98).
- ROS has shown to activate MMPs which further promote matrix degradation in in-vitro studies. Besides, ROS also affects cell apoptosis and decreases the density of smooth muscle cells, compromising the structural integrity of aortic wall and facilitating AAA formation. All these observations together, suggest that oxidative stress is a crucial factor in AAA development (99).

Since male gender is an important characteristic in AAA population, the anti-inflammatory effects of estrogen is discovered to downregulate the expression of certain cytokines and chemokines, attenuating inflammations and the subsequent pathways towards aortic wall degradation, thereby protecting females from AAA formation. This notion can be verified by the similar risks of developing AAAs in both genders after the age of menopause.

III. Biomechanical Factors

Biomechanical factors such as the reduction in wall elasticity and strength, the variation in wall shear stresses due to disordered flow, elevated circumferential stretch at the bifurcation, are believed to greatly affect AAA formation, progression and even rupture (100). Along the aorta from its proximal (aortic arch) to distal (abdominal aorta) end, the followings have been discovered.

- The number of elastin layers as well as the content of elastin and collagen decrease, rendering the abdominal aorta more susceptible to dilation than the thoracic aorta.
- The vasa vasorum gradually ceases at the level of renal artery, and becomes completely absent in the media of abdominal aorta, leading to hypoxia of the aortic tissue which ultimately favors medial degeneration.
- Pulse waves around the bifurcation may greatly amplify the echo, resulting in higher circumferential tensile stretch and disturbed wall shear stresses, both promoting vascular dilation and atherogenic degeneration around the abdominal aorta (63,101).
- More MMP expressions are usually found in the abdominal aorta than the thoracic portion, implying a higher risk of vessel degradation in this region; of note, higher MMP activities are also believed to be the result of increased wall tension.

Keeping in mind that ROS and NO are two shear-induced molecules closely associated with the formation and progression of AAAs. Experimental evidences suggest that regular flow patterns reduce the production of ROS and increase the bioavailability of NO, providing an anti-atherogenic environment and thus lower the risk of AAA formation (102).

IV. Molecular Genetics

Family history has always been considered as a risk factor for AAA, with approximately 15% of AAA patients demonstrating positive family history, therefore genetic factors undoubtedly

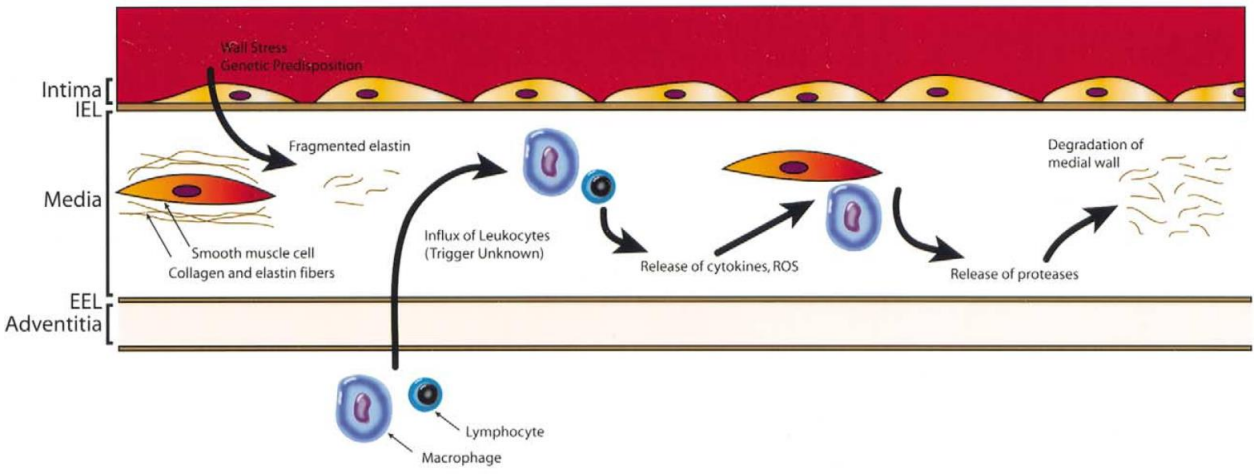

Figure 2.3: Proposed mechanism of AAA formation. (IEL: internal elastic lamina; EEL: external elastic lamina.)
(Image courtesy: B. S. Knipp, MS, University of Michigan Medical School, Ann Arbor)

contribute to the development of AAAs. Beside the common genetic factors involved in inherited connective tissue disorders (discussed in previous sections), two specific loci (on chromosomes 19q13 and 4q31) also display high susceptibility. Nevertheless, not a single genetic polymorphism or defect has yet been nominated as a candidate inducing AAA formation.

Finally, a potential mechanism has been proposed (Fig. 2.3), summarizing from our current understanding of AAA formation and development (92). First, a variety of factors, such as the genetic predisposition, the medial protein fragmentation, the biomechanical stress due to localized hemodynamic effects, all combine and trigger the infiltration of inflammatory cells into the aortic wall via a complex immunologic mechanisms. Cytokines, chemokines and ROS are then released from those inflammatory cells and activate a sub-cellular pathway, further attracting leukocytes influx. This gives rise to a subsequent expressions and activations of proteases (MMPs and cathepsin) which promote medial degradation, aneurysmal dilation and ongoing vessel remodeling. The AAA continues to dilate as the elevated wall stress can intensify proteolytic degradation, eventually leading to AAA rupture if remains untreated. Therefore, pharmacological treatments incorporating the effects from anti-oxidant, anti-inflammatory and anti-proteolytic drugs into cholesterol, hemostasis, or blood pressure control are generally recommended to reduce the progression of AAA.

2.1.4.2 Intraluminal Thrombus

Blood flow stagnation, recirculation zones, low wall shear stress, excessive proteolytic activity, platelet aggregation and subsequent thrombogenic reaction may together trigger the formation of intraluminal thrombus (ILT) (64), which deteriorates both structural integrity and functions of the abdominal aortic wall. ILT is present in 70%~80% of AAAs (18) and normally covers the aortic wall without precluding blood flow, slight compression on the wall can still be seen through a cardiac cycle. Nevertheless, rare event such as complete vessel occlusion instead of mural thrombosis could be fatal.

ILT is structurally complex and widely varies in size and shapes. In general, it is a biologically active neo-tissue laminated in approximately three layers (luminal, medial and abluminal) of poorly organized materials (Fig. 2.4 A&B). The red color in the luminal layer indicates a

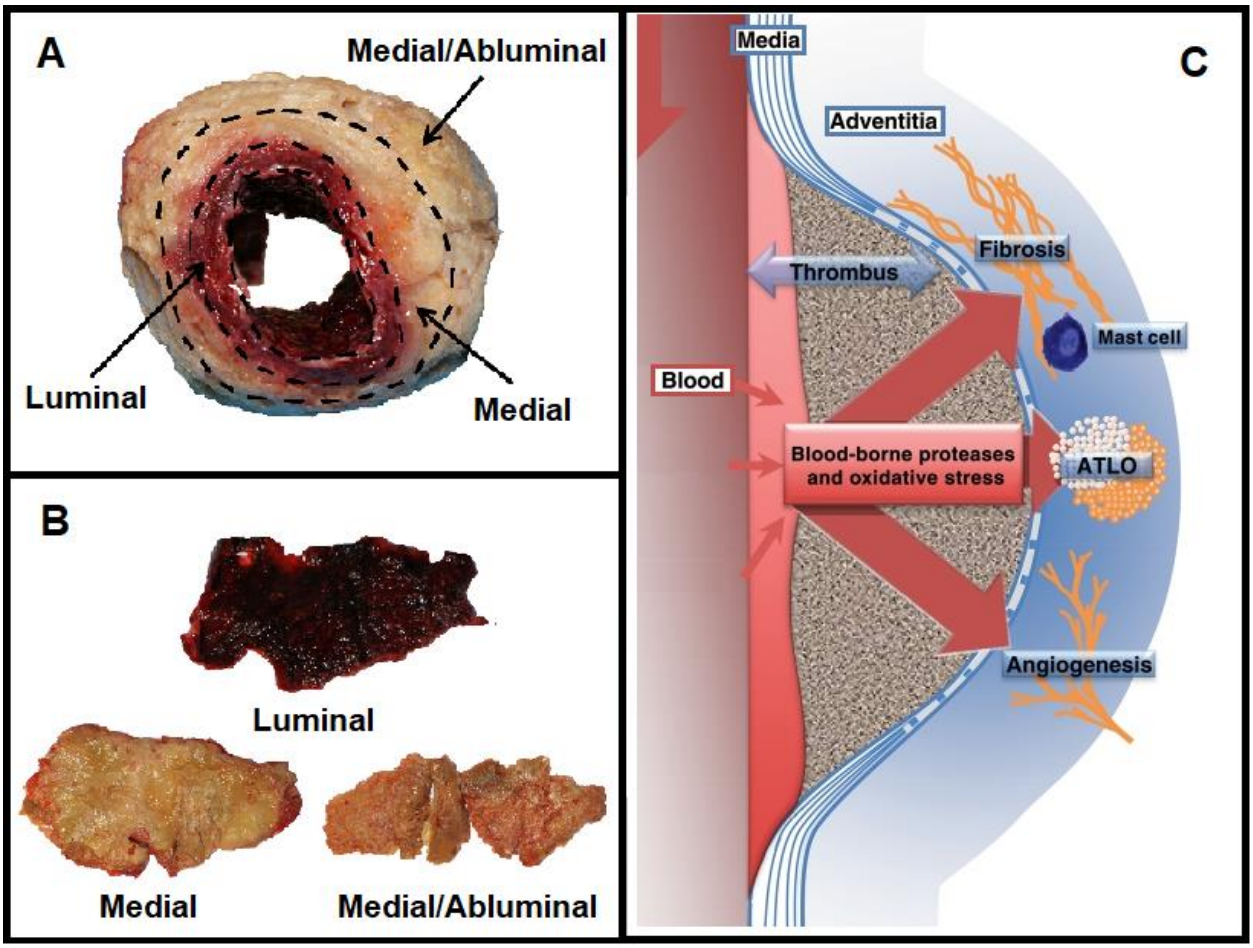

Figure 2.4: A) Three layers of ILT. B) Contents in each layer. C) A schematic illustration of the impact of a large ILT with subsequent biological response. (ATLO: adventitial tertiary lymphoid organ).
(Image source: Jean-Baptiste Michel et al., 2011 [102])

haemoglobin-rich content closest to the circulating blood, as a result of freshly clotted interface followed by platelet and thrombin activation. In the contrary, the medial and abluminal layers appear gradually less rich in blood-born contents but more fibrinolysed, spatially illustrating the clotting-and-lysis temporal events (103). A continuous fibrin network of interconnected canaliculi can be found throughout the ILT (104), allowing macromolecular penetrations from the luminal to the abluminal side of ILT. While fibrin deposition is observed in the entire ILT, fibrin degradation occurs mostly at the abluminal side (104), elevating the risk of aortic wall degeneration and aneurysm growth. Proteomic analysis of ILT has reported the prevalence of platelet-derived proteins which favor the proteolytic process. In line, suppressed ILT and AAA developments have been confirmed in animal studies with inhibitors for platelet activation to reduce vascular inflammation (105). On the other hand, the abundant leukocytes trapped within

ILT create an oxidative and proteolytic environment that promotes aortic wall destabilization. As such, clinical studies have revealed positive correlations between the ILT thickness and AAA diameter, MMP levels, elastin degradation as well as smooth muscle cell apoptosis (18). Despite the permeability of ILT, a large thrombus may cause localized hypoxia on the underlying vessel, accelerating media degradation, adventitial angiogenesis, subsequent inflammation infiltration and fibrotic responses at the outer layer (106), as shown in the schematic representation in Figure 2.4.

2.1.4.3 Calcification

Considerable wall Ca can be seen in about 80% of AAAs and frequently found in the common iliac arteries (26). Ca in AAAs are mostly heterogeneously distributed and located in the medial layer near the luminal surface, occasionally within or lateral to the ILT (near the adventitia).

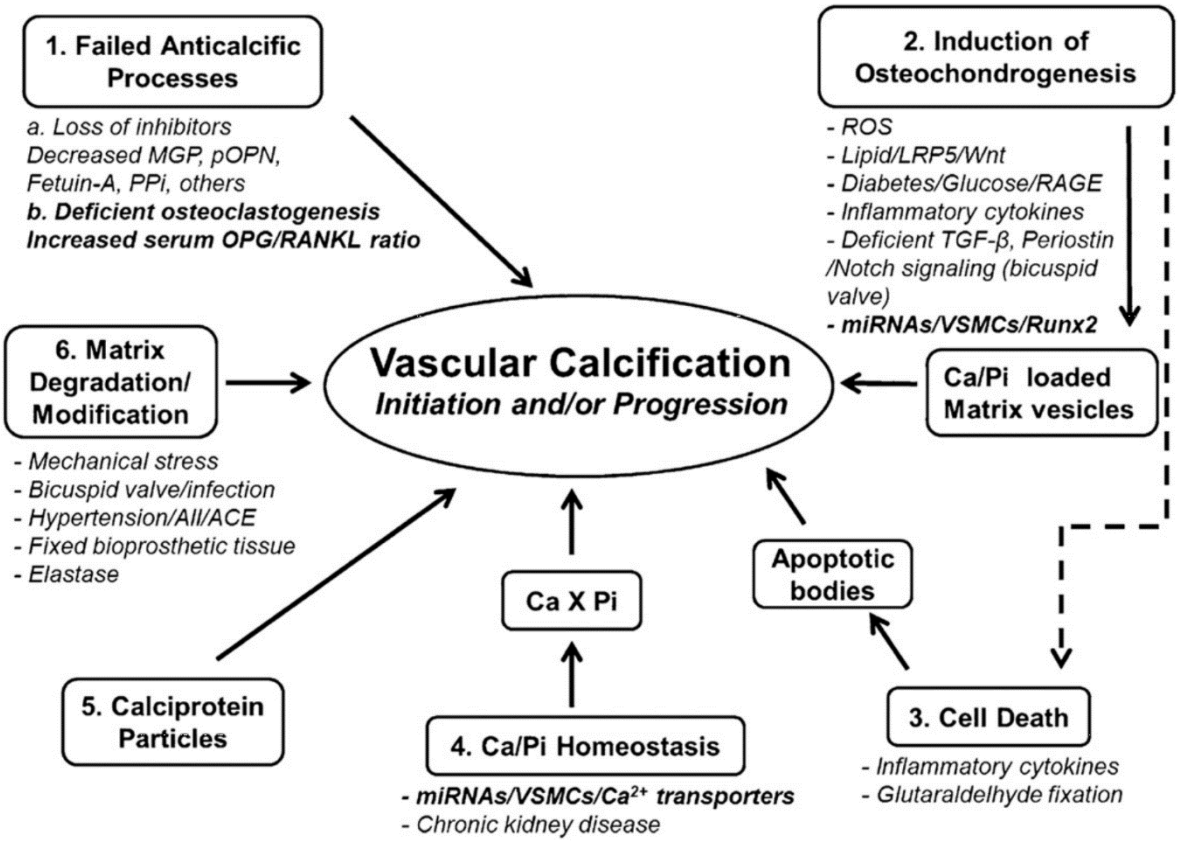

Figure 2.5: Major biological mechanisms and mediators of abdominal aortic calcification. (Ca: calcium; Pi: inorganic phosphate; PPi: pyrophosphate; MGP: matric GLA protein; OPN: osteopontin; ROS: reactive oxygen species; LRP5: low-density lipoprotein receptor-related protein 5; RAGE: receptor for advanced glycation endproducts)
(Image source: Pawel Szulc, 2015 [111])

Clinical risk factors of Ca in AAAs are indeed quite similar to those of AAA, including but not limited to: male sex, heavy smoking, inactive lifestyle, high-fat diet, obesity, dyslipidemia, type II diabetes, hypertension, ischemic heart disease history, hypogonadism, impaired glucose tolerance, treatment with vitamin K antagonists, vitamin D deficit and increased serum phosphorus levels (107–109). In addition, some genetic factors associated with abnormal lipid metabolism pathologies such as familial hypercholesterolemia or Singleton-Merten syndrome (110,111) can also contribute to the Ca development in AAA.

The development of aortic Ca is believed to be an active cell-regulated process involving a series of interconnected mechanisms at different stages of the biological pathway, as shown in Figure 2.5. This process is mainly initiated from the tunica media where vascular smooth muscle cells (VSMC) transdifferentiate into osteoblast-like cells (63,95–99,101), together with the uptake

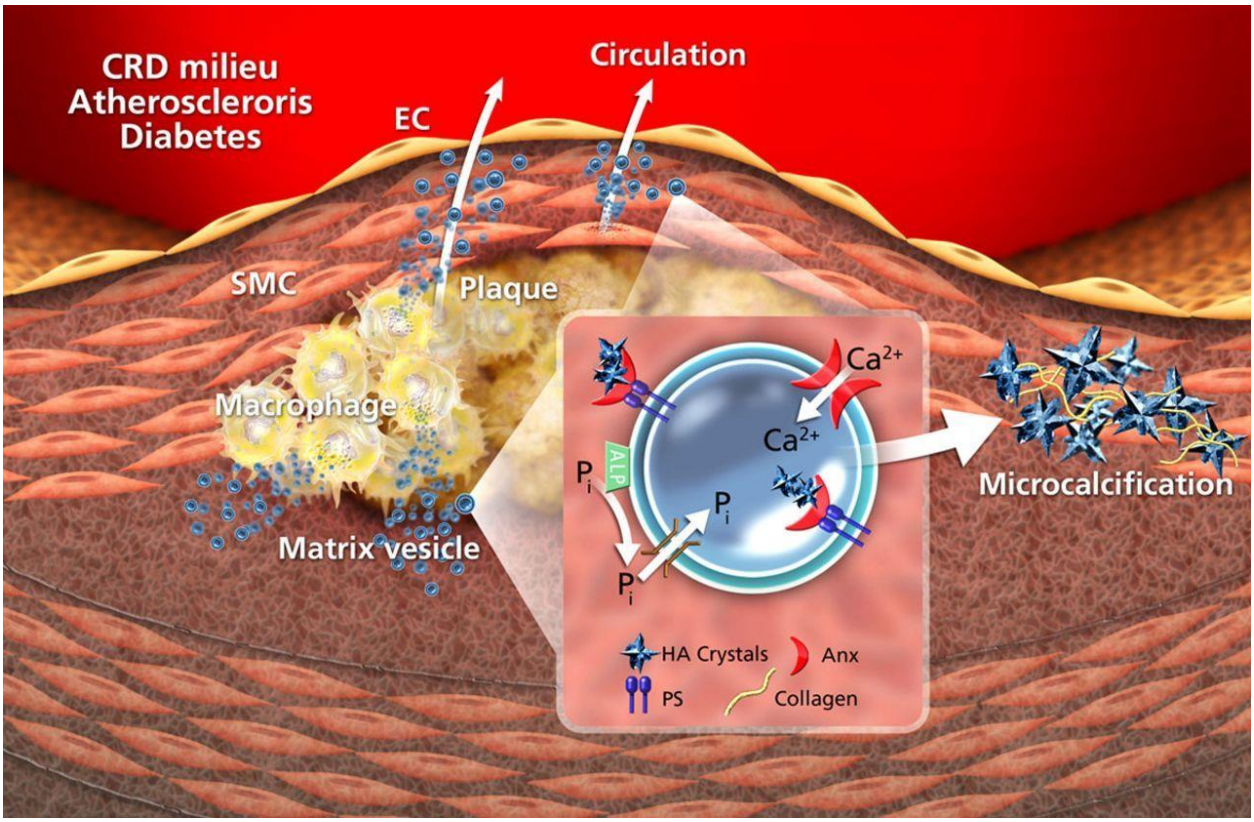

Figure 2.6: Mechanism of pathological MV mineralization, as a result of calcium and phosphate influx due to mineral imbalance. (Ca: calcium; Pi: inorganic phosphate; HA: hydroxyapatite; Anx: annexin; PS: phosphatidylserine; EC: endothelial cell; SMC: smooth muscle cell; CRD: chronic renal disease)

(Image source: Sophie E. P. New and Elena Aikawa, 2013 [112])

of other circulating osteoprogenitors, forming matrix vesicles (MV) in which the apoptotic vascular cells can become the nuclei for Ca. On the other hand, the disruption of elastin fibrils and lamella due to matrix degradation, as well as the abnormal homeostasis of calcium and inorganic phosphate, continuously promote the development of aortic Ca (112).

Pathological studies have shown that mineralization of MV can also be initiated by a mineral imbalance of calcium and phosphate ions in the extracellular space, which induces an influx of those ions into the vesicles and forms amorphous calcium phosphate. Nucleation of hydroxyapatite in the MVs can then be facilitated by an annexin-phosphatidylserine complex released by macrophages, eventually enabling Ca, as illustrated in Figure 2.6 (113).

As a major event in aortic Ca, osteogenic transdifferentiation of VSMC may be stimulated by multiple factors, such as: upregulation of the osteoblast-specific transcription factor, calcified fragments of elastin, hydroxyapatite, inorganic phosphate, oxidative stress, inflammatory cytokines, high glucose, high-fat diet, high oxidized lipids, bone morphogenetic proteins and certain pharmacological agents (114–119). Such transdifferentiation is also associated with the loss of expression of proteins that are specific for vascular muscle contract, reducing the contractility of VSMC (115) and enhancing the wall stiffening effect.

Besides VSMC, some other circulating cells can also differentiate under direct or in-direct stimuli into osteoprogenitors, such as: endothelial progenitor cells, adventitial myofibroblasts, myeloid cells, perivascular pericytes, bone marrow-derived mesenchymal stem cells and so on (120–124). Circulating osteoprogenitors are rather attracted to diseased lesions such as microcalcification related endothelial dysfunction, hypoxia, inflammation, injury and so on, than randomly enter the vascular wall. Although studies have revealed the effect on circulating osteoprogenitors in aortic Ca development (121,122,125–128), the transformability of circulating cells depends on the availability of relevant stimuli, their mobilization from niche, as well as their differentiation rate, resulting in a relatively heterogeneous Ca development (129).

All those biological mechanisms may trigger by several factors and cascade into a series of consequences which may then induce a positive feedback in Ca development. For example, higher calcium concentrations can trigger mineral deposit which favors VSMC apoptosis and elastic

lamina degradation, thereby promoting aortic Ca. As a result, the exact mechanism initiating the aortic Ca is non-trivial and yet difficult to identify.

2.1.4.4 Surrounding tissues

The vertebral spine and perivascular adipose tissue (PVAT) are the two major surrounding tissues of AAA. Although abdominal obesity is a risk factor for AAA, where the quantity of PVAT has been illustrated to be positively correlated with AAA diameter (130), the pathologic mechanism and effects of PVAT have received far less attention.

According to different anatomical locations, PVAT may exhibit divergent phenotypes with distinct physiological functions (131), as illustrated in Figure 2.7. For example, mesenteric and

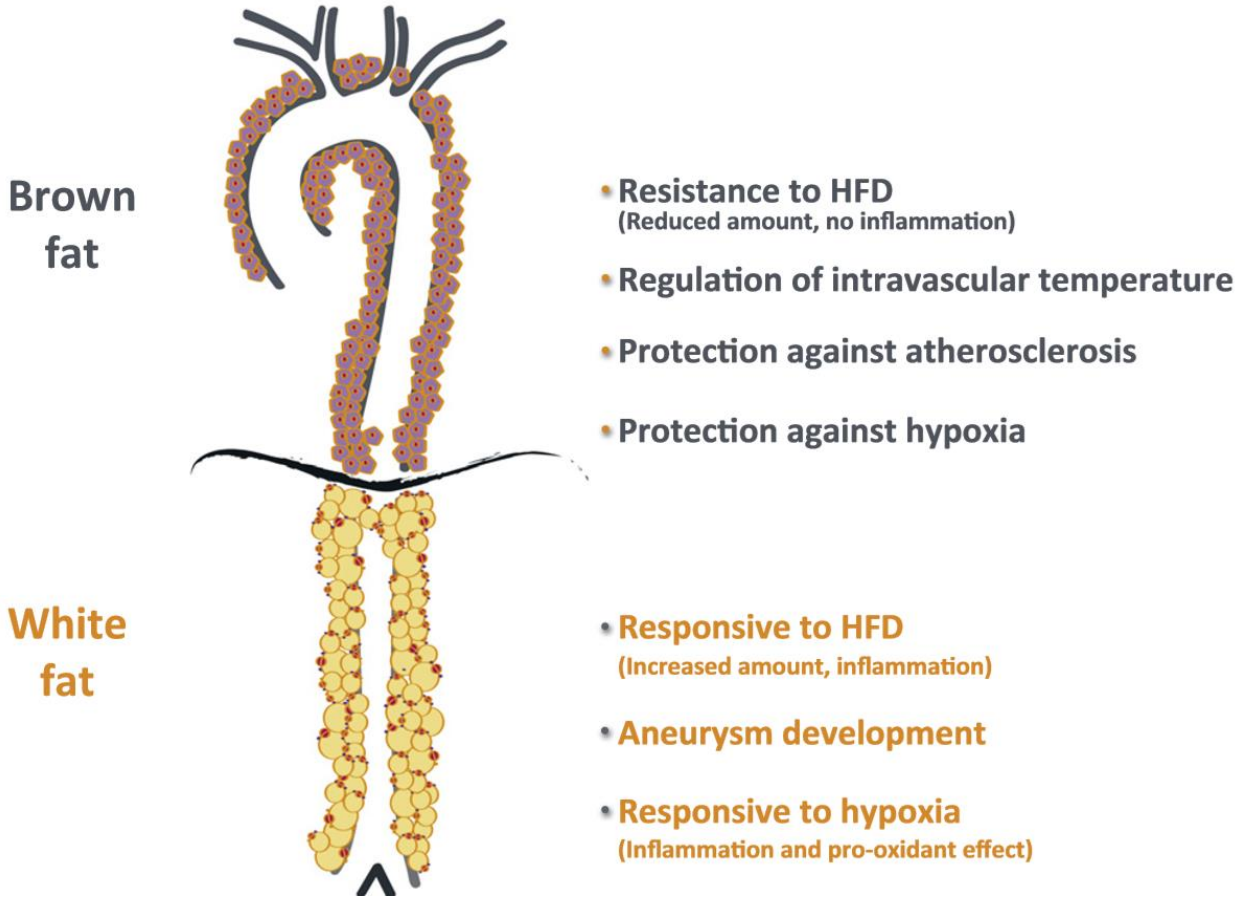

Figure 2.7: Schematic illustration of different PVAT located along the aorta, with distinct physiological effects indicated on the right. (HFD: high fat diet).

(Image source: Marta Gil-Ortega et al., 2015 [130])

femoral PVAT display a white adipose tissue (WAT) phenotype, whereas thoracic PVAT shows the characteristics of a brown adipose tissue (BAT) phenotype. Studies have shown that WAT is highly associated with high fat diet (HFD) and macrophage infiltration into the vascular wall, causing hypoxia with elevated oxidative stress which favors aneurysm growth; in the contrary, BAT appears resistant to HFD and thus exhibiting the opposite effects (131).

Of note, there is no clear division in pure WAT or BAT along the aorta, an intermediate phenotype between WAT and BAT is found in abdominal PVAT (132). In general, abdominal PVAT is more prone to inflammation than thoracic PVAT, indicated by the higher amount of immunomarkers and inflammatory gene expressions (133). Furthermore, increasing evidences suggest that phenotypic changes in abdominal PVAT as a result of smoking or HFD can promote vascular inflammation and wall remodeling, as well as matrix degradation to facilitate AAA development (134).

PVAT can modulate VSMC activities such as contraction, proliferation and migration (135). On the other hand, Folkesson et al. compared the immunohistochemistry and gene expression of PVAT (with AAA wall) collected from 19 patients to 9 healthy abdominal aortic tissues. Results indicated the increase of neutrophils, macrophages, mast cells, T-cells, cathepsin K and S surrounding the necrotic adipocytes in PVAT, implying those adipocytes as a source of inflammation and protease that favor ongoing damage on the adjacent aneurysmal wall (136). With an animal study, Poice et al. demonstrated that obesity could increase macrophage infiltration and cytokine expression in PVAT surrounding the abdominal aorta, which promoted angiotensin-induced AAA formation (137). Interestingly, vasa vasorum is absent in human abdominal aorta (83), recruitment of immune cells or inflammation is in fact enable through the neovascularization at the adventitia layer (138) protected by the WAT and BAT, resulting in a highly vascularized PVAT (139). Although inflamed PVAT is associated with arterial stiffness and vasculitis, the exact pathologic role of PVAT remains to be elucidated due to the challenges in developing relevant experimental models.

2.2 Treatments of AAA

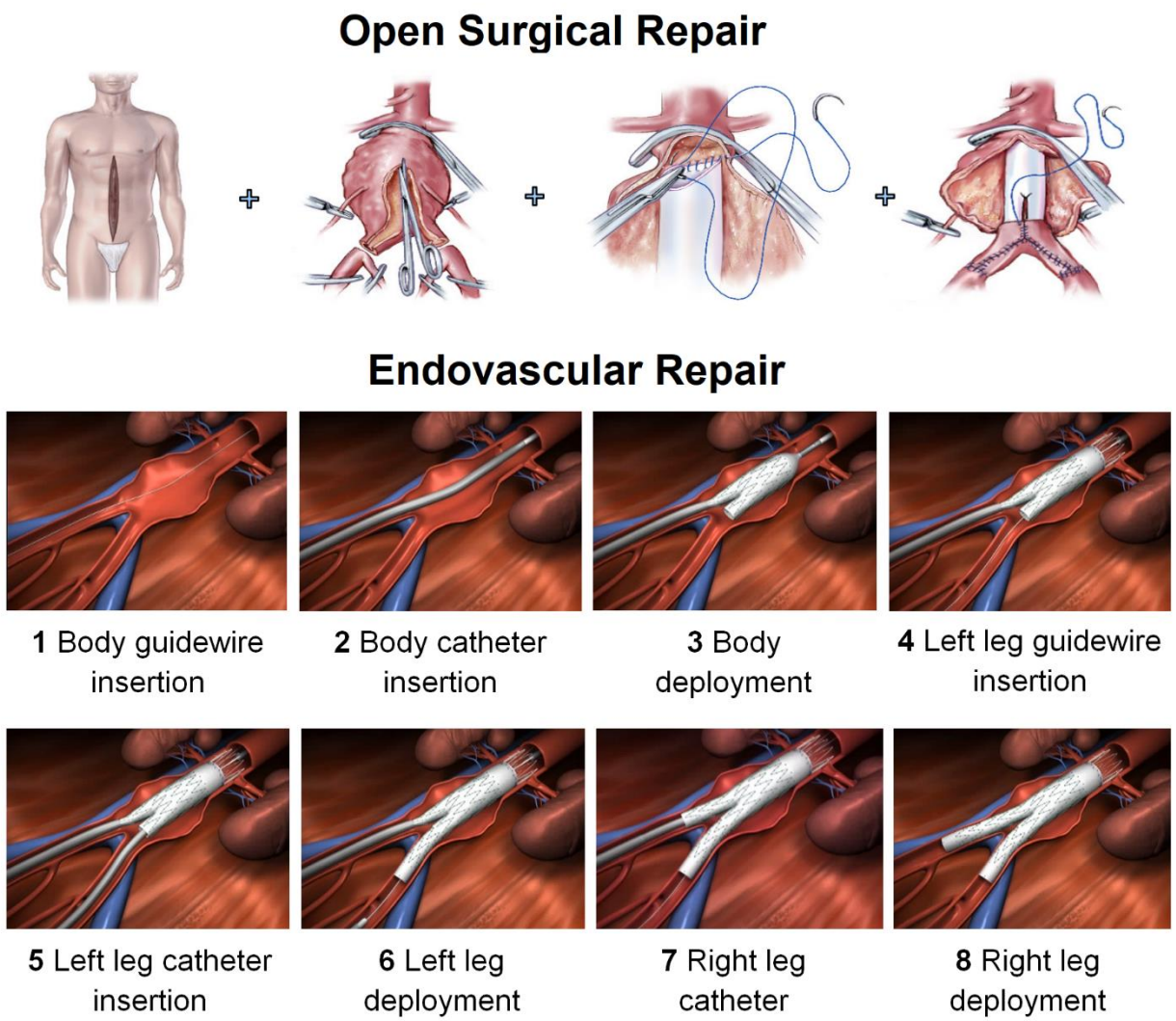

Figure 2.8: Schematic illustration of main procedures in open surgery and EVAR.
(Image source: David Roy, 2015 [239])

AAAs with diameters less than 5 cm will not be treated. To date, surgical repair is the most effective treatment for AAAs greater than 5 cm. Two repair options, as shown in Figure 2.8, are normally considered.

- *Open Surgical Repair (OSR):* it is a traditional and aggressive approach where the AAA is surgically exposed so that the aneurysmal section can be repaired by prosthetic grafts.

- *Endovascular Repair (EVAR):* it is a minimally invasive approach where a catheter is introduced, from the iliac artery at the groin to the AAA, and deploys stents grafts (SG) to exclude the aneurysmal sac.

Both treatments present immediate as well as long-term risks to the patient and should be reserved to the cases where the risk of AAA rupture outweighs surgical risks (140).

2.2.1 EVAR *vs* open surgery

Numerous clinical trials worldwide have continuously investigated the outcomes between EVAR and OSR in AAAs. The concept of EVAR was introduced more than two decades ago, and often recommended because of its lower morbidity and mortality compared with OSR (1.6% versus 5%) (141–143), especially within the first two years. Consistent data has confirmed that EVAR not only minimizes the time, blood loss, transfusion requirements, morbidity and mortality during operation, but also reduces the length of hospital stay and the need for intensive care (8,33–35,37,141). However, this early survival benefit is lost after four years owing to higher rates of graft-related complications (particularly endoleaks with residual flow around SG) (143), secondary interventions and the excess late deaths due to aneurysm complications (8,33–35,37,141). As such, no significant mid and long-term advantage was reported for EVAR in terms of survival rate, quality of life and costs (29,30,32,86). Hence, EVAR is considered a safer option for patients in older age or with higher risk factors, whereas OSR is expected to be a more durable option for young and relatively fit patients, which is in fact a less common scenario (38–41).

2.2.2 Evolution of EVAR

Over the past two decades, the EVAR technology has evolved substantially to enhance procedural success and long-term durability, expanding the EVAR patient population (144). Patients with more challenging anatomies (short and angulated AAA neck) are treated outside the device manufacturers' *Instructions for Use*, leading to an increase of adverse events and mortality rate (145). Nowadays, more complex EVAR procedures are performed to extend the SG sealing zone to the origins of renal and digestive arteries, for example the branched devices, fenestration and chimney techniques, preserving the patency of vessels (146). However, many challenges remain, such as the proper SG selection, the catheter navigation in tortuous arteries, the

geometrical fit between SG and aortic wall, and the alignment with multiple side branches using branched grafts, fenestration or chimney techniques. Of note, with the rapid evolution of SG designs (third generation SG, endovascular sealing system (147)) and EVAR approaches (fenestration, chimney, endoanchor techniques (148)), better understanding the biomechanical interaction between SG and AAA is becoming crucial.

2.2.3 EVAR complications

The quality of EVAR strongly depends on the evaluation of the patient's vascular anatomy, the appropriate implant selection, as well as the optimal procedure planning. In general, complications in EVAR treated AAA can be device-related and/or systemic. Device-related complications include endoleaks, SG migrations, limb kinking or occlusion, iliac thrombosis and SG collapse; whereas systemic complications often related to ischemia in limbs, kidneys, bowels, spinal cord and pelvis.

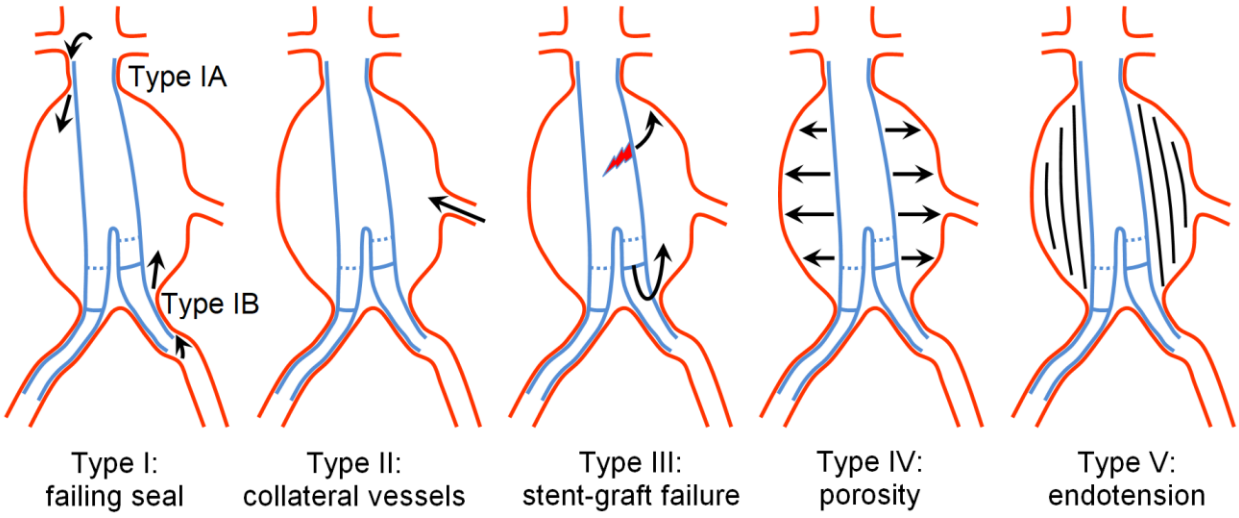

Figure 2.9: Different types of endoleaks in AAA (red line: AAA and iliac arteries; blue line: SG; black arrows: blood flow leaking into aneurysm sac).

(Image source, David Roy, 2015 [239])

In particular, endoleaks are the most common complications in AAA, with a prevalence of 15-30% within the first month after EVAR (149). There are five types of endoleaks, where SGs fail to completely exclude the aneurysm sac due to persistent blood flow perfused from different locations, as illustrated in Figure 2.9. Type I endoleaks correspond to the failure of the circumferential seal at either the proximal (IA) or distal (IB) sides of the SG, causing higher tension

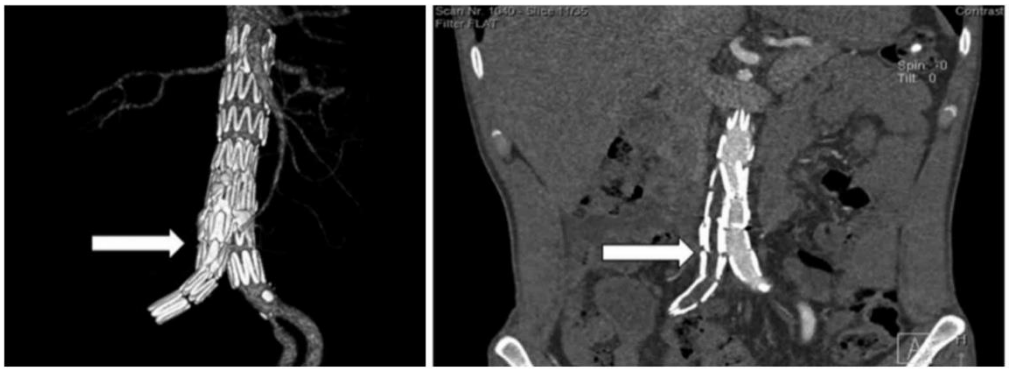

Figure 2.10：3D reconstruction (left) of AAA and SG and a relevant CT scan (right) for the AAA patient at one year after EVAR. Arrows indicate the iliac artery occlusion on the right side, with dark region indicating the discontinued blood flow due to thrombosis).
(Image source: Guoquan Wang et al., 2017 [152])

on the wall by direct blood perfusion into the aneurysm sac, increasing the risk of vascular rupture. Type II occurs when there is continuous blood flowing in and out of the aneurysm sac from aortic side branches (inferior mesenteric artery, lumbar arteries, accessory renal arteries or the left subclavian artery). Type III and IV are both related to the failure of SG itself: Type III is caused by SG structural failure such as tears in SG fabric or disconnections between SG components, whereas Type IV is normally due to the porosity in SG fabric. Type V is also referred as endotension, where the aneurysm sac continues to expand without any evidence of leaking as mentioned above. To date, Type I and II remain the most common complications in AAA after EVAR (149). Besides endoleaks, limb thrombosis is another major complication after EVAR (Fig. 2.10), with an incident rate reported from 2% (early) (150) to 25% (long-term) (151). Apart from vessel kinking and large iliac artery angulation (iliac tortuosity), pronounced Ca has also been demonstrated to be a predisposing factor (152,153). As such, anti-coagulation medical treatments are often recommended after EVAR to prevent limb thrombosis, especially for patients with existing peripheral artery disease (154).

Chronologically, the first major failure of the EVAR approach occurs during the delivery stage, where the access of catheter is limited by the hostile anatomies at the distal end of AAA and the common iliac arteries, increasing the risk of vessel injuries during delivery (dissection, pseudo-aneurysm, vessel perforation, and vascular avulsion) (8) and subsequent limb thrombosis. Not only the vessel diameter and tortuosity, but also the degree of calcification and thrombus are critical to

both successful device navigation and adequate distal sealing (42). EVAR is recently advanced to an even less invasive level by replacing the traditional access method (surgically cut down of common iliac artery) to a percutaneous access technique. Several clinical reports have underlined the degree of Ca as a determinant for the success with percutaneous technique, as percutaneous access and the use of closure device can be impaired by Ca at the anterior vessel wall (43–45).

The second major failure of the EVAR approach occurs during the deployment stage, where the SG cannot be landed and adhered properly on the attachment site of the AAA. Ca, ILT, vessel angulation at attachment sites, and tortuosity of the access vessels are generally considered important risk factors to be evaluated before EVAR (46). Anatomical fit between the SG and AAA is an essential criteria for successful EVAR treatment (42). A tight seal between the SG and attachment zone is required to avoid complications such as endoleaks, endotension and SG migration, minimizing the risk of thrombotic embolism (47). Ca at the proximal neck is believed to impair fixation between the SG and the vessel wall, as it may create heterogeneity in wall structure and impede the attachment of SG. Severe Ca around the neck of AAA has already been associated with a higher rate of endoleaks by Wain et al since 1998 (48). On the other hand, thrombus with its softer nature may provide a more snug adhesion between the vessel wall and SG. In 2011, Wyss et al. observed over 217 patients and concluded that higher rates of complications were associated with increased Ca and angulation at the proximal neck, as well as greater tortuosity and thrombus along the common iliac arteries; surprisingly, the iliac Ca and neck thrombus appear to have a protective effect against complications (49). Unfavorable neck anatomies such as significant Ca and angulation at those regions are thought to have important contributions for developing Type I endoleaks (50). In 2004, Sampaio et al. revealed the correlation between the amount of circumferential Ca around AAA neck and the risk of developing proximal Type I endoleaks, especially in the case of large aneurysm with short and heavily calcified AAA neck (52). In 2013, Antoniou, G. A. et al. reported a four-fold increased risk of inducing Type I endoleaks and a nine-fold increased risk of aneurysm-related mortality within one year of treatment for patients with unfavorable neck anatomy (51).

The third major failure of the EVAR occurs after the operation, either in short or long-term, including kinking or thrombosis of SG due to the degree of bending in tortuous vessels, the failure of AAA sac shrinkage in the absence of endoleaks, migration of SG and so on, which may all lead

to vascular rupture. Some of those complications may also induce a high risk of SG rupture (53). Ca in the aneurysm wall has long been speculated as a contributing factor for the failure of vascular shrinkage, especially in the case of complete circular calcification in the outer wall of AAA (54,55). In 2005, a clinical study by Love et al. demonstrated a positive correlation between the degree of Ca in AAA and the failure to shrink, implying a significant role of Ca in predicting aneurysm diameter reduction after EVAR (56). Taken into account the fact that endotension, having pressure sustained within the aneurysm sac without endoleaks, has been considered responsible for the failure of aneurysm shrinkage, the authors further suggest that Ca in the aneurysm sac may indeed promote endotension (56). In 2009, Pitton, M. B. et al. reported that the occurrence of large endoleaks, which may significantly impair aneurysm shrinkage, was reduced by pre-existing occlusion of the aortic side branches, supporting the hypothesis of correlations between Ca and endotension, as well as Type II endoleaks (57). On the other hand, as another serious complication after EVAR, migration of SG is often evaluated by the coefficient of friction (COF) and the contact pressure between the SG and vessel wall. In 2010, Vad, S. et al. developed a finite-element model along with experimental measurements to evaluate the COF of various SGs, and indicated the COF decreased with oversizing SGs (155).

2.3 AAA biomechanics

2.3.1 AAA wall

Explorations on the relationship between aortic wall stress and AAA development, as well as the risk of rupture, have been further extended using numerical modeling method. Numbers of sophisticated finite-element models have been developed to investigate the biomechanical effects of aortic wall. Although having the micro-structure and composition similar to other human arteries, AAA wall has been proven to have stiffer mechanical property due to the aneurysm formation (156). Studies have indicated that AAA wall is incompressible and hyperelastic, exhibiting non-linear but reversible stress-strain behavior, which enables it to withstand large deformation before rupture (94). Uniaxial tensile tests have revealed not only its anisotropic mechanical properties (stiffer in the circumferential than the longitudinal direction, shown in Fig. 2.11), but also variations of those properties at different locations of the AAA (anterior, posterior and lateral regions) (156,157). The notion of anisotropy has been further confirmed by Vande

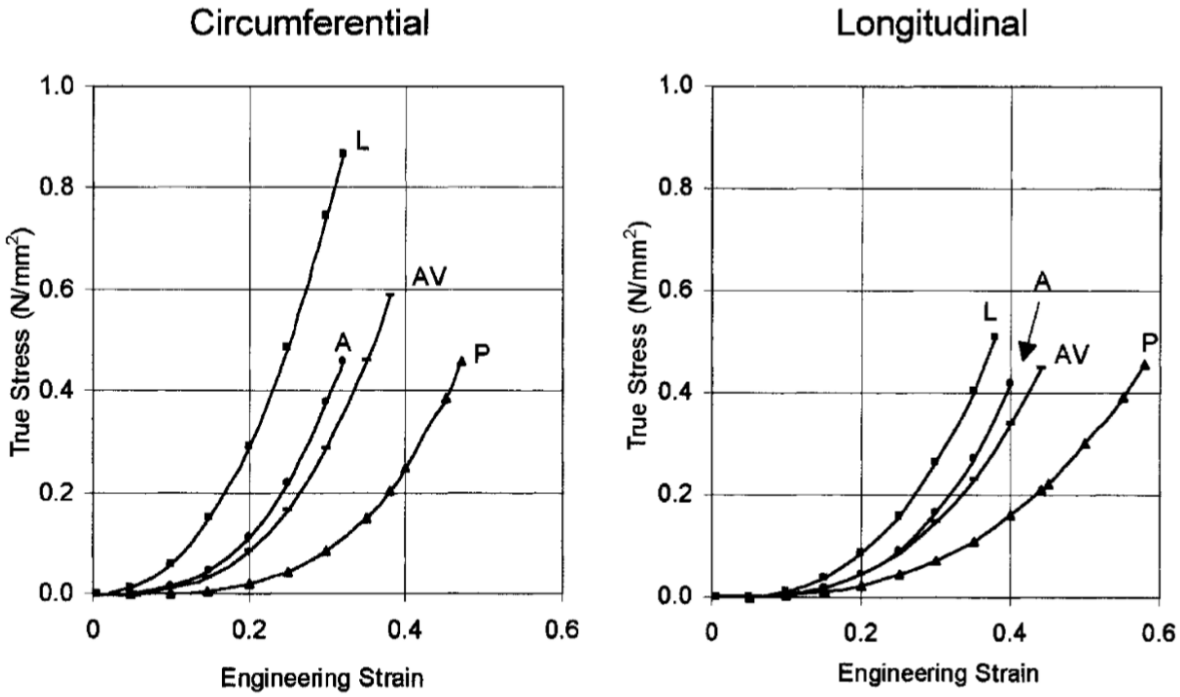

Figure 2.11: Stress-strain curves averaged from multiple samples of the same freshly harvested human AAA. Uniaxial tensile measurements done along different directions and at different locations of the AAA (L: lateral AAA; A: anterior AAA; P: posterior AAA; AV: averaged over all locations).
(Image source: Mano J. Thubrikar et al., 2001 [156])

Geest et al. using biaxial tensile tests, and suggested to only consider healthy aortic tissue isotropic (158). Moreover, the significant loss of VSMCs and elastins compromises the vascular elasticity in the AAA wall, justifying the assumption that viscoelasticity can be neglected in modelling the wall (61,93,94).

The research groups of Raghavan, Vorp and Fillinger (159–162), as pioneers in biomechanical research on the aortic wall stress, have suggested that an increase in wall stress may accompany with the decrease in the ability of the aortic wall to withstand this stress; as the wall stress continues to increase along with aneurysmal growth, the material strength of the wall gradually diminishes, and the AAA will rupture when the wall stress exceeds its failure strength. This hypothesis is further supported by experimental measurements indicating the almost 50% reduction in failure strength of the aneurysmal aortic wall (159). Computational results reveal that the peak wall stress significantly increases as the AAA grows, and the volume rather than the diameter of AAA provides better indications for the peak wall stress (160,161). Moreover, peak

wall stresses are found considerably higher in ruptured or symptomatic AAAs than diameter-matched and asymptomatic AAAs (162).

Wall stress analysis of 3D models combining finite-element method and fluid-structure interaction appear practical, feasible and reliable. It may provide more fundamental evidence to predict AAA interactions with endovascular devices, as well as to evaluate the rupture risk, together with traditional clinical indices.

2.3.2 Intraluminal Thrombus

Around the abdominal aortic bifurcation, pulse waves creates an amplified echo accelerating vascular dilation (63). Subsequently, blood flow stagnation and recirculation, wall shear stress and platelet aggregation at this region may promote ILT formation. It is believed that ILT has significant biomechanical effect on the behavior of AAA, and is often modelled as homogeneous and linear elastic material with Young's modulus of 0.11MPa and Poisson's ration of 0.45 (66).

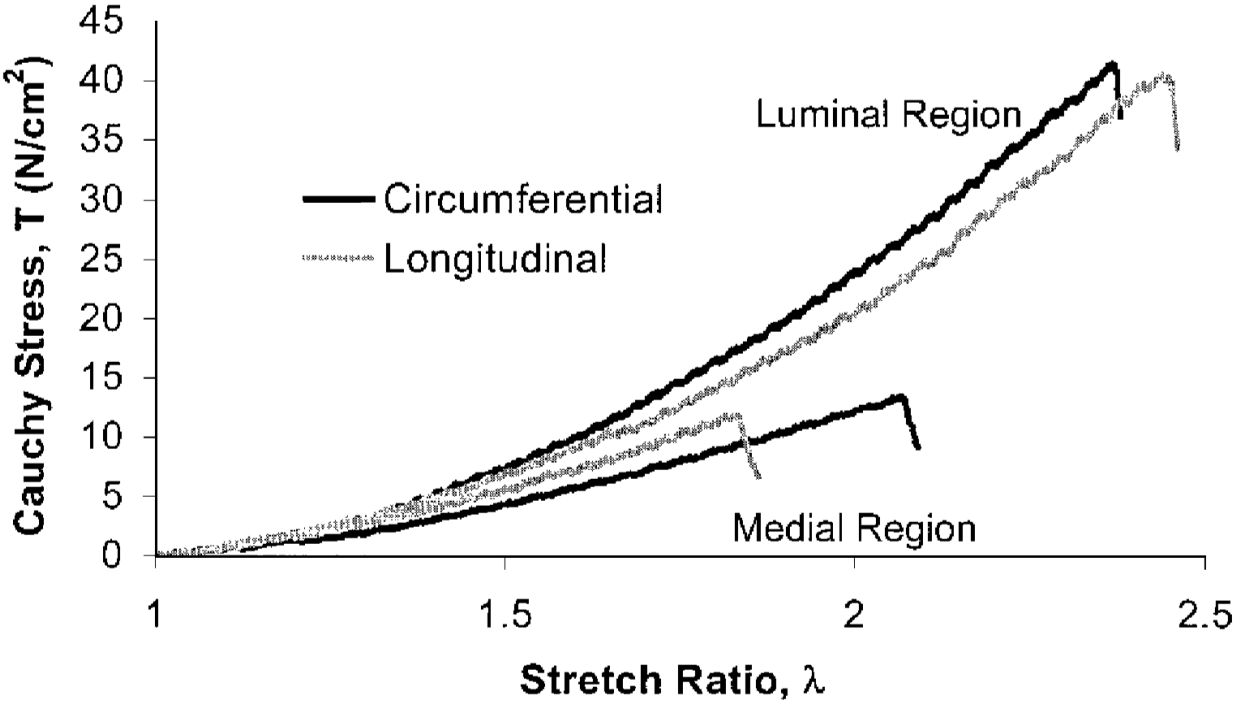

Figure 2.12: Uniaxial tensile measurements along different directions at different layers of ILT from the same patient, illustrating its inhomogeneity in mechanical properties.

(Image source: David H. J. Wang et al., 2001 [65])

Indeed, an in-depth study of the fresh ILT by Wang et al. have revealed that the ILT is an inhomogeneous, non-linear elastic and isotropic material, which consists of three layers of fibrotic contents with different mechanical properties (65) (Fig. 2.12). Specifically, the luminal side is the stiffest with maximum ultimate strength up to 540 kPa under uniaxial loading, whereas the medial layer exhibits much lower ultimate strength (max. 300 kPa) due to the absence of cellular constituent and progressive fibrinolysis. Not surprisingly, the abluminal layer was too degraded for measurements.

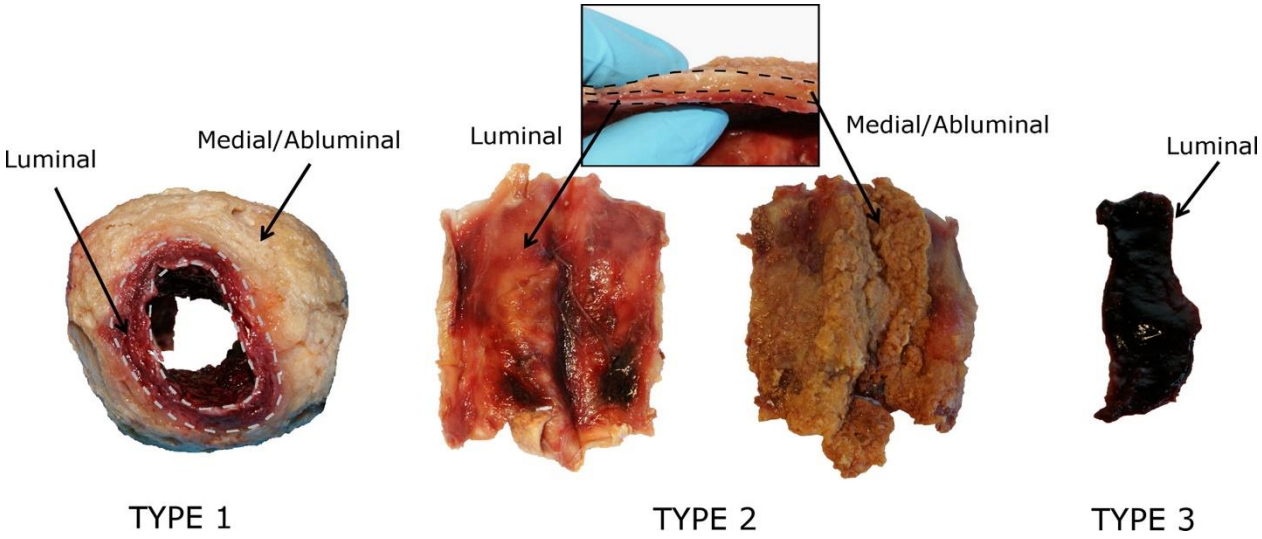

Figure 2.13: Three subtypes of ILT, based on the composition of luminal, medial and abluminal layers. (Image source: Siobhan A.O'Leary et al., 2014 [162])

More recently, O'Leary et al. have conducted bi-axial mechanical tests and further classified the diverse ILT structures into three subtypes (163) (Fig. 2.13). Type 1 is the most popular case, with distinct multi-layered morphology in which the stiffness and strength gradually decrease from the luminal towards the abluminal layer. Type 2 also has a distinct luminal layer, but the medial-abluminal layer is rather thin or highly degraded, resulting in an abrupt loss of mechanical resistance in this layer. Type 3 is a rare case, with a fluid-like single layer having the lowest mechanical stiffness and strength.

Despite the numbers of experimental and numerical studies, the role of ILT on the mechanical behavior of AAA remains a debatable topic. Some believe that the ILT provides a protective effect as it may act as a pressure "shield" to alter stress distributions and reduce the peak wall stress (67,68,164). However, others argue that the porous nature of the ILT allows blood flow and

pressure to be transmitted onto the wall (69,94), and that ILT is in fact vulnerable against fatigue failure (165), reducing the "cushion" effect substantially. Of note, keeping in mind the prevalence of inflammatory and proteolytic responses in ILT, which not only weakens the underlying aortic wall but also promotes aneurysm growth, this protective role may be loss depending on the degree of ILT (166).

2.3.3 Calcification

Given the complex nature and heterogeneous development of aortic Ca, to identify its exact biomechanical role has been challenging. Although numbers of attempts via experimental evaluations, clinical observations and numerical analysis have been conducted worldwide to address this complicated issue, our understanding remains at the beginning of its learning curve.

2.3.3.1 Quantification

Various methods for vascular Ca quantification have been considered, in which Agatston score remains a popular choice. This method was proposed in 1990 and originally used to study Ca in coronary arteries(167). Specifically, Ca was detected from CT image where the intensity exceeds 130 HU for an area greater than 1 mm^2 (to prevent false positives due to noise) and meanwhile, Ca area was measured automatically. Subsequently, a density score based on the maximum value of each Ca region could be defined: score 1 for 130 – 199 HU, score 2 for 200 – 299 HU, score 3 for 300 – 399 HU and score 4 for 400 HU and greater. The Ca score of each slice was then computed by multiplying the density score and the corresponding area. Finally, the total Ca score could be defined by adding up those Ca scores for all slices along the volume of interest. Agatston score has been considered the most efficient and reliable method for Ca quantification and thus, being continuously adopted and/or modified (i.e., Callister method) in many clinical and experimental studies to investigate cardiovascular diseases (168–171). However, this method is not suitable for X-ray analysis with contrast agent, for example digital angiography.

Of note, the Agatston score was invented to quantify coronary Ca, whereas the technical difference in CT acquisition for AAA, as well as the presence of intraluminal contrast, may affect the accuracy and even the reliability of this method. As such, Buijs et al. have further investigated the variations in Ca measurements due to: 1) differences between abdominal and coronary CT

scanning protocols, using the same Ca phantom; 2) differences between contrast and non-contrast CT scans, using the same intensity thresholds (172). Consequently, different CT acquisition techniques did not result in any significant difference in Ca quantification; however, both measured Ca volume and mass were overestimated compared to the actual sizes. Patient-specific thresholds to clearly distinguish aortic Ca from the contrast in lumen were found to be 230 ± 22.6 HU, much higher than the threshold used for the Agatston score. This thresholds could vary greatly between 130 and 1000 HU, depending on the contrast material and screening protocol (173,174). Not surprisingly, with the same threshold value, the volume and mass of Ca measured in CT with contrast were significantly larger. The authors concluded that, current parameters for threshold-dependent quantification method would grossly overestimate the aortic Ca, especially for CT with contrast. Corrective measures or patient-specific thresholds were therefore recommended to improve the accuracy, validity and reliability of outcomes.

In order to have a more practical solution for clinical studies, an Abdominal Aortic Calcification-8 score (AAC-8) has been introduced (175,176), as a simplified version of the AAC-24 score proposed by Kauppila (177), which characterizes semi-quantitatively the severity of Ca based on visual inspection. Specifically, the AAA is divided into 8 sections: along the anterior and posterior walls corresponding to lumbar vertebrae L1 to L4. Each section is then scored as 0 if no Ca exists, 1 if the area of Ca appears less than one third of the corresponding wall, 2 if it's more than one third but less than two thirds, and 3 if it occupies more than two thirds, resulting in a total score of all eight sections ranging from 0 (no Ca) to 24 (severe Ca), as shown in Figure 2.14. Hence, it is also referred as the Framingham Heart Study Aortic Calcification Severity AAC-24 index scoring system in some studies (178,179). This method can be applied to CT images with contrast; however, it is highly observer dependent and not able to distinguish between micro- and macro-Ca (180).

Moreover, other methods to quantify aortic Ca include but not limited to: visual inspection of the sagittal and coronal views (181); grading the Ca proportions of cross-sectional quadrants (182), area (169) or circumference (21); and measuring the percentage of affected circumference and segment length, diving into mild (< 33%), moderate (33% to 50%), severe (> 50%) and complete (~100%) types (42,44,49,56,183).

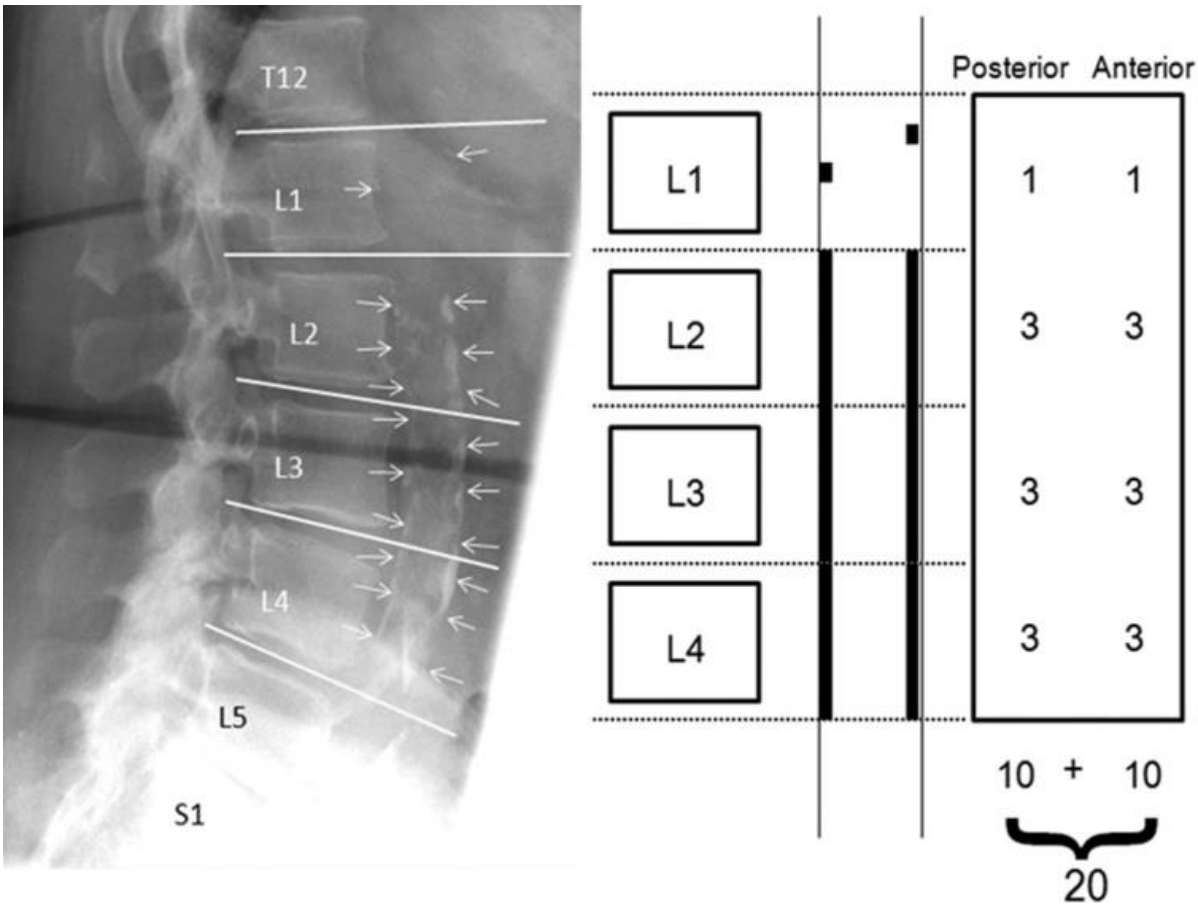

Figure 2.14: Framingham Heart Study Aortic Calcification Severity AAC-24 index scoring system. Left CT scan (sagittal plane) showing the anterior and posterior abdominal aortic walls beside different lumbar sections. (Image source: Friedlander A.H. et al., 2015 [177])

2.3.3.2 Clinical studies

In a cohort study by Lindholt et al. in 2008, 122 men with small AAAs of diameter from 30 to 49 mm were analyzed using ultrasonography (21). They were initially divided into groups of Ca being either more or less than 50% of the maximal AAA circumference, then followed by annual screening over the mean of 6.15 years. The authors reported the expansion rate of AAA with Ca more than 50% of AAA circumference being significantly slower than the other group. Nevertheless, no difference in relevant symptoms and mortality was observed, both in univariate analysis and after adjustment for age, smoking and the use of aspiring. Hence, they concluded that Ca might be protective against aneurysm expansion but not AAA associated risks.

In 2013, Buijs et al. have conducted a case-control study based on clinical evaluations of 334 AAA patients which were classified into electively treated (eAAA: AAA diameter beyond threshold or with fast AAA growth rate) and non-electively treated groups (rAAA: ruptured AAA, or sAAA: symptomatic non-ruptured AAA) (180). Ca levels were measured by AAC-8 score and relevant comorbidity records (serum creatinine, body mass index, hypertension, cardiovascular disease, etc.) were collected. The authors reported a significantly higher AAC-8 score in rAAA and sAAA patients compared to eAAA (4.9 vs 3.4), whereas peripheral artery disease was strongly correlated to eAAA patients (OR=0.39). Therefore, they suggested Ca to be an indicative factor for symptoms development (lower back pain, abdomen tenderness, pulsating abdominal mass being painful on palpation) and AAA rupture prediction.

A retrospective cohort study involving 414 Japanese AAA patients has been performed in 2015, where patients were divided into repaired and non-repaired groups(169). Each patient had undergone minimum two sequential CT scans that were at least 90-days apart. The extent of Ca was calculated by averaging the Ca indexes (Ca area over the corresponding cross-sectional vessel area) along the whole AAA, in which Ca area was detected with a density over 130 HU on the non-contrast CT image. Evidences have confirmed that AAA expansion was strongly inversely correlated with the aforementioned Ca index. The authors have found that an expansion exceeding 5 mm annually was significantly associated with a Ca index <2.74% with AAA diameter >45 mm at the initial diagnosis. More importantly, they underlined that the location of Ca might be in fact more crucial than only considering the overall Ca extent.

In 2018, Chowdhury et al. have investigated the association between aortic Ca and call-cause mortality, cardiovascular mortality and morbidity(171). Modified Agatston score was used to quantify Ca in 123 thoracic aneurysm (TAA) and 196 AAA patients during a median follow-up period of 30 months. The authors reported that aortic Ca for both TAA and AAA were significantly related to all-cause and cardiovascular mortality, whereas Ca in TAA was also highly associated with cardiovascular morbidity. Results underline the potential role of aortic Ca score, as a predictive tool to rapidly identify high risk patients and minimize treatment failure.

2.3.3.3 Numerical simulation & experimental analysis

From an engineering perspective, calcified deposits in the vessel wall act as geometric singularities that create heterogeneity in the wall structure, resulting stress concentration may significantly affect the mechanical behavior of the wall. Although numbers of clinical and numerical studies have been focused on this topic, results seem contradicting: some saying that calcification increases stress and becomes a risk factor for aneurysm rupture, whereas others saying that it stabilizes the aneurysm wall.

In agreement with the assumption that aortic calcifications can act as stress concentrators, Putter et al. (70) (2006) developed FEA models using patient-specific calcification geometries and idealized aortic wall to characterize the calcification-wall interface phenomena in AAAs, and underlined the sensitivity of peak wall stress to the calcification material properties. Speelman et al. (71) (2007) conducted the first computational analysis with patient-specific FEA models to evaluate the effect of calcification in AAAs. Their results show that calcifications can alter the stress distribution and increase the peak wall stress up to 22%, and also suggest that not only the extent but also the location and shape of calcifications are important factors affecting wall stress in AAAs; the importance of proper calcification material properties determination was also highlighted. To describe the relationship between the AAA wall stress and the volumes of calcifications and ILT, Li et al. (67) (2008) also developed patient-specific FEA models representing the non-calcified, no-ILT and calcification-plus-ILT cases. Their results shown an average of 14% decrease in the maximum stress while the calcification was absent; besides, a negative correlation was found between the volume of ILT and the maximum wall stress, with an average of 24% increase in the maximum stress while the ILT was absent. With patient-specific fluid-structure interaction models involving both ILT and calcifications in various regions, Michalis Xenos et al. (72) (2010) found a strong stress gradient propagating around the calcifications, particularly at the interface between the calcification and aortic wall, implying the role of calcification as a contributing factor for AAA rupture. They also claimed that small calcifications may weaken the wall and increase rupture risk, whereas large plaque-like calcifications may reduce the stress of the adjacent wall.

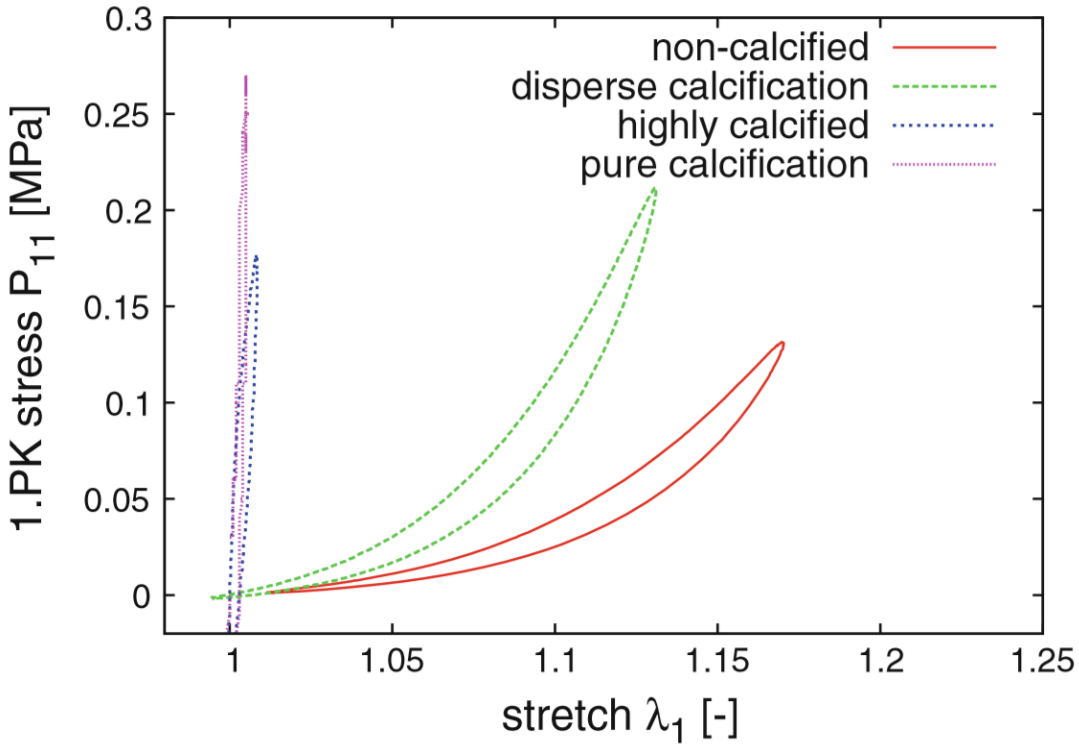

Figure 2.15: Stress-strain responses of freshly harvested human AAA walls with various degree of Ca under uniaxial cyclic loading (after 19 preconditioning cycles).
(Image source: Maier et al., 2010 [73])

Nevertheless, Maier et al (73) (2010) believed the contrary. With three patient-specific FEA models containing both the ILT and calcifications, they investigated the effect of progressive degrees of calcification on the computational wall stress in AAAs. Mechanical properties were also measured experimentally for various degree of calcification, as shown in Figure 2.15. An almost linear elastic behavior with little hysteresis was obtained for most calcifications, with Young's modulus ranging from 40 MPa (highly calcified AAA tissue) to 450 MPa (pieces of pure Ca from AAA). It is speculated that the density, dimension, as well as the micro-structure of Ca contribute to such a wide range of mechanical strength. Besides, the notion of higher rupture risk due to Ca was doubted. Specifically, an up-to-59.2% increase in the computed average wall stress was found assuming all Ca were absent, implying a significant load-bearing effect of Ca to the adjacent wall. The authors also observed that the highly calcified regions mostly match with the locations displaying high stress in the absence of Ca, suggesting a biological process of wall remodeling in which Ca assists in withstanding AAA deformation. Since large Ca were mostly

located in the concave bulge and affected the shape of AAA, the authors concluded that neglecting large calcification in AAA modelling may lead to crucial errors.

Thereupon, Raut et al. (2013) attempted to address these contradicting discoveries from computational studies in a literature review (184). As the modelling approaches for Ca were quite different, for example Speelman et al. modelled Ca by modifying the material properties of neighboring wall elements, Li et al. embedded Ca within the wall itself, whereas Maier et al. embedded Ca in the ILT region, it is speculated that these subtle differences could greatly affect the simulated wall stress due to the nature of very thin wall with large compliance mismatch (with Ca). Moreover, the demand for proper material models in aortic Ca simulations was underlined. A more recent later literature review in 2018 (185), Farotto et al. also pinpointed the role of Ca on the biomechanics of AAA being not completely clear, as the results from computational studies were highly dependent on modelling assumptions.

Although mechanical properties of Ca are of critical importance to the AAA wall stress analysis, relevant experimental measurements remain very limited. The assumptions of isotropy, homogeneity, incompressibility and linear elasticity have been commonly adopted due to its similarity to bone tissue (186). However, large discrepancy in its elastic modulus has been reported, mainly due to the difference in Ca locations, the density (calcified tissue vs. pure Ca pieces), the status of specimens (fresh vs. dried samples) and measurement techniques (uniaxial tensile, biaxial tensile or nano-indentation). The elasticity moduli of Ca are reported in the range of 1.5 to 19 MPa for coronary arteries (187,188), 7.9 to 17.3 MPa for iliac arteries (74), and 1.4 MPa to 20 GPa for AAAs (27,71,73,75,76,189). In particular, the material parameters for Ca in many numerical studies were adopted from Loree et al (189) (1994) who reported a circumferential tangential modulus of 1.466 ± 1.284 MPa for calcified aortic atherosclerotic plaques, which was later speculated to be wrong by Maier et al. as it appeared even less stiff than non-calcified AAA tissues (73).

An in-depth analysis of the composition, morphology and mechanical property of Ca in AAA has been performed by Marra et al. in 2006 (27). Calcium deposit specimens were removed from AAA tissues harvested from open surgeries. Results indicate that vascular calcifications are mainly composed of calcium and phosphorus, similar to hydroxyapatite and appeared as spherical crystals

growing along the direction of blood flow. Testing dehydrated specimens with nano-indenter, the authors obtained an average hardness of 710 MPa which is similar to that of iron, and an average elastic modulus of 20.5 GPa (Poisson's ratio 0.4) which is five times less than that of pure hydroxyapatite, but three orders of magnitude greater than that of AAA wall measured by Raghavan ML in 2000 (159). Moreover, small sensitivity of the Poison's ratio on the elastic modulus of Ca was revealed. With this significant mismatch in stiffness between Ca and AAA wall, they concluded that Ca can elevate wall stress in AAA, thereby increasing both the rupture risk and challenge in AAA repair.

More recently, the research groups of O'Leary et al. (2015) (190) and Barrett et al. (2018) (191) performed experimental characterization on the mechanical strength and failure properties of calcified AAA tissues harvested from open surgeries. O'Leary reported that the failure properties of tissues with Ca were significantly weaker than those of fibrous tissues (no Ca), where the junction between Ca and the tissue network appeared highly susceptible to failure, confirming a critical role of Ca in AAA rupture. Besides, they also observed that Ca were mostly distributed along the rim of adventitia rather than within the ILT. On the other hand, Barrett et al. found an averaged increase of 174% in peak strain and 18.2% in peak stress for tissues with Ca, indicating the mismatch in compliance between stiff Ca and distensible walls, which may also increase the risk of AAA rupture. Nevertheless, both studies did not conduct quantitative characterizations of Ca in their samples, and all samples were taken from the anterior wall of AAA due to surgical limitations.

2.3.4 Surrounding tissues

The biomechanical role of AAA surrounding tissues has not been studied extensively, relevant experimental and computational findings remain very limited. It is often omitted or oversimplified with assumptions, especially in numerical simulations, partially due to the diversity in morphological characteristics and complexity in modelling.

An in-depth analysis on the mechanical properties of human abdominal adipose tissues were conducted for the first time in 2013, using both uniaxial and biaxial tensile tests (Fig. 2.16), as well as triaxial shear measurements (192). Sommer et al. have revealed the non-linear, anisotropic and viscoelastic characteristics of human abdominal fat, where the collagenous micro-structure plays a key role in this anisotropic behavior. As a result, a constitutive model for the corresponding hyperelastic behavior of the abdominal fat was proposed, providing a more accurate boundary condition for numerical analysis predicting clinical outcomes.

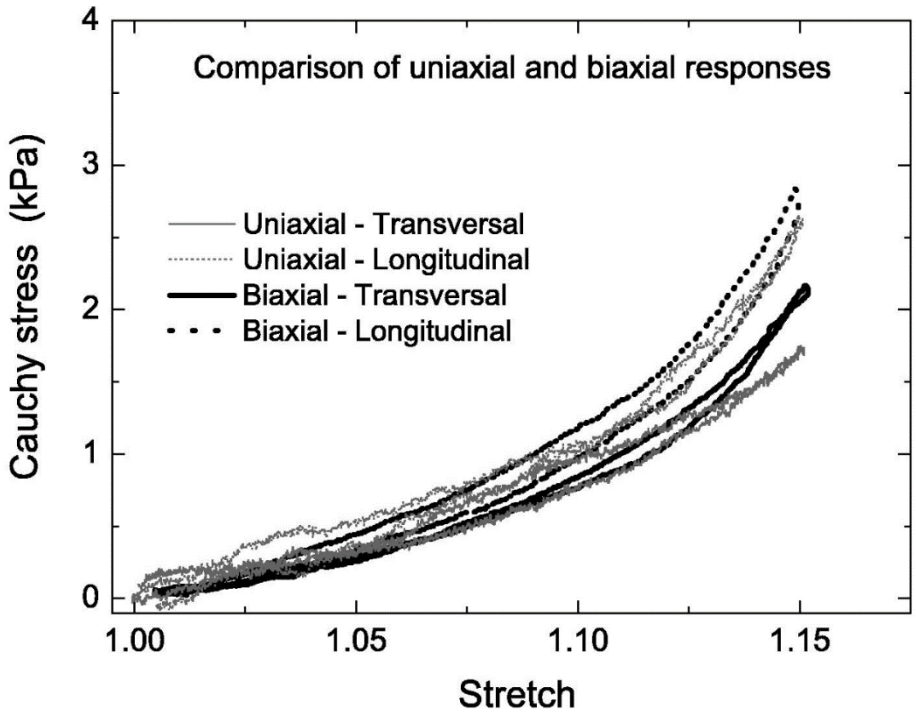

Figure 2.16: Comparison of the uniaxial and biaxial stress-strain behavior of a freshly harvested human abdominal fat, in both transversal and longitudinal directions.
(Image source: Gerhard Sommer et al., 2013 [191])

In 2013, Kim et al. developed idealized finite element models to study the biomechanical effects of surrounding tissues composed of PVAT and the outer layer of connective tissue for thoracic aorta (193). Their results indicated a mechanical homeostasis effect of the surrounding tissues to provide additional radial constraints on the aorta, thereby redistributing the wall stress circumstantially based on the variation in tissue thickness. Hence, the regional adaptation of aortic wall stress may be better estimated by including surrounding PVAT with corresponding thickness, in both healthy and pathological conditions. Two years later, Kwon et al. investigated the effect of surrounding tissues on the shape and curvature of AAA from longitudinal CT scans of ten patients (58). The authors revealed significant flattening effects on certain areas of AAA due to the interaction with spine throughout the evolution of growing AAA. Since AAA diameter is the main criterion for treatment decision in clinical practice, where small AAA also shows high mortality rates, it is suggested to consider AAA wall stress together with the inclusion of surrounding tissues for treatment planning.

2.4 Tissue-mimicking mockup for cardiovascular biomechanics

Better understanding the biomechanical interaction between the SG and the AAA is critical to ensure the overall quality of EVAR treatments. However, most biomechanical tests cannot be implemented directly with living human tissue, rendering the vascular mockup an interesting alternative. On the other hand, mockups can be standardized, allowing the experiment to be reproducible, and alleviating experimental limitations due to the cross-species and cross-specimens variability.

2.4.1 Synthetic polymer

Traditionally, mold-casted elastomer was commonly used in experimental research to replicate human vasculature. Silicone is a classical selection due to its compliancy, translucent nature, low cost and relatively easy fabrication process (194–198). As such, silicone vascular mockups have been often fabricated from biomedical industries for education, research, medical training and medical device benchmark testing (Fig. 2.17).

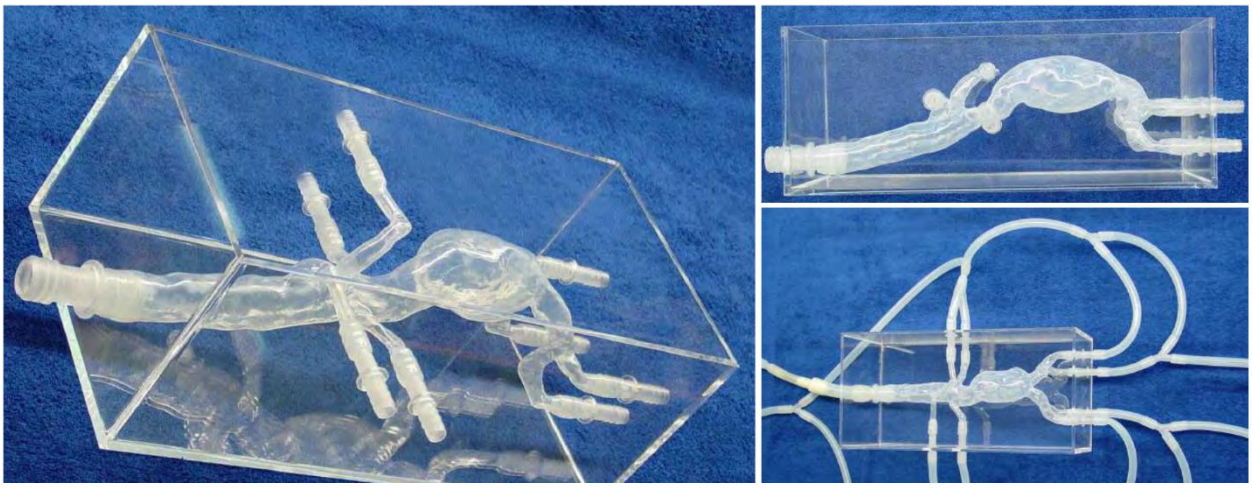

Figure 2.17: Commercial silicon mockup for AAA.

(Image source: Elastrat Sàrl, Switzerland, http://www.elastrat.ch/models/index.php?id=3)

Other materials such as polyurethane and epoxy resin have also been considered, especially for imaging modality (199) and hemodynamics studies (200). In 2013, Louise Allard presented a method to fabricate patient-specific AAA mockups and demonstrated decent match in imaging features with in-vivo data from magnetic resonance (MR) angiography, CT angiography and

ultrasound examinations. The mockup consisted of the manually molded AAA wall, ILT and surrounding tissue that were made of polyurethane, agar-glycerol gel and agar-oil gel respectively (Fig. 2.18). Although it exhibited relatively weak mechanical strength and thus only able to mimic small deformations, it could be of great value for different imaging modality calibrations (199).

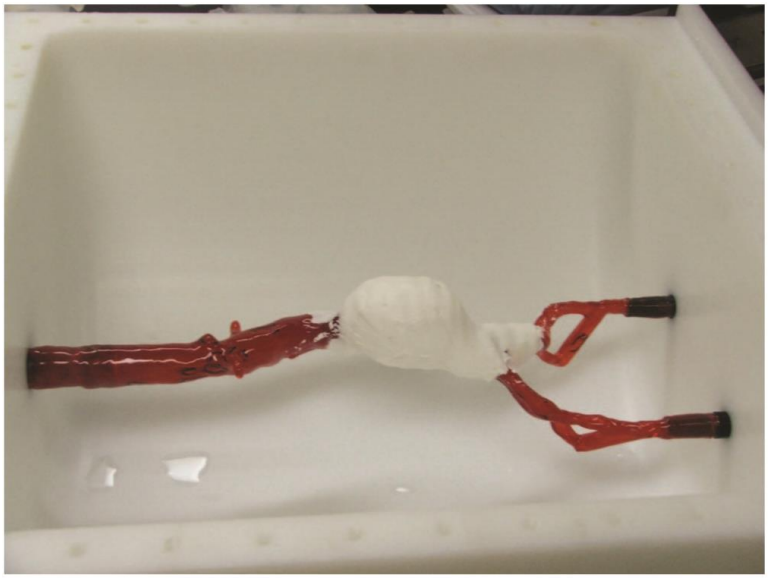

Figure 2.18: AAA phantom with polyurethane coated lumen (red region) and agar gel ILT (white region); agar-oil gel was later poured into the polyethylene container to mimic the abdominal space. (Image source: Louise Allard et al., 2013 [198])

More recently, the art of human vascular replica is brought to the next level thanks to the emerging development of rapid prototype technique. The invention of flexible rubber-like 3D-printed material provides a great range of mechanical strengths to mimic vascular tissues (201). This technique not only drastically reduces fabrication time and cost (202,203), but also overcomes the difficulty in reproducing more complete vascular networks with patient-specific geometry (204). In 2018, Andrzej Polanczyk et al. presented an ex-vivo system composed of a 3D printed patient-specific AAA model, with thrombus (same material as AAA wall) or SG, and a pulsating network reproducing realistic blood circulation, to study the hemodynamic effects due to the change in AAA spatial configuration (Fig. 2.19). Although it was a preliminary study which required further optimizations in the mockup design, this ex-vivo system has confirmed hemodynamically the protected effect of thrombus or SG in wall deformations and SG migrations (204).

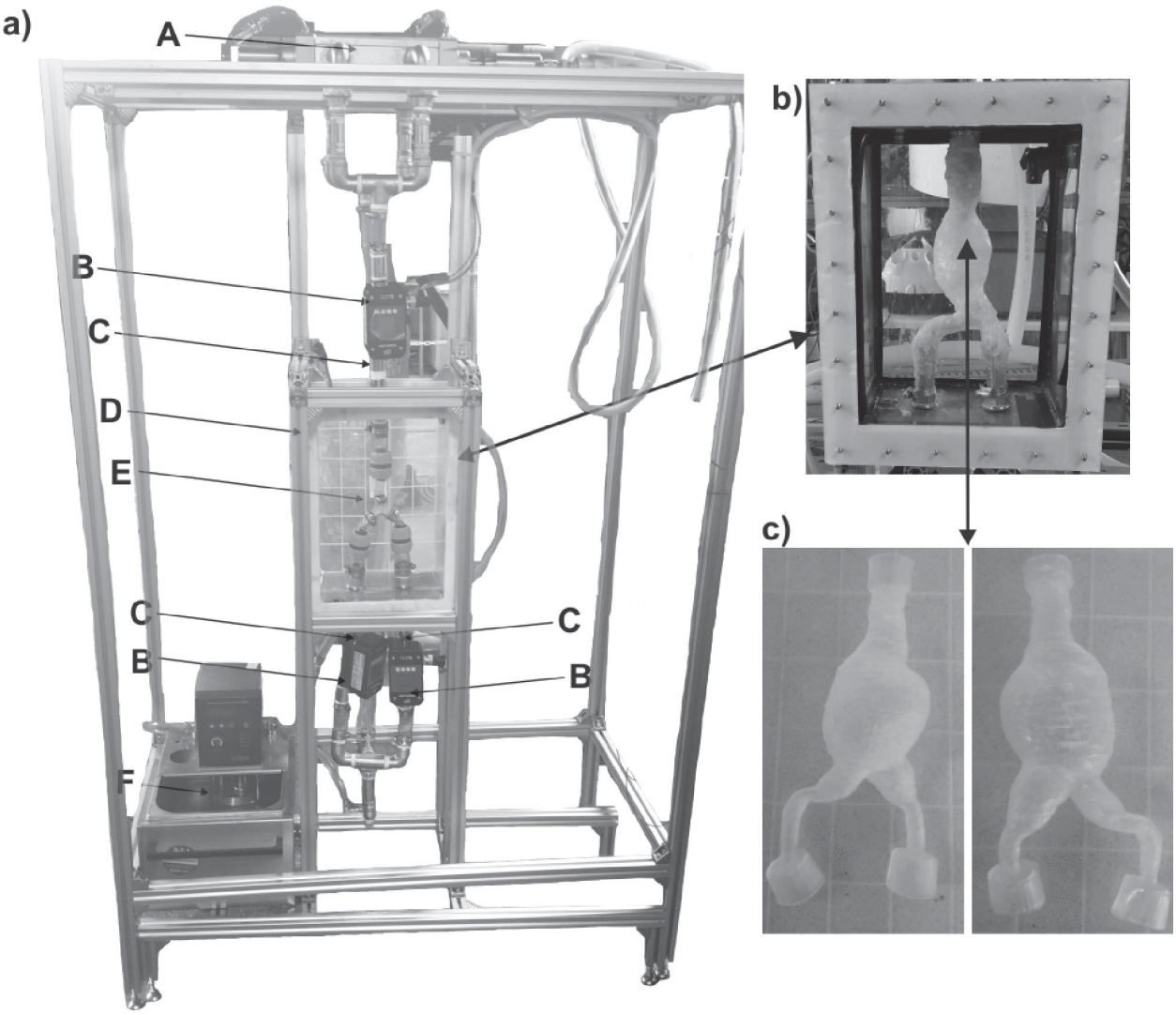

Figure 2.19: A system (a) with 3D printed flexible AAA phantom (b & c) connected to a circulating system to mimic pulsatile blood hemodynamic environment in human AAA. (A: pulsator; B: flow sensors; C: pressure sensors; D: transparent rectangular container; E: 3D flexible phantom of AAA; F: pump)
(Image source: Andrzej Polanczyk et al., 2018 [203])

Of note, limitations of current 3D printed vascular mockups remain, albeit the rapidly evolving technology, for example: printing accuracy due to printer resolution, surface roughness (compared to casted models) due to deposition layers (201), compatibility with different imaging modalities (205), and poor friction behavior (casted polymer as well (197)) which is one of the determinant factors to accurately predict catheter tip trajectory [39].

2.4.2 Hydrogel

Although various tissue-mimicking materials have been used to provide a more controlled testing environment, the demand for a material with suitable friction property remains, as friction behavior plays a key role in endovascular device navigation and associated vessel damaging. Owing to the hydrophilic nature, the surface friction and interfacial energy of hydrogel in contact with biological fluid can be minimized (207), making it an ideal candidate to mimic the surface of human soft tissue. Besides, hydrogel has been well known not only for its adjustable mechanical strength, degradation kinetics and mass transfer properties, but also the biocompatibility that supports a wide range of cell phenotypes. Consequently, hydrogel has been considered in many biomedical applications such as tissue engineering, regenerative medicine and artificial implants (208).

Specifically, the cryogenic polyvinyl alcohol (PVA-C) hydrogel, having excellent compatibility with various medical imaging modalities (ultrasound, CT and MRI), is becoming a popular synthetic material for vascular mockup. The cryogenic treatment consists of a specific sequence of customized freezing-thawing cycles, resulting in a hydrogel with non-linear elastic behavior, which is essential for human vascular tissue. Repeated thermal cycling has been demonstrated to increase crystallinity in the hydrogel, thereby increasing its elastic modulus (209–214). By adjusting different parameters during the cryogenic treatment (number of the cryogenic cycles, freezing and thawing rate, duration at peak temperature, etc.), one can tailor the mechanical strength of PVA-C to mimic a wide range of biological soft tissues (215–218).

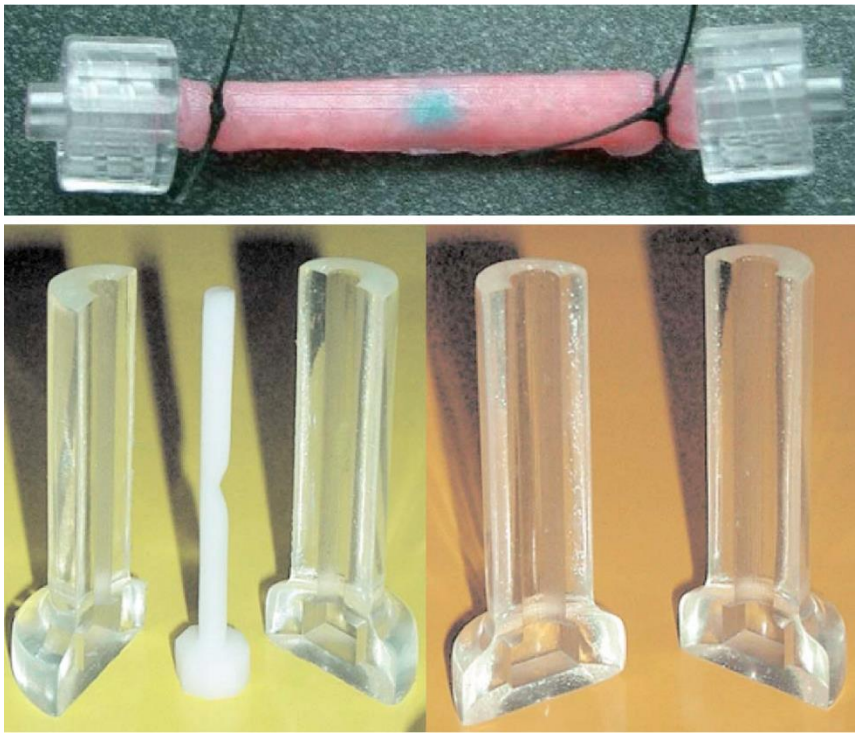

Figure 2.20: A double layered PVA-C mockup (top) mimicking coronary artery with a lipid inclusion (in blue); molds are shown at the bottom. (Image source: Valerie Pazos et al., 2010 [219])

Several studies have utilized PVA-C mockups to investigate human vascular biomechanics, from coronary to aortic arteries, with and without diseased characteristics. A research group led by Rosaire Mongrain has created a series of vascular mockups using PVA-C. In 2009, they performed uniaxial tensile tests to characterize the effect of cryogenic parameters on the non-linear-elastic behavior of PVA-C (219). The authors reported that PVA-C with 3 cycles could mimic lipid inclusion and that with 6 cycles was more suitable to represent the vessel wall, whereas no significant change in mechanical properties was observed beyond 6 cycles. Subsequently, a multi-layer PVA-C mockup mimicking simplified coronary artery segment with a lipid inclusion was created (220) (Fig. 2.20), in order to validate a numerical method determining the elasticity of the lipid inclusion (221). In 2012, they further incorporated various concentration of calcium carbonate into PVA-C specimen to mimic the mechanical behavior of coronary arteries with calcium deposits on the plaque cap (222). Their results indicated that higher concentration of calcium deposits greatly increased the stiffness of surrounding material, whereas the corresponding decrease in the fracture toughness might reflect the brittleness of specimen, potentially attributing to vascular rupture.

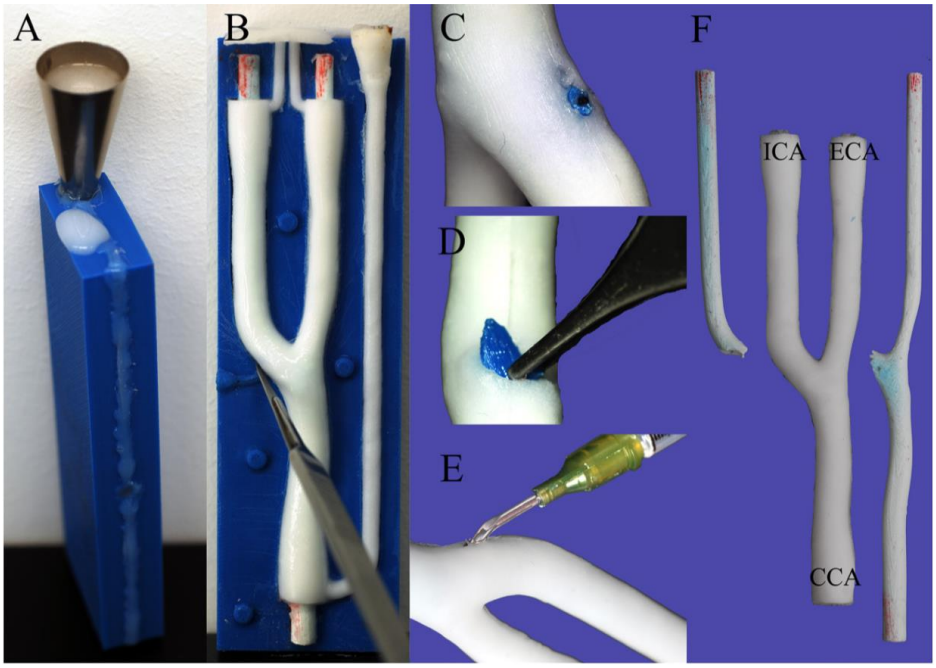

Figure 2.21: Phantom fabrication steps for a bifurcated carotid artery with an atheroma: A) seal outer molds (in blue) and inject PVA solution; B) C) D) after few thermal cycles, remove small ABS piece loosely attached to the mold; E) inject PVA solution into the empty space for subsequent thermal cycles to create atheroma; F) final PVA-C phantom after removing the inner molds (in white).

(Image source: Chayer Boris et al., 2019 [223])

Another group led by Guy Cloutier has also employed PVA-C mockups for vascular imaging analysis, with the addition of 3%wt of Sigmacell Cellulose as acoustic scatterers to improve ultrasound detection. In 2010, they developed PVA-C mockups in tubular shape with various thickness and inclusions (made of softer PVA-C) to mimic coronary arteries with atheroma plaques, in order to evaluate a new imaging approach detecting vulnerable plaque in vivo (223). Few years later, this mockup design was further modified with a more complex geometry to mimic a bifurcated carotid artery with stenosis (Fig. 2.21), for flow imaging and elastography analysis (224).

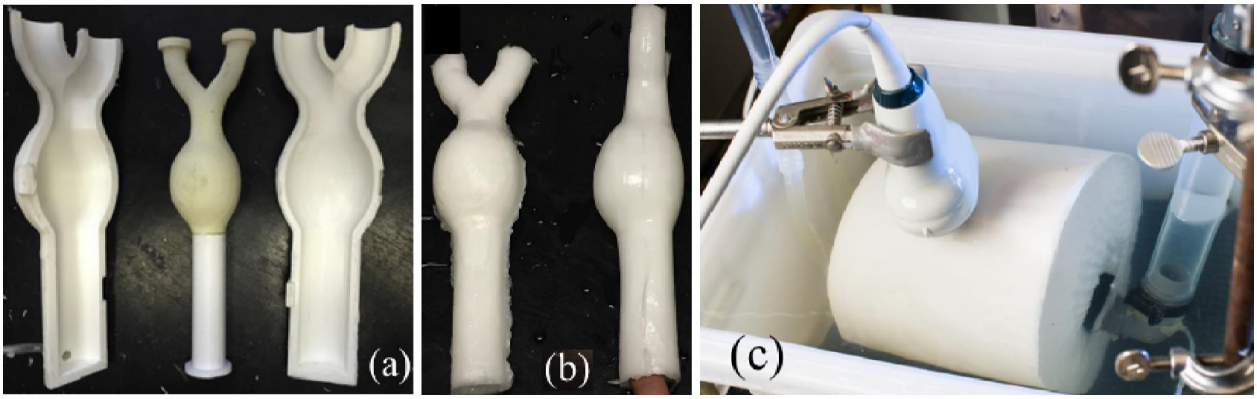

Figure 2.22: PVA-C phantom for AAA in uniform thickness with bifurcation: a) inner and outer molds; b) final PVA-C phantom; c) a set-up to encase the phantom, reproduce a general retroperitoneum space and a hemodynamic environment. (Image source: Doran S. Mix et al., 2018 [224])

More recently, another group led by Michael Richards has developed a PVA-C mockup to identify high-risk AAAs with ultrasound elastography (225) (Fig. 2.22). Unlike the previous group, they used 0.2%wt of Calcium Carbonate as ultrasound scatterers. A thick tube made of softer PVA-C were placed around the aneurysm to simulate retroperitoneum tissues, and a hemodynamic pump was connected to reproduce physiologic cyclic pressure and flows. Although the mockup provided a dynamically realistic environment, the AAA geometry was considerably simple and diseased characteristics (ILT and Ca) were absent.

2.5 Limitations in current knowledge

To the best of the author's knowledge, the role of AAA biomechanics in EVAR assessment, considering the combined effects from all major AAA characteristics, has never been elucidated comprehensively. This is in part due to the fundamental knowledge of certain AAA characteristics remains unclear, controversial or poorly addressed. Gaps in the current knowledge can be summarized in, but are not limited to, the following areas.

2.5.1 Morphological characteristics of calcification

Various methods to characterize the amount of Ca have been employed in literature. Nevertheless, no qualitative and quantitative analysis has been done on Ca for human AAA, for example its extent, locations, configurations and distributions. Such analysis may not only complement the pathophysiological knowledge of vascular Ca, but also provide essential background to understand the failure mechanics in AAA rupture.

2.5.2 Biomechanical role of calcification

Albeit the numerous attempts to identify the biomechanical role of Ca in AAA, findings remain inconclusive: some consider Ca as a stress shield stabilizing AAA wall from rupture, whereas others argue that Ca creates strong stress gradient and promotes vessel failure. As one of the major pathological characteristics of AAA, Ca may affect not only the wall biomechanics itself but also the interaction with endovascular devices. As such, understanding the effects of Ca in EVAR assessment may help to shine a light back on the exact role of Ca in AAA wall biomechanics. Moreover, the association between Ca density and the corresponding manifestation in different clinical imaging system has not been elucidated, which may play an important role in determining its material strength and subsequently, the biomechanical response.

2.5.3 Effect of surrounding tissues

Unlike other AAA characteristics, the biomechanical effects from surrounding tissues have received far less attention. In computational studies, it is either omitted or oversimplified as a single boundary condition. On the other hand, most AAA mockups are developed without

considering the surrounding structures (199,203,226) due to the challenge in developing relevant experimental models. Being a massive compartment offering different mechanical support directly to the AAA (spine vs. surrounding fat), surrounding tissues may be a critical factor to better understand the biomechanical interaction of AAA with endovascular devices.

2.5.4 In-vitro EVAR analysis

To date, most vascular mockups have been developed to address a single or few parameters in questions. For example: transparent but relatively rigid mockups made of polyurethane or epoxy resin for hemodynamics studies (199,200); compliant mockups made of mold-casted silicone (196–198) or hydrogel (220,224,225) for medical imaging and computational validations, but often in simple geometry; 3D-printed flexible mockups in complex geometry for medical trainings and benchmark testing, but with less desirable mechanical properties (203,204). On the other hand, surrounding structures and pathological characteristics are still rarely considered due to the complexity in mockup development. Hence, an anthropomorphic mockup (AMM) representing the major mechanical, anatomical and pathological characteristics of AAA as well as surrounding tissues is in demand.

3

QUANTITATIVE AND QUALITATIVE ANALYSIS OF CALCIFICATION IN AAA

In this chapter, the quantitative and qualitative analysis of Ca in AAA is presented. Specifically, the motivations, assumptions, patient selection criteria and clinical data collection are discussed. A novel strategy to characterize Ca in AAA is proposed, followed by both statistical tests and finite-element models to analyze potential effects of Ca. Being an integral part of the current research, this strategy not only tackles the ambiguous role of Ca from a different angle, but also outlines some significant characteristics of Ca in AAA for the first time.

3.1 Motivations

Calcified deposits in the aortic wall create geometric heterogeneity that can alter the mechanical behavior of AAA. Although numbers of studies have been focused on this topic, the biomechanical role of Ca remains inconclusive: some consider Ca as a risk factor for AAA rupture as it may increase the peak wall stress, whereas others suggest a load-bearing effect as the Ca may stabilize the adjacent wall. Beside the intrinsic properties, some clinical studies speculate a nontrivial role of Ca locations, as well as the proportion of Ca in AAA, for the success of EVAR during device navigation (42,44), SG fixation (45,46) and post-treatment vessel remodeling (42,48). Nevertheless, without a comprehensive understanding of the Ca morphological characteristics in AAA, it would be impossible to validate any hypothetical role of Ca in AAA biomechanics and the interaction with endovascular devices.

3.2 Methodology

3.2.1 Patient Selection & Clinical Data Collection

In order to maximize the sample size and present the complete spectrum of AAA population (regardless of age, gender and ethnicity), patients from multiple database used in our previous AAA projects (Online, Offline, Rigid, Elastic, Croissance, Halifax and 2D3D) were evaluated. All those patients have been informed for being registered anonymously in the database. Most recent data from 2010 to 2019 was considered, and all study protocols have been approved by CHUM ethics committee.

In this study, 3D models reconstructed from clinical CT scans were the foundation of the quantitative and qualitative analysis. As such, adequate image resolution from all clinical CT scans was the key criterion while selecting our patient group. Specifically, only those with both slice thickness and voxel spacing below 1 mm were considered. Moreover, CT scans must well cover the region of interest (ROI) for this study (specification explained in the following section 3.2.2). On the other hand, the availability to access pre-operative evaluations (blood tests, BMI, comorbidities, medication used, etc.), peri-operative and follow-up reports was another important criterion. Of note, patients with inherited defects in connective tissues were also excluded. As a

result, around 25% of patients from those database were excluded, and a total number of 103 AAA patients were finally selected, in which 53 have undergone EVAR (open surgery, thoracic, fenestrated, multiple-branched SG were all excluded). For the EVAR patients, 3D models were created based on their pre-operative scans, whereas for all other patients, the latest scans were utilized. As a result, the morphological characteristics of Ca in AAA (Ca volume, locations and shapes) could be outlined using these 3D models.

Clinical data describing the patient demographics, comorbidities, EVAR procedures and complications were also retrieved from medication indications, blood and imaging analysis, as well as clinician reports. All collected data used in this study have been verified by at least two medical specialists.

- For demographics, gender, age, AAA diameter, smoking history (current, former or non-smoker) were collected and the corresponding body mass index (BMI) were also calculated.
- For comorbidities, the status of hypertension, diabetes, dyslipidemia (DLP), coronary artery disease (CAD), peripheral vascular disease (PVD), chronic obstructive pulmonary disease (COPD) and chronic kidney disease (CKD) were determined for each patient. To minimize any bias resulting from incomplete health records, more than one measures were considered for certain comorbidities. For example: prescribed medications and blood pressure records were used to evaluate the hypertension status; medications and glycemia records were taken into account for the diabetic status; New York Heart Association (NYHA) classification, echocardiogram and stress test reports, anesthesia records were examined to verify the CAD status; glomerular filtration rate (GFR), pre- and post-operation creatinine profile were all considered for the CKD status.
- For EVAR complications, all surgical reports and follow-ups up to 3 years were reviewed, and events such as peri- or post-operative endoleaks (Type IA, Type IB, and Type II) and limb thrombosis (iliac occlusion) were recorded. Moreover, the surgery duration, fluoroscopy time and total iodine used were collected to evaluate the procedural complexity.

Finally, the effects of Ca on patient demographics and comorbidities were studied using 3D models from all AAA patients, whereas the effects on EVAR success, in terms of complications and procedural complexity, were analyzed using 3D models from EVAR patients only.

3.2.2 Quantitative Analysis

In order to eliminate observer dependent outcomes, a semi-automatic segmentation approach was proposed to quantify Ca in AAA. For each patient, all analysis was focused at the ROI setting from 1 cm above the highest renal artery to 5 cm below the iliac bifurcation. Afterwards, both Ca and AAA wall were segmented and reconstructed via snake evolution using ITK-SNAP (version 3.6.0), the corresponding Ca volumes and ratios could then be calculated for further analysis.

3.2.2.1 Calcification & Wall Segmentations

As explained in Chapter 2, the threshold distinguishing Ca from its surrounding can vary from 130 to 1000 HU, depending on the injection of contrast agent. Most high resolution CT angiography study are done after contrast injection. The density of the enhanced lumen is usually ranging between 150 and 450 HU. Although the patient-specific threshold yields more accurate results, it is a rather non-practical approach, given the fact that the image intensity of Ca varies with the density of calcium, which is a variable with the age and gender; besides, this intensity is also very susceptible to the operator variability. For those reasons, it is essential to select a threshold value capturing most of the data from our patient group. Hence, 500 HU as a central value, which has also been suggested in some studies (174,227), was tested for scans with and without contrast, from different facilities, for patients in different age and gender. Based on our visual inspections, the edge of Ca appeared blur with the threshold set below 480 HU; while increasing the threshold above 520 HU, the size of Ca shrank rapidly, implying an overestimation of the threshold. Consequently, 500 HU was defined as the lower bound limit for all Ca segmentations in this study.

Accordingly, 130 HU was applied as the upper bound limit to segment the luminal side of AAA, from which the entire AAA wall could then be reconstructed by assuming a uniform thickness. As mentioned above, 130 HU is also the lowest image intensity for Ca; therefore,

partitioning the image by intensity lower than this value should be able to clearly exclude any calcified deposits from the aortic wall.

3.2.2.2 Calcification Volumetric Ratio

Once 3D models for all Ca inclusions within the ROI were reconstructed, the total Ca volume for a patient could be obtained by summing up the volumes of those Ca inclusions. Keeping in mind that limited spatial resolution from clinical scans (as oppose to micro CT) could hamper visualization of small objects, and that patient-specific thresholds were not considered here, the reconstructed models of Ca might slightly vary from the actual size, yet sufficiently reflect the morphological trends of Ca from our AAA patients.

In order to provide a better insight into the extent of Ca regardless of the aortic vessel size, the Ca volumetric ratio, a dimensionless representation was sought. For each patient, the total Ca volume was normalized by the volume of aortic wall within that ROI, assuming a uniform wall thickness of 2 mm and the absence of all side branches (even the renal arteries).

3.2.3 Qualitative Analysis

To date, studies of Ca in AAA have been greatly focused on quantitative data. Non-quantifiable information, such as Ca locations and geometric configurations (or shape), has been suggested critical for EVAR assessment, but still rarely been investigated. As such, not only quantitative data but also qualitative measures were considered in this study. Specifically, at different locations along the AAA, the distributions of Ca volumes as well as the presence of different Ca shapes were evaluated, to draw a complete spectrum illustrating the morphological characteristics of Ca in AAA. Statistical analysis was then performed to unravel any significant effects of those characteristics.

3.2.3.1 Location

Endovascular interventionists have reported the aortic Ca being very critical for EVAR when it is heavily located in certain areas of the AAA. For example, catheter navigation may become difficult with excessive Ca along the iliac arteries and around the bifurcating area, causing iliac

thrombosis or rupture (42,44); Ca around the renal artery ostia may impair SG fixation and apposition at the neck, resulting in Type IA endoleaks (45,46); heavy Ca on the aneurysmal wall may also impede AAA size reduction after EVAR, leading to endotension over time with a high risk of AAA rupture (55,56). Thus, according to the above-mentioned potential effects on EVAR, locations of Ca were classified as follows (Fig. 3.1).

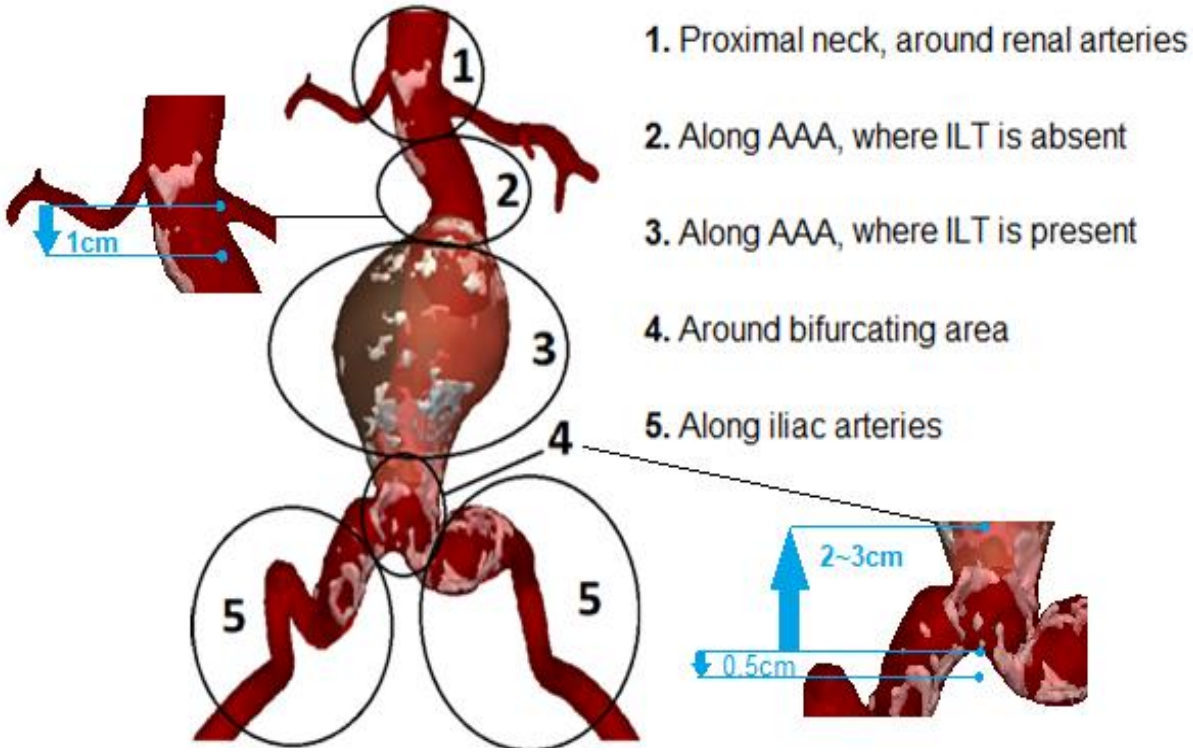

Figure 3.1: Classifications for five different locations along AAA, according to the potential effects on EVAR.

More precisely, location 1 begins from the top of ROI to about 1 cm below the lowest renal artery ostia; location 2 starts from the end of location 1 all the way till 2~3 cm above the lowest point of bifurcation; in the case with an ILT, location 2 becomes smaller as the region covered by ILT is excluded, referred to as location 3; location 4 continues from the end of location 2 to about 0.5 cm distally bellow the lowest point of bifurcation; finally, the rest belongs to location 5. Of note, a different sample size (n=73) was considered for Ca statistical analysis at location 3, given the fact that ILT was present in 71% cases.

At each location, a binary classifier was utilized: "1" refers to the presence of Ca, "0" indicates no Ca at that location. As a result, the occurrence of Ca at a specific location for a given patient group (mild, medium, heavy, severe Ca or all patients) could be determined as follows.

$$Location\ occurrence\ (\%) = \left[\frac{sum\ of\ binary\ values\ at\ 1\ location}{numer\ of\ patients\ in\ that\ group}\right] \times 100$$

(Equation 1)

3.2.3.2 Shape

In three dimensional space, all geometrical configurations are composed of faces, edges and vertices that are characterized by the x, y and z Cartesian coordinates. Accordingly, the maximum length, width, and thickness of a 3D object can be well defined. Of note, like many other biological tissues, Ca often grow into very complex and irregular shapes. Thus, further classification into simplified geometrical models are required to better elucidate any geometrical role of Ca on the AAA biomechanics. As explained in Chapter 2, the development of aortic Ca is believed to be an active cell-regulated process initiated from the media and promoted by VSMC apoptosis and elastic lamina degradation. For this reason, calcium tends to aggregate circumferentially and longitudinally along the aortic wall, rather than radially through the wall. More specifically, at a macroscopic scale, the change in Ca dimension could be relatively planar and constrained by the thickness of aortic wall, where the expansion in length and width is unrestricted. Therefore, by fitting uniform cubes (edges equivalent to Ca thickness) into our 3D Ca models, three types of arrangements could be generally expected: 1) a single cube; 2) a cuboid composed of multiple cubes in a line; 3) a plate composed of multiple cubes on a single surface (Fig. 3.2). According to our visual inspections, all 3D Ca models can well fit into these geometrical arrangements and hence, the classification of Ca shapes for each patient was proposed as follows.

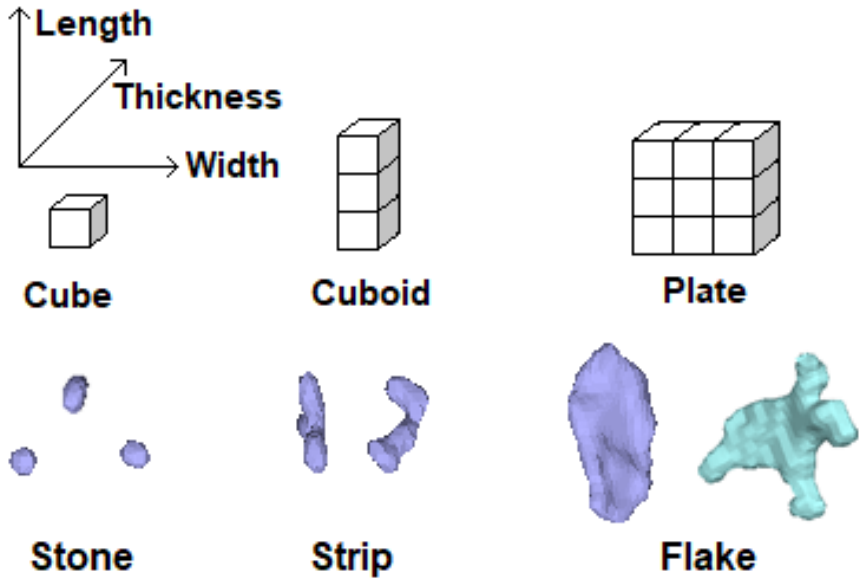

Figure 3.2: Classifications for Ca in different geometrical configurations: cubical illustrations (top) and the actual Ca models (bottom).

- ***Stone (cube)***: small spherical or cubical shape, with length ≈ width ≈ thickness
- ***Strip (cuboid)***: long curvy/spiral shape, oriented vertically or horizontally, with length ≥ 3 × width, width ≥ thickness
- ***Flake (plate)***: large shell-like shape (circular, rectangular, triangular or amorphous), with length ≥ 3 × thickness, width ≈ length

For a specific shape at each location, a binary classifier was also utilized: "1" refers to the presence of Ca in that shape, "0" if no relevant Ca at that location. Therefore, the occurrence of a specific Ca shape at each location for a given patient group could also be calculated as follows.

$$Shape\ occurrence\ (\%) = \left[\frac{sum\ of\ binary\ values\ for\ a\ specific\ shape\ at\ a\ single\ location}{numer\ of\ patients\ in\ that\ group}\right] \times 100$$

(Equation 2)

In addition, the sum of these binary values obtained from all five locations could reveal how widespread a specific Ca shape was across the AAA. Hence, the extensiveness (level of widespread) of a specific Ca shape for a patient could be defined as follows.

$$Shape\ extensiveness\ (\%) = \left[\frac{sum\ of\ binary\ values\ for\ a\ specific\ shape\ in\ all\ 5\ locations}{5\ (the\ case\ where\ this\ shape\ is\ present\ in\ all\ 5\ locations)}\right] \times 100$$

(Equation 3)

Accordingly, the proportion of this Ca shape for a specific AAA could also be obtained. Note that the following formula only illustrates the proportion of Ca stone, but the same was applied for the proportion of Ca strip, as well as Ca flake.

$$Ca\ stone\ proportion\ (\%) = \left[\frac{Ca\ stone\ extensivity}{sum\ of\ Ca\ stone, strip, flake\ extensivities}\right] \times 100$$

(Equation 4)

It is speculated that concentrated small Ca inclusions may weaken the aortic wall and increase rupture risks, whereas a large Ca flake may reduce the stress in the adjacent wall (72). Moreover, strip is another interesting shape as it may create relatively sharp edge that initiates vessel tearing.

3.3 Analytical Results

3.3.1 Calcification Volume

The distribution of total Ca volume appears non-symmetrically bimodal, as shown in Figure 3.3: relatively uniform below 3 cm^3, then spread in a wide range after 3 cm^3 with outliers greater than 15 cm^3. Corresponding Ca volume ratios are also indicated. The uniform distribution implies an equal opportunity of having total Ca volume less than 1 cm^3, between 1~2 cm^3 and 2~3 cm^3. Hence, Ca models are classified accordingly into mild (Ca volume < 1 cm^3, volume ratio <3%), medium (1~2 cm^3, 3%~6%) and heavy (2~3 cm^3, 6%~10%) for analysis. Beyond this range, all Ca models are classified as severe (>3 cm^3, >10%). Our results confirm the presence of Ca in all AAA patients, and highlight that attention should still be drawn to the severely calcified cases (~25% of population).

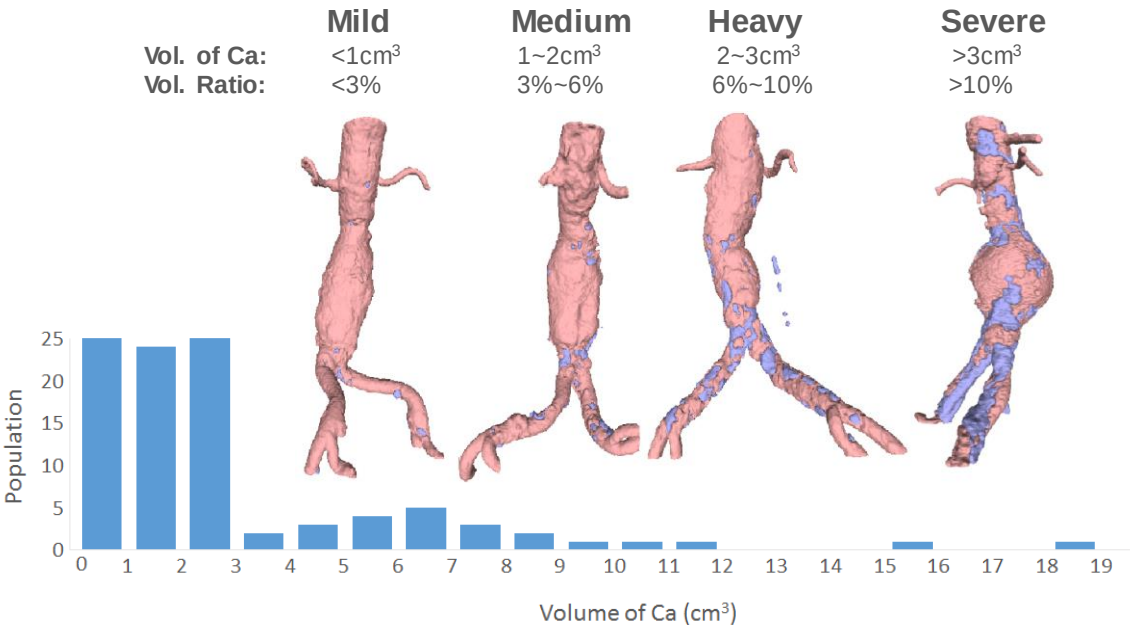

Figure 3.3: AAA models representing various extents of Ca (lumen in pink, Ca in purple) and distribution of Ca volume for all patients. (Population: the number of patients)

3.3.2 Calcification Locations

As illustrated in Figure 3.4, the iliac artery is the most common location regardless of the Ca loads, and the aortic bifurcation area is the second popular location for Ca accumulation. One interesting observation is that, upon reaching the medium Ca load, Ca always exists at these two locations which are very critical for catheter navigation, underlying the importance to understand the biomechanical effect of Ca at those locations. Around the proximal neck area and the aortic wall without ILT, Ca accumulation increases as the AAA becomes more calcified. While the ILT is present, Ca is rarely found on the luminal side but mostly lateral to the ILT, and the chance of having Ca at this location remains consistently the lowest. The surprisingly low Ca accumulation at this location suggests a protective effect of ILT against aortic Ca development. Moreover, a different pathogenesis for Ca at this location is also speculated as it appears relatively insensitive to the overall Ca loads along the AAA.

One interesting observation, Ca accumulations for all patients (red line) are getting more and more intense from the AAA neck towards iliac arteries, resulting in a trend against the direction of blood flow. Meanwhile, being inversely associated with the size of vessels, this site-specific trend of Ca development may be closely related to AAA hemodynamic environment. More specifically, blood flow in the lower infrarenal region is comparably more resistive than that in the

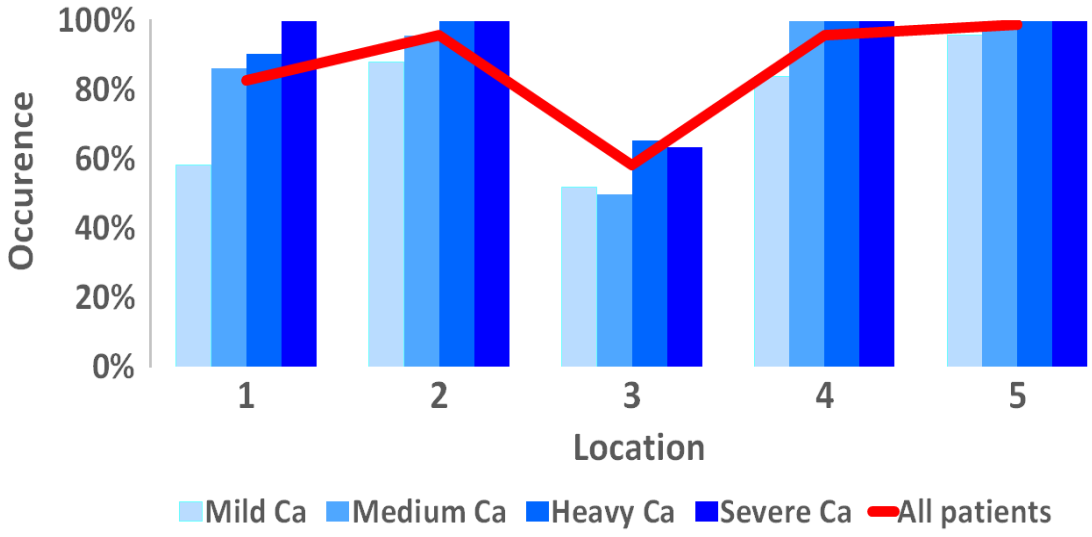

Figure 3.4: Occurrence of Ca at different locations of AAA, for all patients (red) and for each patient group of different Ca loads (different shades of blue).

proximal neck (228), as the peripheral flow resistance from lower limbs (tri-phasic, with a diastolic flow reversal phase (229)) is significantly higher than the renal vascular resistance (typical resistive index of 0.5-0.7 (230)). Furthermore, studies have reported that the locations of Ca along the thoracic aorta are not random, but rather associated with the shear stress and gradient related biomechanical responses (231–234). Therefore, a more comprehensive study is suggested in future, considering both the hemodynamic effects of blood flow and the bio-mechanically induced cellular pathways inside the aortic wall, to better understand the disease initiation and progression of aortic Ca.

3.3.3 Calcification Geometric Configurations

The occurrences of specific shapes found at each location for all patients are plotted at the top of Figure 3.5; the corresponding values for different patient groups (mild, medium, heavy and severe Ca) are also illustrated in the bar charts below.

For all patients, stone geometry is the most common Ca shape around the neck of AAA; whereas at the bifurcation and iliac arteries, the occurrence of Ca flakes becomes the highest. On the other hand, the chances of seeing Ca flakes and stones are very similar along the AAA with and without the presence of ILT. Of note, the change in Ca shapes predominance from the proximal AAA (stones) to the distal end (flakes), together with the Ca accumulation trend observed across different locations (discussed at section 3.3.4), can be crucial factors for EVAR assessment. Besides, these observations are also valuable to study the pathogenesis of aortic Ca, assuming most Ca flakes are originated from clusters of Ca stones along the circumferential and longitudinal directions. As for Ca strips, the occurrence remains consistently the lowest across all locations. Nevertheless, different orientations of Ca strips have been observed (horizontal, diagonal, vertical and long spiral strips) and the diagonal ones appear to be the most popular.

While looking at results for a specific Ca shape (across a column of bar charts in Fig. 3.5), one can observe the variation in prevalence of a specific shape associated with different locations and Ca loads.

- For the ***Ca stone***, the occurrences at most locations do not vary consistently with Ca loads, except at the aortic wall without ILT, where the occurrence gradually increases

with Ca loads, and reaches 100% in severely calcified cases. Around the renal artery ostia and the bifurcation, the occurrence is the highest in medium calcified cases; whereas at regions lateral to ILT and along the iliac arteries, it is the highest in heavily calcified cases. In contrast, the overall lowest occurrence of Ca stone is found at the aortic wall lateral to ILT in mild calcified cases.

- For the ***Ca strip***, the occurrence at each location always increases gradually with Ca loads, and reaches 100% at the aortic wall without ILT in severely calcified cases. Unlike Ca stone, the overall lowest occurrence of Ca strip is found around the renal artery ostia in mild calcified cases.
- For the ***Ca flake***, the occurrence at each locations also increases with Ca loads. Among all shapes, Ca flake appears more dominant as its occurrence reaches 100% at the bifurcation and iliac arteries in severely calcified cases, as well as the aortic wall without ILT in both heavily and severely calcified cases. Similar to Ca strip, the overall lowest occurrence is also around the renal artery in the mild Ca group.

While looking at results for a specific patient group (across a row of the bar charts in Fig. 3.5), one can determine the spatial trend of Ca shapes, and reveal the corresponding variation as AAA becomes more calcified. Hence, the most common scenarios for different Ca groups are listed as follows.

- ***Mild Ca***: Ca stones at the renal artery ostia and the aortic wall without ILT; Ca flakes lateral to the ILT, at the bifurcation and iliac arteries.
- ***Medium Ca***: Ca stones at the renal artery ostia and lateral to the ILT; Ca flakes at the aortic wall without ILT, the bifurcation and iliac arteries.
- ***Heavy Ca***: Ca stones at the renal artery ostia, lateral to the ILT and along the iliac arteries; Ca flakes at the aortic wall without ILT, the bifurcation and iliac arteries.
- ***Severe Ca***: Ca flakes at the renal artery ostia, lateral to ILT, around the bifurcation and iliac arteries; all Ca shapes at the aortic wall without ILT.

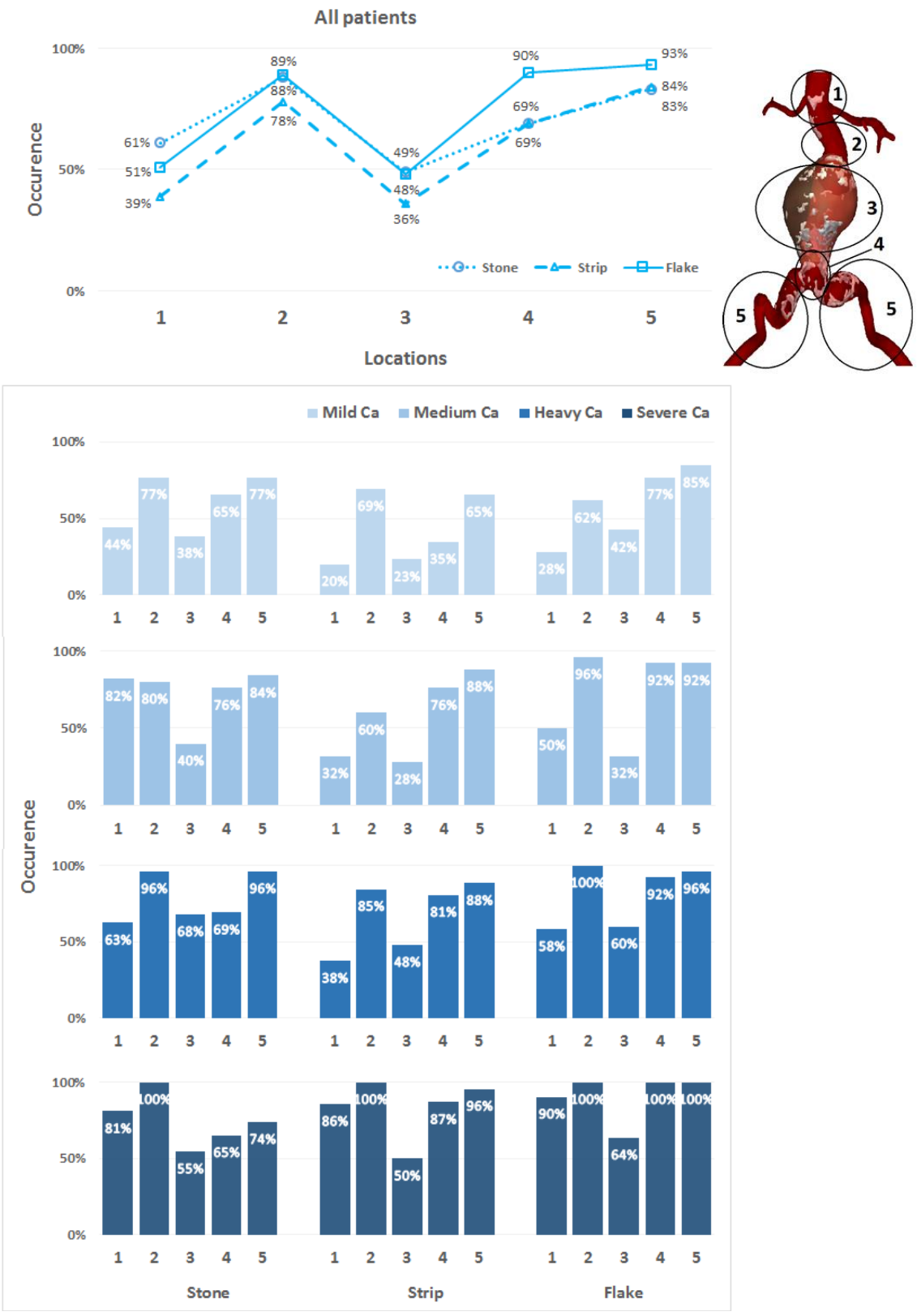

Figure 3.5: Occurrence of different Ca shapes at different AAA locations, for all patients (top plot) and for each patient group of different Ca loads (bottom bar charts).

For all patients, our results shown in Figure 3.6 indicate that flakes are the geometrical configurations most widely distributed (74% along the AAA), whereas strips appear to be the least (59% extensiveness). As AAA becomes more calcified, the extensivities of both flakes and strips gradually increase, with flakes being always more widespread but strips extending a bit faster. In contrast, Ca stone is initially the most widespread shape in mild calcified cases, but reaches its plateau in heavily calcified cases, then becomes the least widespread shape for severely calcified cases. Such a transition in shape extensiveness observed from mild to severe Ca may imply a potential growth pattern of aortic Ca, as a result of Ca stones gradually developing into flakes and strips. From a broader perspective, aggregate distribution (large flakes and strips) appears to replace the randomly diffused distribution (small stones). Keeping in mind that, Ca in eggshell form could act as a load-bearing shield on one hand, but impair the conformability of AAA aortic wall to vascular implants on the other hand. On the other hand, spiral Ca strips could constrain the interaction with delivery devices (catheters and guidewires). Further investigations on the biomechanical effects of Ca in specific shape will be critical to understand the contradicting role of Ca in AAA.

In addition, the change in shape proportions (Fig. 3.6, pie graphs) along the progression of Ca reveals another interesting fact: the proportion of stones decreases but that of stripes increases, whereas the proportion of flakes remains relatively consistent. It is therefore speculated that, along the evolution of Ca, the adjacent stones gradually grow into strips before aggregating into a large flake. As such, regardless of the overall lowest occurrence and extensiveness, Ca strip represents a non-trivial transitional shape during the Ca development.

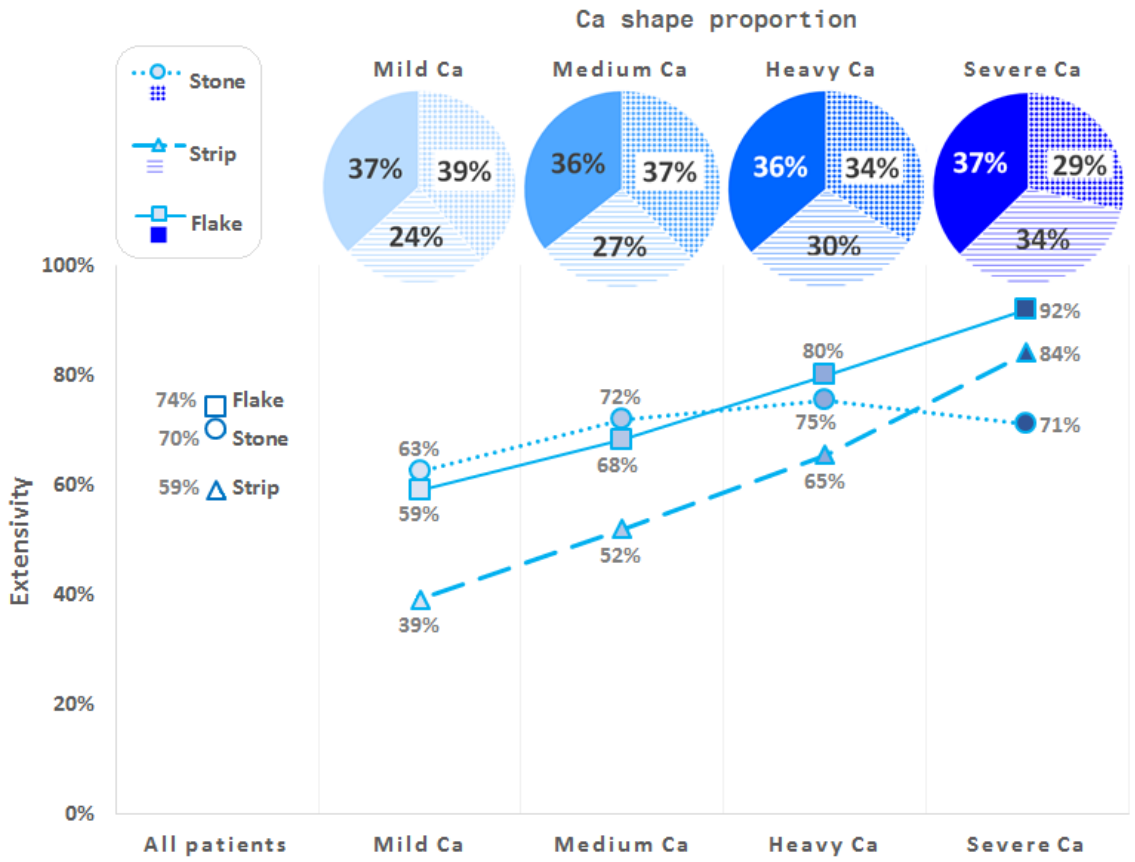

Figure 3.6: Extensiveness of different Ca shapes across the AAA for all patients, as well as for each patient group of different Ca loads (bottom plot); proportion of different Ca shapes in each patient group of different Ca loads (top pie charts).

3.3.4 Representative Models

Summarizing from the our observations regarding the morphological characterizations of Ca in AAAs, stones around the renal artery ostia, as well as flakes at the aortic wall without ILT, the bifurcation and iliac arteries are the most common scenarios. Better understanding the biomechanical effect of Ca in those scenarios may yield more accurate endovascular treatment predications. Hence, the following models (Fig. 3.7) representing those typical characteristics are proposed for EVAR assessment, which also provide main selection criteria for the patient-specific anthropomorphic mockup (AMM) in this study.

- Ca stones located around the renal artery ostia, to evaluate SG fixation;

- Ca flakes along the aortic wall without ILT, to evaluate the rupture risk and SG conformability;

- Ca flakes around the bifurcation and the iliac arteries, to evaluate the catheter navigation and risk of limb thrombosis.

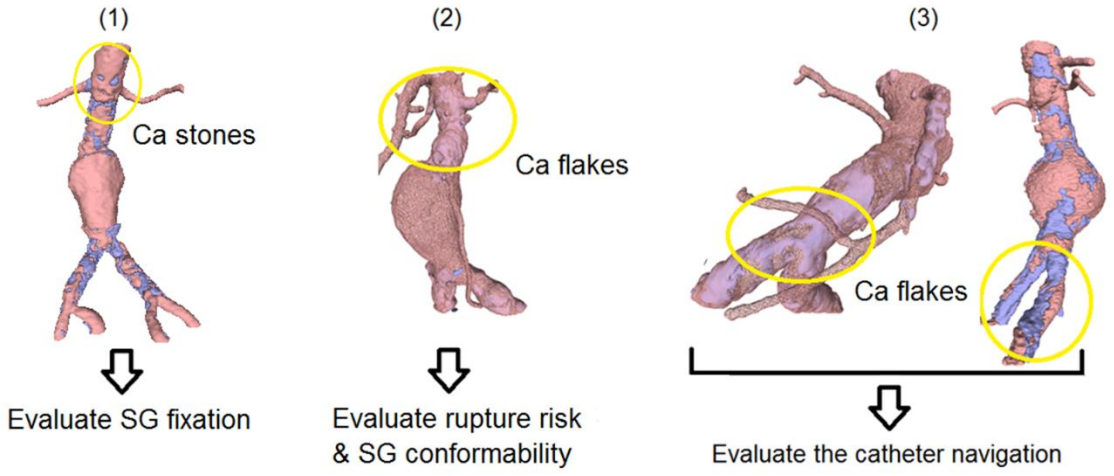

Figure 3.7: Representative models for EVAR assessment.

3.3.5 Statistical Analysis

Three types of scenarios were investigated for subsequent statistical analysis: considering a single, double or triple morphological factors. According to the above-mentioned morphological analysis, Ca volume, locations and shapes may not be independent variables and thus, conventional strategies such as multi-factor ANOVA or logistic regression are simply not ideal. Hence, a new variable representing the combined morphological characteristics was proposed for each scenario (except for the single-factor case), and univariate tests were then carried out to verify any significant difference in the comorbidities, EVAR complexity and complications. More specifically, Fisher exact tests were considered for nominal variables, and Student's t-tests were applied for continuous variables where appropriate. In addition, Bonferroni corrections have been applied where necessary.

3.3.5.1 Demographics, Comorbidities, EVAR Complications

Prior to analyzing any effects of Ca on endovascular treatments, patient demographics and comorbidities were studied for all patients as well as those underwent EVAR (Table 3.1). In agreement with the risk factors observed in general AAA population, all patients selected for this study show a predominance in males, elderlies (older than 70), those with smoking history, hypertension and dyslipidemia; whereas the prevalence of PVD, COPD, diabetes and CKD are significantly lower. Surprisingly, as a different vessel disorders with a common background, CAD appears to be a medium-risk medical condition.

	All patients (n=103)	EVAR patients (n=53)
Demographics		
Age [years]	74 ± 8.2	75 ± 8.2
BMI [kg/m^2]	28 ± 6.4	29 ± 7.2
AAA Diameter [cm]	5.8 ± 1.10	6.1 ± 0.93
Male	81%	89%
Current Smoker	36%	32%
Former Smoker	83%	87%
Comorbidities		
Hypertension	81%	75%
Diabetes	18%	23%
Dyslipidemia	70%	68%
CAD	42%	49%
PVD	30%	23%
COPD	27%	26%
CKD	20%	22%

Table 3.1: Demographics and comorbidities of all patients compared with EVAR patients. (n: sample size for that patient group; CAD: coronary artery disease; PVD: peripheral vascular disease; COPD: chronic obstructive pulmonary disease; CKD: chronic kidney disease)

In comparison to all patients, our EVAR patients have slightly larger AAAs, with much higher incidence in males have smoking history, diabetes and CAD. Besides, the prevalence of PVD in our EVAR patient group is relatively low. It is speculated that some cases with severe PVD were not yet considered for EVAR treatments, as the rupture risk in those very narrow vessels could be much higher during endovascular access and catheter navigation.

	EVAR patients (n=53)
Complexity	
Surgical duration [min]	160 ± 70.3
Fluoroscopy time [min]	28 ± 18.3
Total iodine [ml]	136 ± 59.5
Complications	**EVAR patients (n=53)**
Type IA	17%
Type IB	6%
Type II	23%
Limb thrombosis	9%

Table 3.2: Treatment complexity and complications for EVAR patients. (n: sample size for that patient group)

EVAR complexity and complications for all 53 patients are described in Table 3.2, with averaged iodine used, fluoroscopy time and surgical duration being 136 ml, 28 and 160 minutes, all within the standard range reported from literature (235). Note that patients underwent endovascular treatments other than abdominal-iliac SGs, for example fenestrated and branched grafts, were excluded from this analysis, as they required much longer surgery and were more prone to type I and III endoleaks. Complication rates are obtained by combining incidents noted from both perioperative and post-operative reports. Perioperative complications refer to the leaks observed during EVAR procedure, which have normally been treated before the operations end (except for a minor type II and a slight iliac occlusion which are reported but left untreated). Of note, some perioperative complications in this study, for example the Type I endoleaks that have been successfully fixed during the surgery, are usually not considered as complications in other clinical studies. However, those scenarios indeed reveal an increased level of EVAR complexity,

potentially due to Ca, therefore are also included in our study. On the other hand, post-operative complications are captured in a way similar to other clinical studies, based on the follow-up evaluations from one month up to three years after EVAR. In general, Type I & II are both very common cases in our patients. Specifically, Type IA is much more frequent than IB, and both mostly happened during EVAR (10 perioperative IA & IB; 2 post-operative IA). Besides, Type II is usually found in annual follow-ups (4 perioperative; 8 post-operative). Finally, limb thrombosis is not rare and often confirmed during follow-ups (2 perioperative; 3 post-operative). In conclusion, although a slightly high incidence of Type I endoleaks is reported here as we also consider the ones successfully fixed during EVAR, most data remain within the standard range reported from literature (149,153,236), which normally varies depending the surgical technique employed and SG designs.

3.3.5.2 Single Factor

First, to better understand the effect of Ca loads on AAA patient demographics and comorbidities, all patients are divided into Regular Ca (combining the mild, medium and heavy Ca) and Severe Ca groups. Results in Table. 3.3 reveals that older patients are associated with higher degree of Ca ($p=0.02$), whereas other differences in demographics and comorbidities owing to the variation of Ca extent are not significant.

Subsequently, EVAR patients are also divided into Regular Ca and Severe Ca, to illustrate the effects of Ca loads on surgical complexity and complications. Results in Table 3.4 confirms that the severity of Ca loads can significantly increase the difficulty of the EVAR procedure, with higher surgical duration ($p=0.03$), fluoroscopy time ($p=0.03$) and total iodine used ($p=0.04$). However, no significant effect can be found on EVAR complications while only considering Ca volume as a risk factor.

All AAA Patients	Severe Ca (n=26)	Regular Ca (n=77)	P value
Demographics			
Age [years]	**77 ± 7.9**	**72 ± 8.1**	**0.02**
BMI [kg/m^2]	28 ± 3.7	28 ± 7.1	0.87
AAA Diameter [cm]	5.7 ± 1.03	5.8 ± 1.13	0.69
Male	81%	80%	0.91
Current Smoker	33%	37%	0.78
Former Smoker	78%	86%	0.37
Comorbidities			
Hypertension	93%	76%	0.09
Diabetes	19%	18%	0.93
Dyslipidemia	78%	67%	0.34
CAD	41%	42%	0.89
PVD	33%	29%	0.76
COPD	15%	32%	0.13
CKD	24%	21%	0.83

Table 3.3: Comparison of demographics and comorbidities between Severe Ca and Regular Ca groups (from all patients). (n: sample size for that patient group; CAD: coronary artery disease; PVD: peripheral vascular disease; COPD: chronic obstructive pulmonary disease; CKD: chronic kidney disease)

EVAR Patients	Severe Ca (n=15)	Regular Ca (n=38)	P value
Surgical duration [min]	**193 ± 93.4**	**147 ± 57.3**	**0.03**
Fluoroscopy time [min]	**37 ± 27.2**	**24 ± 12.9**	**0.03**
Total iodine [ml]	**162 ± 56.1**	**126 ± 59.9**	**0.04**
Type 1a	27%	13%	0.25
Type 1b	7%	5%	0.89
Type 2	27%	29%	0.93
Limb thrombosis	20%	5%	0.13

Table 3.4: Comparison of EVAR complexity and complications between Severe Ca and Regular Ca groups. (n: sample size for that patient group; min: minutes)

3.3.5.3 Double Factors

To better visualize the combined effects of the extents and locations of Ca, an additional quantitative and qualitative measure is applied. Specifically, the locations of Ca are further simplified into superior (including location 1), center (including locations 2 and 3) and inferior (including locations 4 and 5), in which the corresponding ratio of Ca can be obtained for each new location as follows.

$$Ca\ Ratio\ (\%) = \frac{Volume\ of\ Ca\ at\ specific\ location}{Total\ volume\ of\ Ca\ within\ ROI} \times 100$$

(Equation 5)

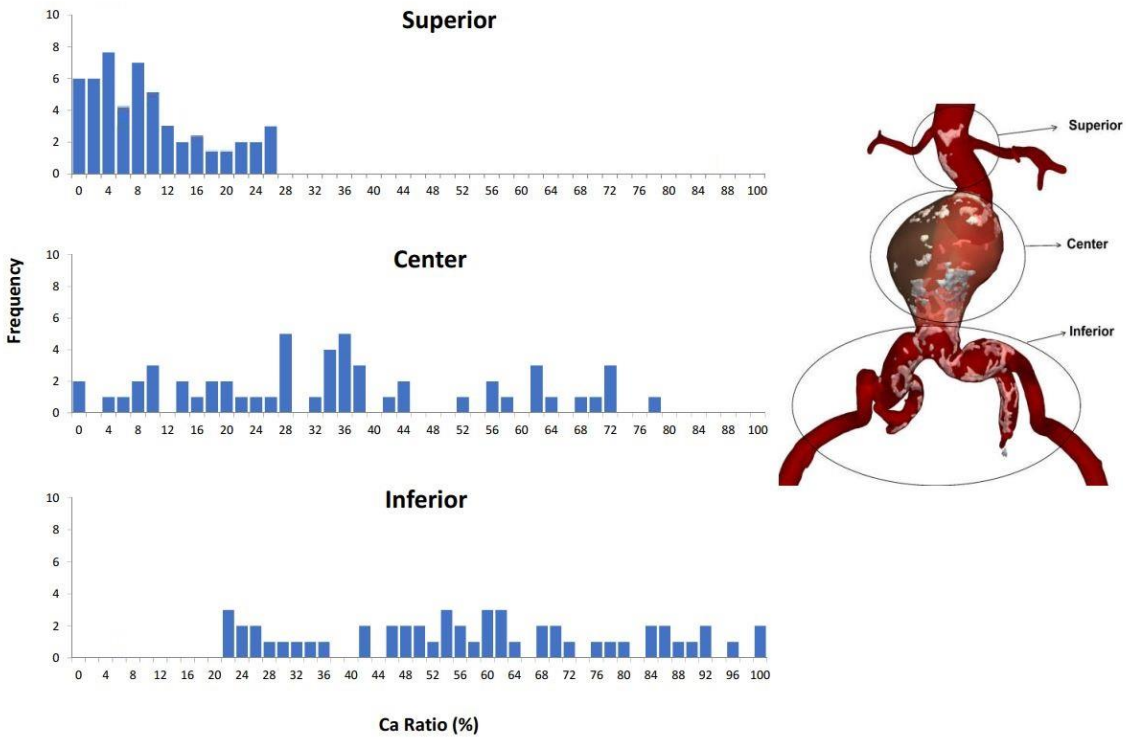

Figure 3.8: Distribution of Ca ratios at the superior, center and inferior locations of AAA.

The distributions of corresponding Ca ratios for all EVAR patients are illustrated in Figure 3.8. At the superior location, the distribution of Ca ratio appears bimodal: normally distributed below 10% and somehow uniform afterwards. Hence, EVAR patients are divided into two groups

accordingly to verify if Ca ratio at the superior location associated with any surgical complexity and complications.

Results in Table 3.5 indicates that a higher ratio of Ca at this location can significantly prolong the surgical duration (p=0.02) and fluoroscopy time (p=0.02), implying that EVAR procedures become more challenging when Ca accumulated proportionally more around the renal artery ostia. Nevertheless, effects on EVAR complications in this case remains insignificant. This could be related to the small sample size in our study, where the number of complication cases in each group might be too small to reveal a significant difference that can be seen with a larger samples size.

Superior Location	Ca Ratio > 10% (n=18)	Ca Ratio < 10% (n=35)	P value
Surgical Complications			
Surgical duration [min]	**195 ± 83.3**	**145 ± 61.1**	**0.02**
Fluoroscopy time [min]	**37 ± 26.9**	**24 ± 12.2**	**0.02**
Total iodine [ml]	157 ± 61.4	127 ± 58.9	0.11
Type 1a	31%	11%	0.11
Type 1b	6%	5%	> 0.5
Type 2	31%	27%	> 0.5
Limb Thrombosis	19%	5%	0.16
Comorbidities			
AAA Diameter [cm]	**6.5 ± 0.94**	**6.0 ± 0.89**	**0.04**

Table 3.5: Comparison of EVAR complexity and complications between different ranges of Ca ratio at the superior location of AAA. (n: sample size for that patient group; min: minutes)

One interesting discovery, the AAA diameter is significantly larger (p=0.04) in the case of higher Ca ratio around the renal artery ostia. Given the rigid nature of Ca, higher Ca ratio at this region may create a significant mismatch of wall compliance along the aorta, resulting in a sudden flow expansion at the transition from the superior to center region. Therefore, a possible transition to turbulence flow with more pronounced hemodynamic effects (237), such as strong recirculation and elevated wall shear stress, is speculated. As mentioned in the previous chapter, these biomechanical factors may subsequently induce more advance atherosclerotic degeneration in the

medial layer, favoring the progressive aneurysmal development. Further investigations with numerical models elucidating such hemodynamic phenomenon are required to support this hypothesis.

For both center and inferior locations, the distributions of Ca ratio are relatively wider and more uniform; hence, patients are divided in two groups according to the mean of Ca ratios for similar analysis. However, no indicative result regarding their effects on surgical complexity and complications has been discovered.

In general, the Ca ratios appears to increase gradually from superior toward inferior regions of AAA, supporting our previous observation that the aortic Ca is becoming more pronounced from the AAA neck down towards the iliac arteries.

3.3.5.4 Triple Factors

To further investigate the effects of Ca morphological characteristics combining the volume, location and shape on EVAR complications, analysis with specific sets of criteria simultaneously representing different risk factors must be considered.

- Ca volume: severe Ca is assumed to generally increase the risk of treatment complications.
- Ca location: intense Ca located around the AAA neck may cause Type IA endoleaks. If more than half of Ca accumulates below the bifurcation (inferior location), it may induce Type IB or limb thrombosis. In contrast, if more than half of Ca accumulates above the bifurcation (center & superior locations), it may affect sac shrinkage after EVAR and lead to Type II endoleaks.
- Ca shape: the presence of large Ca flakes or strips may compromise the conformability of SG, as well as vessel remodeling after EVAR. More specifically, the shape of Ca at the proximal neck may result in different level of wall compliance mismatch at the SG anchoring site, which is essential for the quality of proximal seal. On the other hands, AAAs with complete circular Ca has been associated with failure in sac shrinkage (56), again may potentially cause Type II endoleaks.

Accordingly, a new series of patient classification process considering multiple Ca morphological risk factors, as illustrated in the flowchart below (Fig. 3.9), is utilized to evaluate the potential contribution to a presumed EVAR complication.

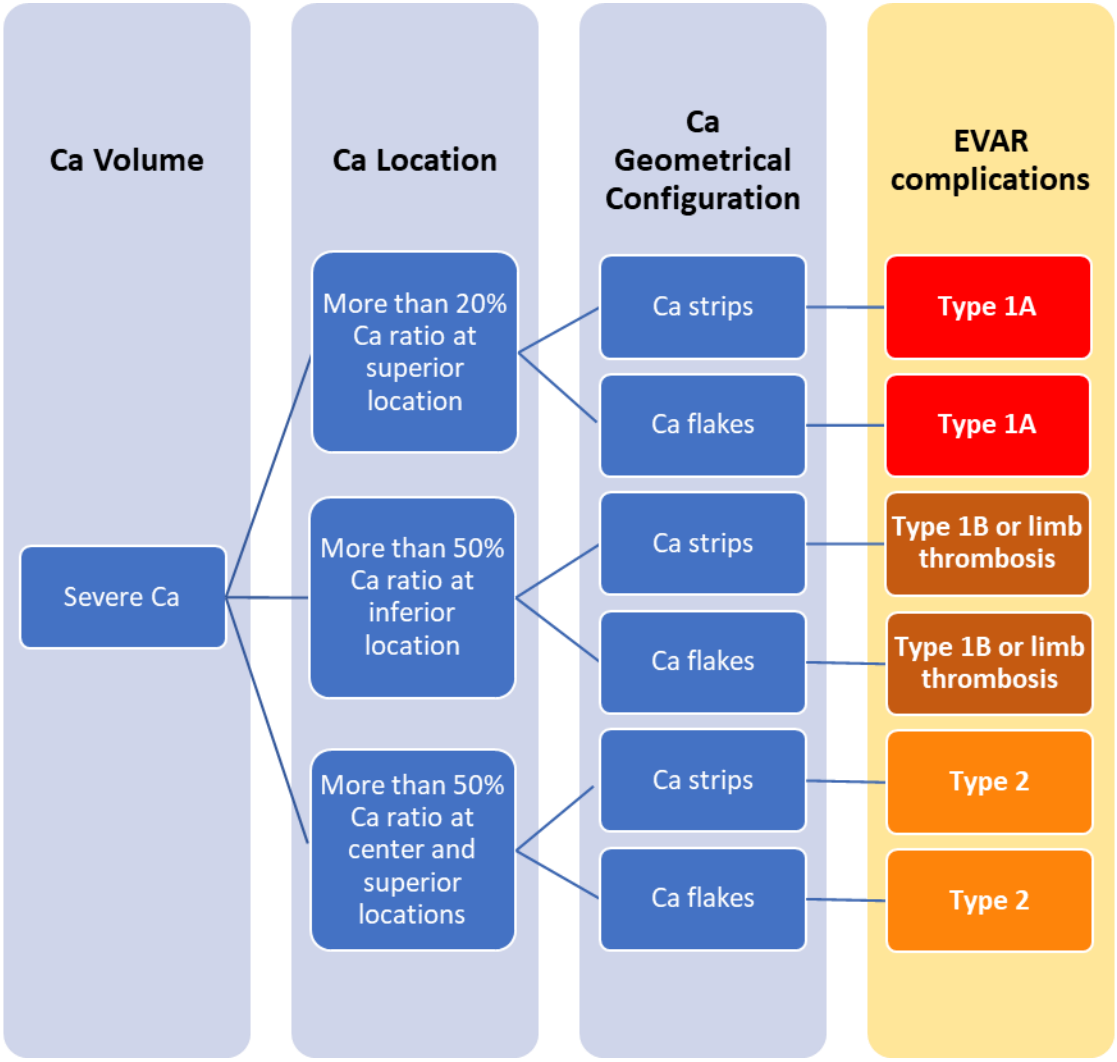

Figure 3.9: Flow diagram explaining the stratification approach, according to relevant clinical implications, to evaluate the combined effects of Ca volumes, locations and shapes on specific EVAR complications.

Significant findings from this analysis are summarized in Table 3.6, where the risks of EVAR complications are highlighted for three scenarios.

- First, if the AAA is severely calcified, with more than 20% of Ca accumulated around the renal artery ostia and the presence of Ca in strip, it bears a very high risk for Type1A endoleaks (100% peri-operative Type 1A, p=0.003).

- Second, if the AAA is severely calcified, with more than 50% of Ca accumulated from the bifurcation to iliac arteries, it can easily cause limb thrombosis (60%, p=0.004) regardless of the presence of Ca strips or flakes. However, no significant correlation is found for Type IB in this study.
- Third, if the AAA is severely calcified, with more than 50% of Ca accumulated above the bifurcation and the presence of Ca strip around the aneurysm, Type2 endoleaks may very likely occur (50% post-operative Type 2, p=0.038).

	Type1A	P-value
Ca Volume > 3 cm^3 **Ca in Superior Region > 20%** **Ca strip in Superior Region**	100% (3/3)	0.003
All Other Patients	12% (6/50)	

	Limb Thrombosis	P-value
Ca Volume > 3 cm^3 **Ca in Inferior Region > 50%**	60% (3/5)	0.004
All Other Patients	4% (2/48)	

	Type2	P-value
Ca Volume > 3 cm^3 **Ca in Inferior Region < 50%** **Ca Strip in Center Region**	50% (3/6)	0.038
All Other Patients	25% (12/47)	

Table 3.6: Chance of EVAR complications when the EVAR patients' Ca morphological characteristics meet certain combinations of criteria.

Consequently, results from all above statistical analysis provide strong evidences to confirm the first hypothesis of this thesis: the morphological characteristics of Ca (volume, location and shape) combine together to alter the global behavior of aortic wall and thus, play an important role in EVAR assessment.

3.3.6 Finite Element Analysis

In order to better understand how the variation in Ca volume with different geometrical configurations may affect the behavior of the AAA wall under the same pressure loading, simplified finite-element models representing those scenarios have been developed and simulated.

3.3.6.1 Numerical Model

Ca loads	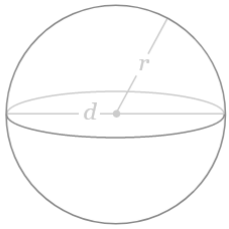 $V = \frac{4}{3}\pi r^3$ **Stone – Sphere**	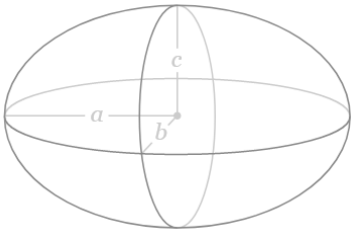 $V = \frac{4}{3}\pi a b c$ **Strip – Ellipsoid**	**Flake – Disk** 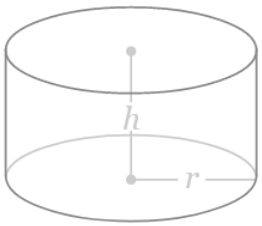 $V = \pi r^2 h$ *Fillet radius 0.1mm to make round edges*
3%	r = 0.612 mm	a = 1.273 mm b = c = 0.424 mm	r = 0.771 mm h = 0.514 mm
6%	r = 0.771 mm	a = 1.604 mm b = c = 0.535 mm	r = 0.972 mm h = 0.648 mm
10%	r = 0.914 mm	a = 1.902 mm b = c = 0.634 mm	r = 1.152 mm h = 0.768 mm

Table 3.7: Details geometrical specifications for Ca inclusion models (V: volume).

All Ca inclusions were completely embedded in a cubic vessel wall of dimension 2 mm thickness, 4 mm width and height. Four simplified geometrical configurations were considered: spheres for Ca stones, elongated ellipsoids with its length at least 3 times greater than the width for Ca strips (both in vertical and diagonal orientations) and round-edge disks with diameter at least 3 times greater than the thickness for Ca flakes. To represent different Ca loads, three volume ratios were modeled, namely 3%, 6% and 10% referring to the highest cases of mild, medium and heavy Ca. Note that the most severe case was not considered because it may occupy most of the vessel space (especially the case of flake), thereby not sufficiently illustrating the deformation between Ca and the vessel wall under loadings. Detailed calculations on the Ca inclusion dimension are shown in the Table 3.7.

A hyperelastic, homogenous, isotropic and incompressible material model was assigned to the AAA wall, with the second order Yeoh hyperelastic material strain energy function (W) as follows, where I_1 represent the first strain invariant. According to previous studies, the material parameters C_{10} and C_{20} are often assigned as 174 and 1881 kPa respectively (59,159).

$$W = C_{10} \times (I_1 - 3) + C_{20} \times (I_1 - 3)^2$$

(Equation 6)

On the other hand, Ca was characterized with a density of 0.12 g/mm^3, and modelled as a linear elastic material with a Young's Modulus of 50 MPa and a 0.4 Poisson Ratio (238). Ca inclusion and the adjacent wall were attached together, sharing the interface with identical nodes and elements.

To reproduce the amplified circumferential stretch under diseased condition (AAA), uniaxial tensile stretch (vertical direction in Figure 3.10) was applied, with up till 25% strain in 1000 steps to investigate the rupture risk. Numerical simulations were performed using the LS-DYNA explicit finite-element solver (Livermore Software Technology Corporation, Livermore, CA, USA). For each case, stresses were calculated at different time points, then averaged over multiple locations inside the vessel wall close to the Ca inclusion (anterior, posterior, top, bottom, lateral to Ca).

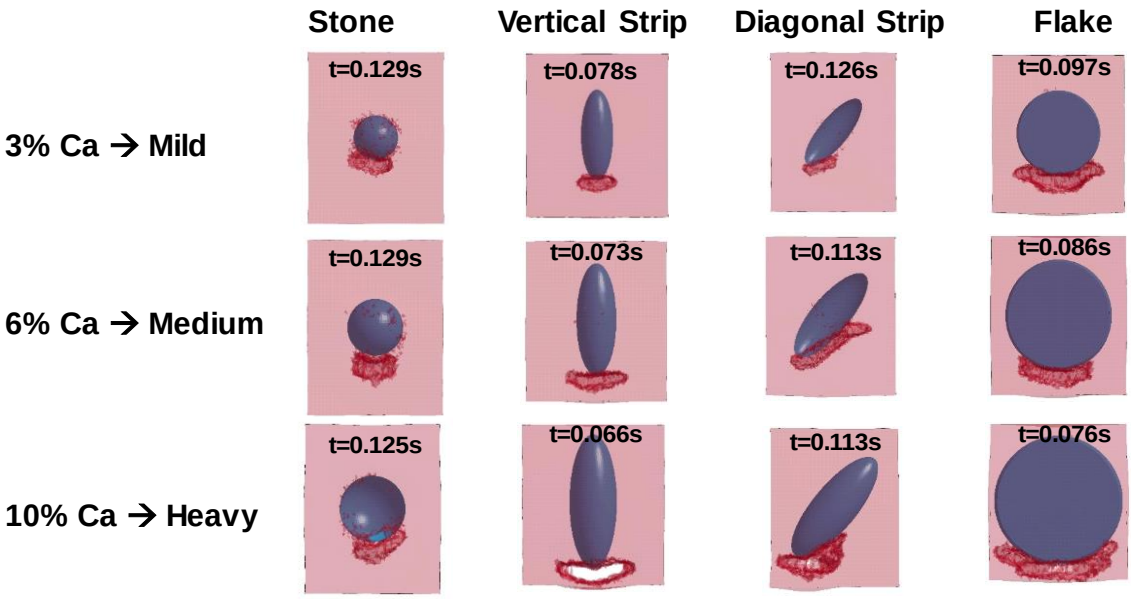

Figure 3.10: Simplified finite element models of AAA wall with Ca inclusions, representing mild, medium and heavy Ca cases, to evaluate the biomechanical effect of Ca shapes and orientations on the aortic wall (t: time point where we start seeing vessel rupture; s: seconds).

Figure 3.10 compares the deformed configurations of those simulated walls, with Ca inclusions in different shapes and volumes, at the time point where we start seeing vessel rupture.

3.3.6.2 Simulated Results

Results in Figure 3.10 show that wall failures always initiate at the edge of Ca and most likely propagate along its boundary, which agrees with the experimental observation reported by Robertson A. M. in 2017 (239). While Ca strip is the least common shape except for the severe Ca cases, any sub-failures at its edge may propagate very easily along its longitudinal direction and cause catastrophic damage, as indicated in the case of diagonal Ca strip. Although the wall failure with vertical Ca strip doesn't propagate along its boundary, the voids develop relatively fast and indeed, resulting in a higher risk of rupture compared to the diagonal strip.

While looking at the stress-strain behavior of each geometrical configuration (Fig. 3.11), one may notice that high Ca volume associates with a higher risk of wall failure, except for Ca stones which appear relatively less sensitive to Ca volume. While comparing results of different geometrical configurations having the same Ca volume, the risk of wall failure is always the highest with Ca flakes and lowest with Ca stones. In structural stress analysis, any geometric

singularity and sudden variation in material stiffness may both result in stress concentration, where the transition boundary is usually subjected to the highest stress. Although Ca volume and material stiffness are the same, the curvature at the rim of Ca flake is substantially greater and more complex than that at the relatively uniform Ca stone surface, hence leading to the higher risk of rupture. As for Ca strips, in agreement with our previous observation, the ultimate tensile stress of diagonal strips is much greater than that of vertical strips, suggesting a higher risk of wall failure when Ca strips orient along the direction of major stresses. An interesting observation, the vessel with Ca stone in heavy volume has a much higher ultimate strength and fails at a greater strain compare to the vessel with Ca flake or vertical strip in mild volume. So to speak, the risk of vessel rupture for a mild calcified patient with mostly Ca flakes or vertical strips may just be as high as a heavily calcified patient but with lots of Ca stones. According to our Ca morphological analysis, such a scenario is possible: the occurrence of Ca flakes at location 5 is the highest in the mild Ca group, whereas the occurrence of Ca stones at location 2 is also among the highest in the severe Ca group (Fig. 3.5). The inevitable risk of vessel rupture even in mild Ca cases during catheters navigation is therefore underlined. Consequently, it is highly recommended to take into account Ca geometrical configurations for EVAR assessment, as well as AAA rupture risk evaluation, which is still not the case in clinical practice nowadays.

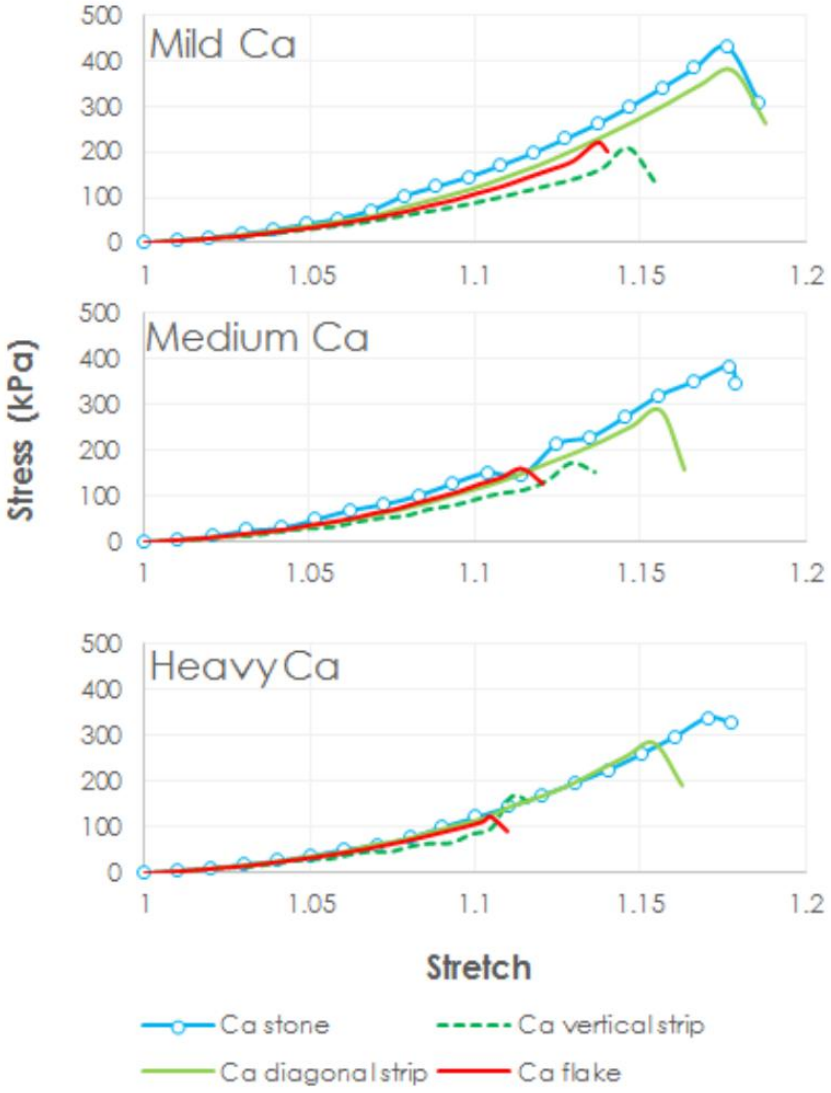

Figure 3.11: Stress-strain behavior of simulated aortic tissue with Ca in different geometrical configurations and in different volume.

3.4 Summary

First, a thorough examination of Ca morphological characteristics, in terms of the extent, geometrical configurations and locations, over a general AAA population is presented. Unlike conventional methods in clinical evaluations, a novel strategy, combining the quantitative analysis using 3D reconstructions from clinical CTs and the qualitative analysis through subsequent classifications of Ca shapes and locations, is applied. The presence of Ca in all AAA patients is confirmed, where severely calcified cases are noteworthy. Ca is most commonly found in the iliac arteries and rarely found lateral to the ILT. As the AAA becomes more calcified, the proportion of Ca stones decreases and that of Ca strips increases, whereas that of Ca flakes remains relatively consistent, suggesting a growth pattern during the evolution of Ca development. Finally, representative models representing the most common and severe scenarios of Ca in AAA are proposed for future studies.

Subsequently, a series of statistical analysis to understand the contribution of these morphological factors to AAA comorbidities, EVAR complexity and complications is also discussed. Among all AAA patients, severely calcified cases are significantly associated with older age populations. Higher complexity in EVAR treatment is demonstrated with severely calcified cases. More specifically, greater Ca ratios around the AAA neck correspond to larger AAA diameters, as well as longer EVAR surgeries. While taking into account multiple factors, namely the volumes, shapes and locations of Ca, one can provide more reliable predictions on certain EVAR complications.

Furthermore, the biomechanical effect of Ca geometrical configurations along the variation of Ca volume is illustrated by simplified finite-element models. It confirms that higher Ca volume generally increases the risk of AAA wall rupture. For the same level of Ca loads, flaks induce the highest rupture risk and stones appear to be the safest, where vertical strips correspond to greater risk than diagonal strips. Nevertheless, the variation in Ca shapes can drastically reverse the rupture risk solely associated with Ca loads, confirming the importance to include geometric configurations as a risk factor in clinical evaluations.

Consequently, this chapter presents the first successful attempt to study the combined effects of Ca morphological characteristics on EVAR complexity and complications. Moreover, it provides not only evidences for future investigations in the pathophysiology or aortic Ca, but also valuable insight to clarify the debatable role of Ca in AAA.

4

PATIENT-INSPIRED ANTHROMORPHIC MOCKUP FOR AAA

In this Chapter, the design and development of a hydrogel-based anthropomorphic mockup (AMM) is presented, allowing further investigations on the biomechanical constraints of AAA during EVAR. Specifically, the hydrogel fabrication process enabling a human-AAA-like biomechanical response is described. The molding sequence and the pressurizing system designed to reproduce the patient-inspired geometrical and diseased characteristics of AAA are also illustrated. A mechanically, anatomically and pathologically realistic AMM for AAA is developed for the first time, with subsequent EVAR experiments highlighting the importance of surrounding tissues while interacting with endovascular devices. Furthermore, potential use of this AMM for medical training is also suggested.

4.1 Motivations

Current complications of EVAR reflect our inadequate knowledge and experience of the biomechanical interaction between the aortic wall and the endovascular devices (i.e., SG and catheters). Not only the anatomical feature of AAA, but also the aortic wall degeneration characteristics (i.e., wall stiffening and development of ILT) may be contributing factors. As it will be complicated and risky to evaluate this biomechanical interaction directly in vivo, vascular mockups become an interesting alternative. Besides, standardized mockups allow the experiment to be reproducible, by-passing the limitations of animal experiments due to cross-species and cross-specimens variabilities. Albeit the above mentioned benefits, current mockups are designed to address a single or few parameters in questions, rendering a comprehensive vascular mockup in demand. Thus, we aimed to develop an anthropomorphic mockup (AMM) of AAA that is mainly composed of PVA-C, which could exhibit the major mechanical, anatomical and pathological characteristics of human AAA and surrounding structures. Such AMM can therefore provide an essential path to reverse engineer the complex biomechanical behavior of AAA, especially during EVAR.

4.2 Methodology

4.2.1 Anthropomorphic Mockup Design & Development

A patient-inspired AAA model generated from a previous work (240) was adopted for the AMM in this study. This model eliminated the geometrical irregularities in patient-specific cases, but still well represented the common anatomical and pathological characteristics of human AAA, namely the iliac artery ostia, the aneurysm sac, the ILT and the bifurcated iliac arteries (Fig. 4.1). By varying the parameters during hydrogel fabrication, we tailored the mechanical elasticity of the PVA-C very similar to that of human AAA wall, ILT (94) and abdominal fat (192). A specific molding-demolding technique with either interconnected or dissolvable molds was applied to reproduce the anatomical and pathogenic features. An air-tight system was designed to maintain the intraluminal and abdominal pressure, and to encase the surrounding tissue such as the abdominal fat and the spine. Detailed methodology on the hydrogel preparation, molds fabrication, reproduction of the anatomy and anthropomorphic system are presented as follows.

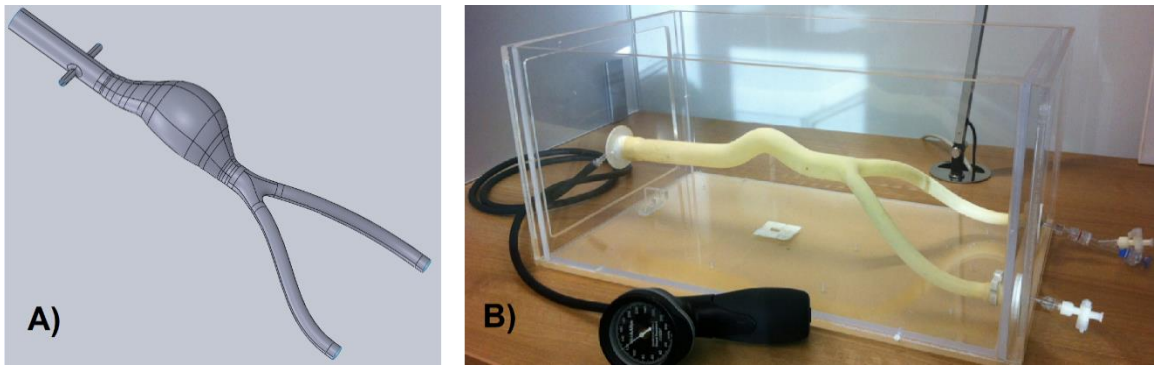

Figure 4.1: A) Patient-inspired AAA geometry modified from our previous work, with the addition of renal artery ostia and an eccentric ILT; B) 3D printed simplified patient-inspired model presented in our previous work.

Hydrogel Preparation

A commercial grade, fully hydrolyzed and soluble polyvinyl alcohol powder (P1763 Sigma-Aldrich) was used. The weight concentration of PVA-C solution was 10%, which allowed a relatively low viscosity to facilitate bubbles release during molding steps. To develop PVA-C hydrogel mockup, first, the PVA powder must be completely dissolved in water at 100℃, then cooled down to room temperature and injected into the molds for specific cryogenic treatment in a temperature-controlled freezer (Fig. 4.2).

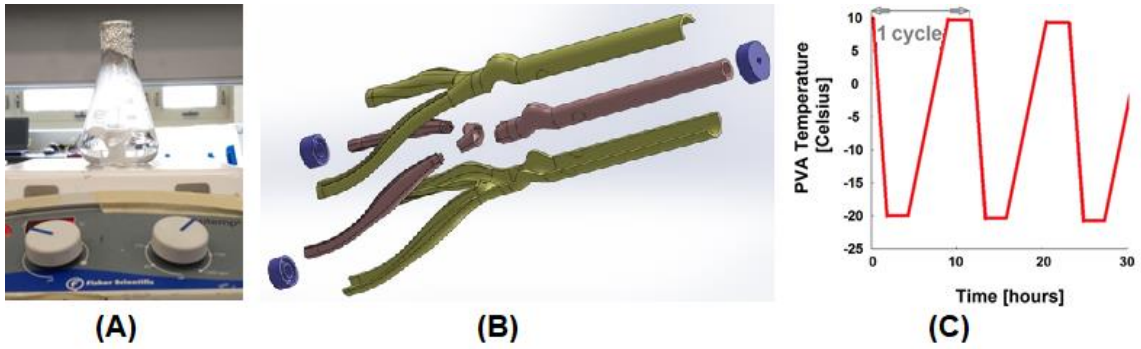

Figure 4.2: PVA-C fabrication process: A) dissolve PVA powder into boiling water; B) inject PVA solution into patient-inspired AAA molds; C) demonstration of cryogenic cycles in the temperature-controlled freezer.

Based on our previous experience (219), the cryogenic treatment was designed as follows: each cycle was first frozen at a rate of 0.333℃/min to -20℃ and rested for two hours, then thawed at a rate of 0.08℃/min to 10℃ and rested for another two hours. A thermal couple was inserted at the center of the molds to monitor temperature variations. Numbers of studies have demonstrated that repeated thermal cycling of PVA-C can increase the crystallinity in the hydrogel, thereby

increasing its elastic modulus (209–211,213,214). Therefore, PVA-C specimens made by the same cryogenic treatment in each cycle but with different number of cycles were prepared, to determine the optimal number of cycles for different components of the AMM (stiffen aortic wall, ILT and abdominal fat).

Mold Fabrication

Traditionally, molds for PVA-C mockup were made in metal to provide optimal heat-transfer results. However, due to the complexity in our model geometry, especially the tubular bifurcating shape, rapid prototyping technology was ideal for mold fabrication. As such, all our molds were 3D printed in acrylonitrile butadiene styrene (ABS) using Dimension Elite (P430, Stratasys), with the highest printing resolution and density to maximize the accuracy in printed geometry. In order to obtain efficient temperature control through ABS molds, which was critical for the quality of cryogenic cycles, all molds were designed in a uniform thickness of 2 mm to facilitate heat transfer.

During PVA-C fabrication, molds with rough surface finish could be an issue with the current 3D printing technology. A tiny bump on the mold surface may easily trap bubbles in between the molds, resulting in voids inside the thin PVA-C wall and thus, higher risk of wall rupture under luminal pressure. Therefore, detailed post-processing such as manual sanding, acetone-treatment and thin varnish coating were necessary, to achieve a much smoother surface without defects or signs of threads from 3D printing (Fig. 4.3). Of note, these treatments must be carefully

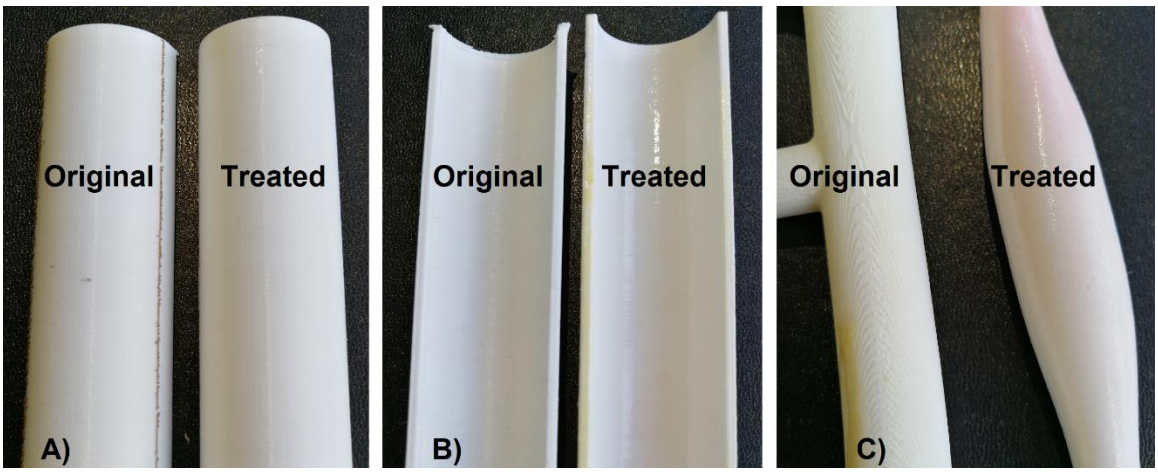

Figure 4.3: Comparison between the surfaces of original and smoothened/treated 3D printed molds: A) outside the outer molds; B) inside the outer molds; C) outside the inner molds.

implemented without affecting much of the original mold thickness (ensure final mold thickness to be 2 ± 0.1 mm).

Realistic Anatomy

In order to create a tubular and bifurcating vessel in one piece, many mold design concepts have been considered. The final mold design consisted of a detachable inner mold, the outer molds that can split in two halves, and three caps at all ends to properly seal and align the inner and outer molds, as shown in Figure 4.4.

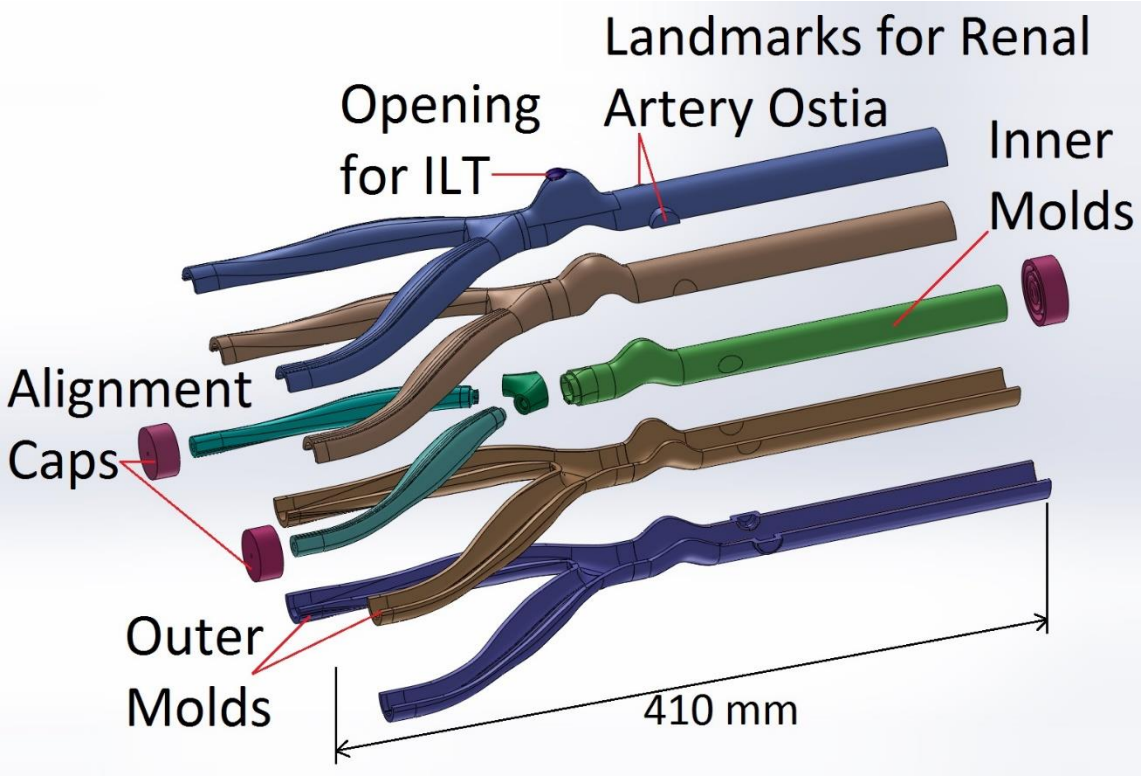

Figure 4.4: Design of multi-layer molds to reproduce a patient-inspired AAA with eccentric ILT, as well as landmarks indicating renal arteries.

As renal artery ostia are the important landmarks during EVAR, but no other essential role in this study, two glass beads (visible under X-ray CT scans) were embedded into the PVA-C wall at those locations (during hydrogel curing process) for indication purpose.

For human AAA, Raghavan et al. have reported the wall thickness varied from 0.23 mm to 4.26 mm (241). A uniform thickness of 2 mm along the AAA, as the mean of those values, has

been commonly adopted in AAA computational models (242–245) and thus, also considered in this study. As such, the space between the inner and outer molds was designed to remain at 2 mm.

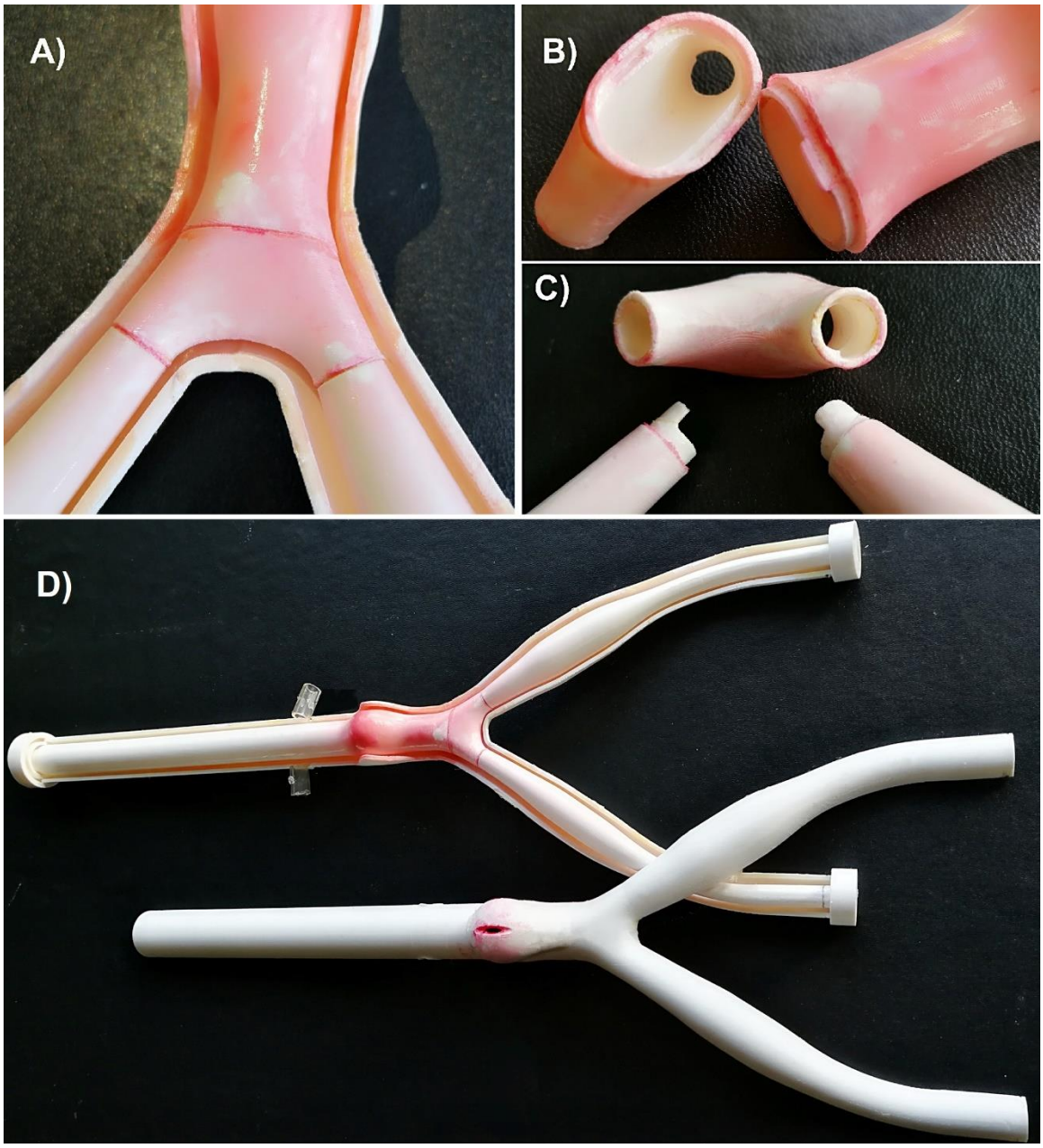

Figure 4.5: The actual 3D printed molds for the patient-inspired AAA mockup: A) interconnected inner molds, with the posterior part of the outer mold placing underneath; B) inner-mold connecting mechanism between the aortic and bifurcation segments; C) inner-mold connecting mechanism between the bifurcation and iliac arteries segments; D) a set of inner and outer molds, note that the molds for renal arteries were transparent and removable in order to facilitate the process of curing glass bead within the PVA-C.

The design of inner molds were crucial to reproduce the tubular bifurcating shape. After numbers of trials, the final design consisted of multiple parts with inter-locking mechanisms. Specifically, three long segments for the aorta and iliac arteries are connected via a small components at the bifurcation. All attachment sites between these parts were thoughtfully designed in male and female flanges with different patterns to ensure proper alignment, as shown in Figure 4.5. Note that all inner molds were also 3D printed in 2 mm thick hollowed pieces, allowing air to circulate inside for efficient heat transfer during the cryogenic treatment.

To combine PVA-C parts with different mechanical strength, a multi-layer molding technique along with a specific molding sequence during PVA-C fabrication was applied. Specifically, after few cycles of cryogenic treatment, the second set of outer molds (same dimension but without ILT extrusion) was used, so that PVA-C solution could be injected through a small opening to the site of ILT, then together cured for the remaining cycles to create an ILT attaching to the AAA wall. Note that the ILT in this study was fabricated inside the lumen, unlike the intramural hematoma that develops in between the wall layers and exhibits potentially a very different biomechanical profile.

Anthropomorphic System

In order to reproduce major pathological characteristics of AAA, some surrounding tissues (abdominal fat and spine), as well as the intraluminal and abdominal pressure were included in this AMM (Fig. 4.6).

An air-tight plexiglass container was developed to encase the vessel along with abdominal fat and a radiopaque spine (LSS-10, AMS Labs Inc.), to allow for optimal exposure with various imaging techniques. Note that no metallic components were used in this AMM, to minimize optical interference during imaging (X-ray and ultrasound).The spine was glued and attached firmly at the bottom to eliminate dislocation during EVAR.

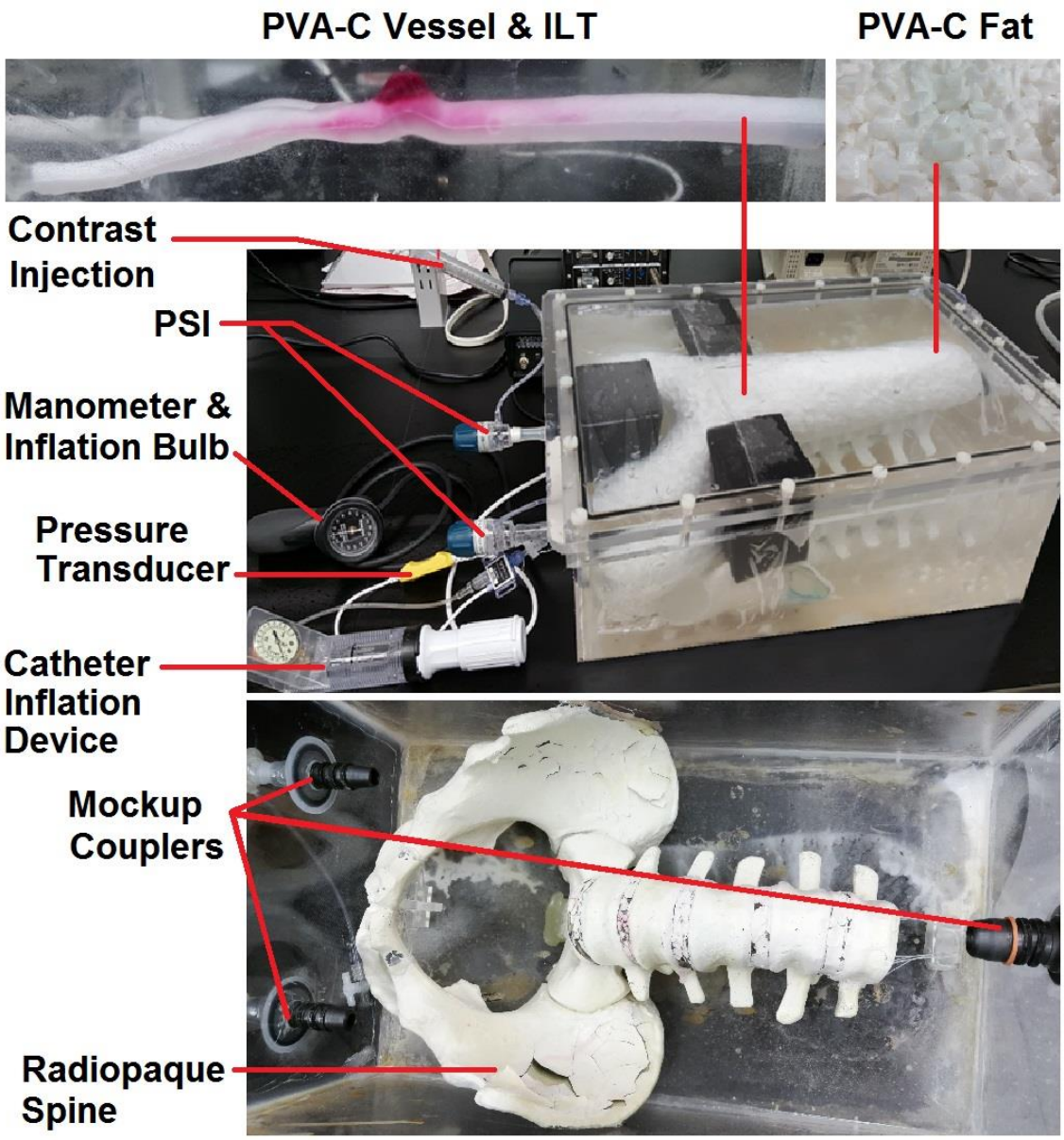

Figure 4.6: Anthropomorphic system to encase PVA-C vessel with ILT (red ink added to visually distinguish ILT from aortic wall), surrounding PVA-C fat, radiopaque spine, and to maintain abdominal and intraluminal pressure. (PSI: percutaneous sheath introducers)

To assemble the PVA-C mockup into the system, both proximal and distal ends of the vessel were carefully slipped over the customized couplers having deep grooves, so that the vessel could then be fastened by cable ties to prevent leakage. At the proximal end, a plastic tube was connected outside the container, with a rubber stopper sealing the pressure inside, mainly to provide more room for delivery device navigation. At the distal end, each coupler was attached to a percutaneous sheath introducers (PSI), ensuring a hemostatic seal during the access of EVAR catheters. A thick

layer (outer diameter 3 to 6 cm) of PVA-C fat cubes was then laid over the whole vessel to mimic the surrounding fat. Of note, it was gently wrapped by a customized cotton-mesh envelop without compressing the vessel, to allow for a decent expansibility of this perivascular fat during EVAR. Finally, the AAA mockup with fat was partly lying on the spine, with at least 5cm away from the top cover to avoid any movement restriction.

In order to mimic an in-vivo environment during EVAR experiments, the port from one PSI was used to inject contrast agent, whereas that from the other PSI was connected to a balloon catheter inflation device via a pressure transducer (Vivitro Labs Inc.), to monitor the intraluminal pressure at 100 mmHg (ViviTest 4.0). Finally, the abdominal pressure inside this AMM system was maintained manually at 12 mmHg (246), by a dial manometer along with inflation bulb.

4.2.2 Mechanical Properties

Tensile Tests

PVA specimens with two to ten thermal cycles were tested and compared with soft tissue values from literatures. Uniaxial tensile tests were carried out using a mechanical tester (Bose, Enduratec ELF 3200). All samples were cut into rectangular strips of 40 mm by 10 mm with a uniform thickness of 2 mm (to mimic averaged AAA wall). Immediately upon fabrication, all samples were stored in water at 5℃, and then equilibrated to room temperature (~24℃) an hour prior to mechanical testing. Two clamps with saw-tooth surface were employed to provide firm gripping of the samples during stretching. According to our previous study (219), six preconditioning cycles were performed prior to the actual test of a maximum 50% extension at a constant speed of 0.1 mm/s. Three samples were repeated for each set of cryogenic treatment.

The applied force $\boldsymbol{F}$ and displacement $\boldsymbol{\Delta l}$ were recorded and the stress-strain curve obtained by calculating the Cauchy stress $\boldsymbol{\sigma}$ and engineering strain ε as follows ($\boldsymbol{A}$: current cross-section area; $\boldsymbol{L}$: initial length).

$$\sigma = \frac{F}{A}, \qquad \varepsilon = \frac{\Delta l}{L}$$

(Equation 7, 8)

Assuming incompressibility, the sample volume v at any given strain should be conserved. Hence, ***A*** and the stress at any given strain $\boldsymbol{\sigma}$ was adjusted as follows ($\boldsymbol{A_0}$: initial cross-section area).

$$A = \frac{v}{L + \Delta l} = \frac{A_0 \times L}{L + \Delta l} = \frac{A_0}{1 + \varepsilon}$$

$$\sigma = \frac{F}{A_0} \times (1 + \varepsilon)$$

(Equation 9, 10)

Since some of our measurements involved larger strain values, the engineering strain $\boldsymbol{\varepsilon}$ mentioned above may not reflect the large strain behavior. Hence, Green strain tensor was used, where the only non-zero component ***Exx*** for uniaxial tension was calculated as follows (assuming tension along x-direction).

$$E_{xx} = \frac{\partial u}{\partial x} + \frac{1}{2}\left(\frac{\partial u}{\partial x}\right)^2 = \frac{\Delta l}{L} + \frac{1}{2}\left(\frac{\Delta l}{L}\right)^2 = \varepsilon + \frac{\varepsilon^2}{2}$$

(Equation 11)

Friction Tests

The goal was to assess the friction behavior of our AMM interacting with EVAR catheters, especially the polymeric sheath with a hydrophilic coating, and then compare the results with that of human aortic tissue and the tissue-mimicking silicone.

The tests were carried out using a Biomomentum Mach 1 v500csst with the experimental set-up as illustrated in Figure 4.7. The sample chamber was custom-designed and 3D printed to fit the Biomomentum Mach 1 measurement stage: not only as a water reservoir to prevent specimen from dehydration, but also as a sample holder with tiny notches at the bottom to prevent specimen from

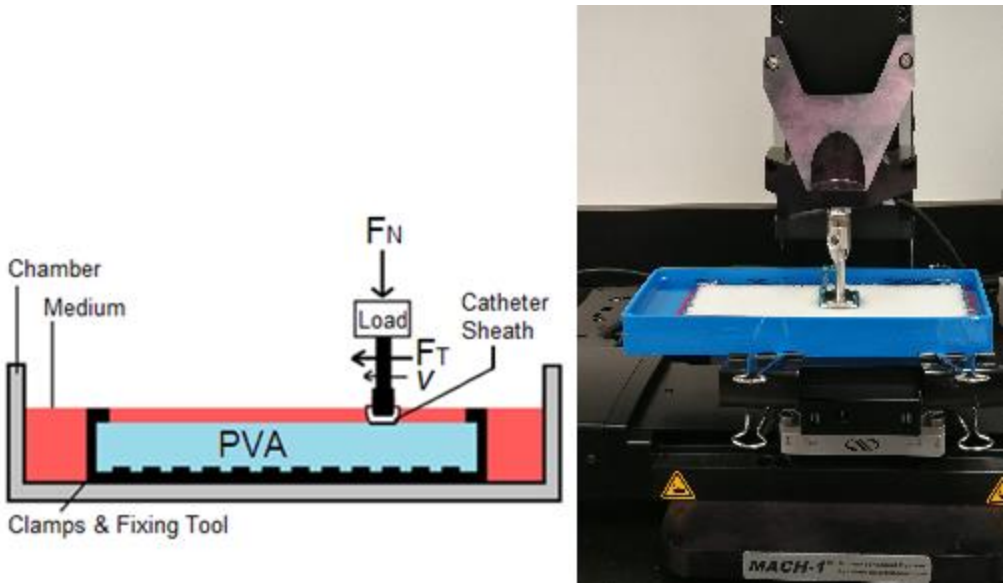

Figure 4.7: Schematic illustration of friction test (left) and actual experimental setup (right). (F_N: normal force; F_T: transverse force; V: velocity)

sliding. A catheter sheath (Cook Medical) was cut and flattened into a rectangular strip, then gently mounted (glue) to the bottom of a shaft (15 mm x 15 mm contact area) connecting to the load cell. With the high-precision multi-axial load cell, friction forces $\boldsymbol{F_T}$ were measured while a range of normal loads $\boldsymbol{F_N}$ were applied: 0.1N (equivalent to force during smooth catheter navigation), 1N, 2N and 3N (equivalent to force during SG deployment) (247). Consequently, the friction coefficient **μ** can be obtained as follows.

$$\mu = \frac{F_T}{F_N}$$

(Equation 12)

Three types of specimens were tested: PVA-C mimicking human AAA wall (number of cryogenic cycles determined after tensile tests), three kinds of silicone commonly used for vascular mockups (Sylgard 184 silicone elastomer from Dow Corning, Mold Max™ 20 & Mold Max™ XLS™ II from Smooth-On Inc.) (248–251), and diseased human AAA tissue (anterior abdominal aortic region, obtained following aortic reconstruction surgeries at Montreal Heart Institute with

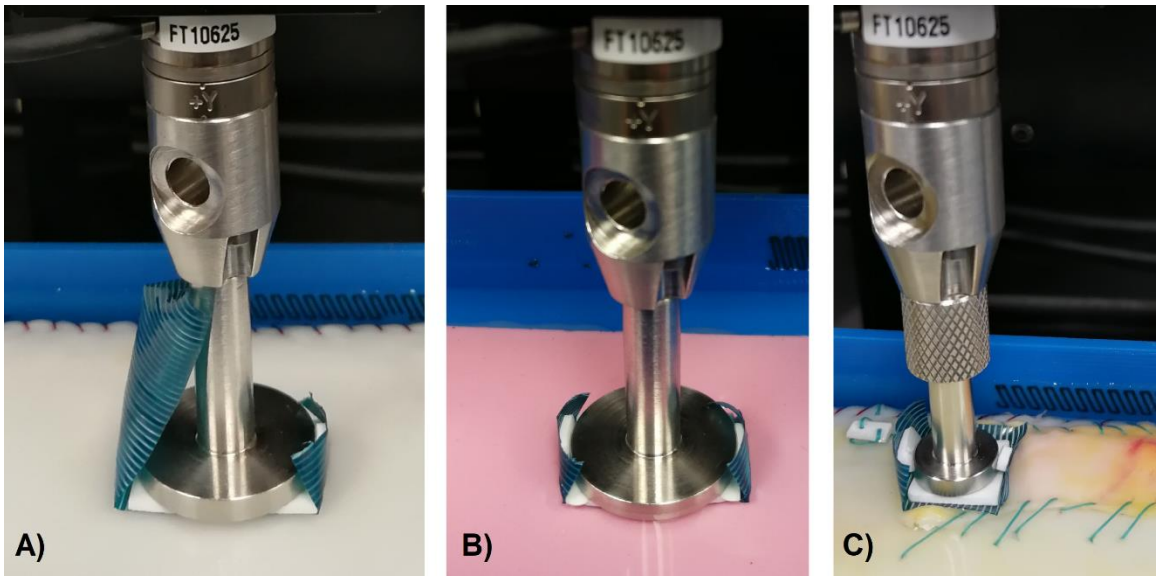

Figure 4.8: Friction tests with different types of specimen: A) PVA-C; B) one type of silicone; C) human AAA tissue sutured on PVA-C, note that although the contact area is smaller due to the size of tissue, friction coefficient should not be affected by the contact area on a macro scale.

ethical approval, refrigerated in phosphate buffered saline and tested within 24 hours), as shown in Figure 4.8. Water was filled up to the contact surface and all experiments were conducted at room temperature (~24℃).

With the aim of obtaining the Stribeck curves (friction coefficient vs. sliding velocity) to better describe the friction behaviour, a set of constant sliding speeds were tested for a sliding distance of 80 mm: from 0.5 mm/s to 50 mm/s, with an increment of 5 mm/s.

4.2.1 EVAR Experiments

EVAR experiments were performed using our AMMs by an interventional specialist in a realistic clinical set-up (Artis-Q, Siemens Healthineers, Forccheim, Germany). One shot and cone beam CT (CBCT) scans were acquired during every stage of EVAR (6 second C-arm spin, 0.47 x 0.47 x 0.47 mm voxels and 24 x 24 x 18.5 cm acquisition volume). 3D models of the lumen and SG were also reconstructed by thresholding technique (lumen < 250 HU; SG > 1000 HU (252)) and snake evolution with ITK-SNAP (version 3.6.0) to verify proper deployments (Fig. 4.9).

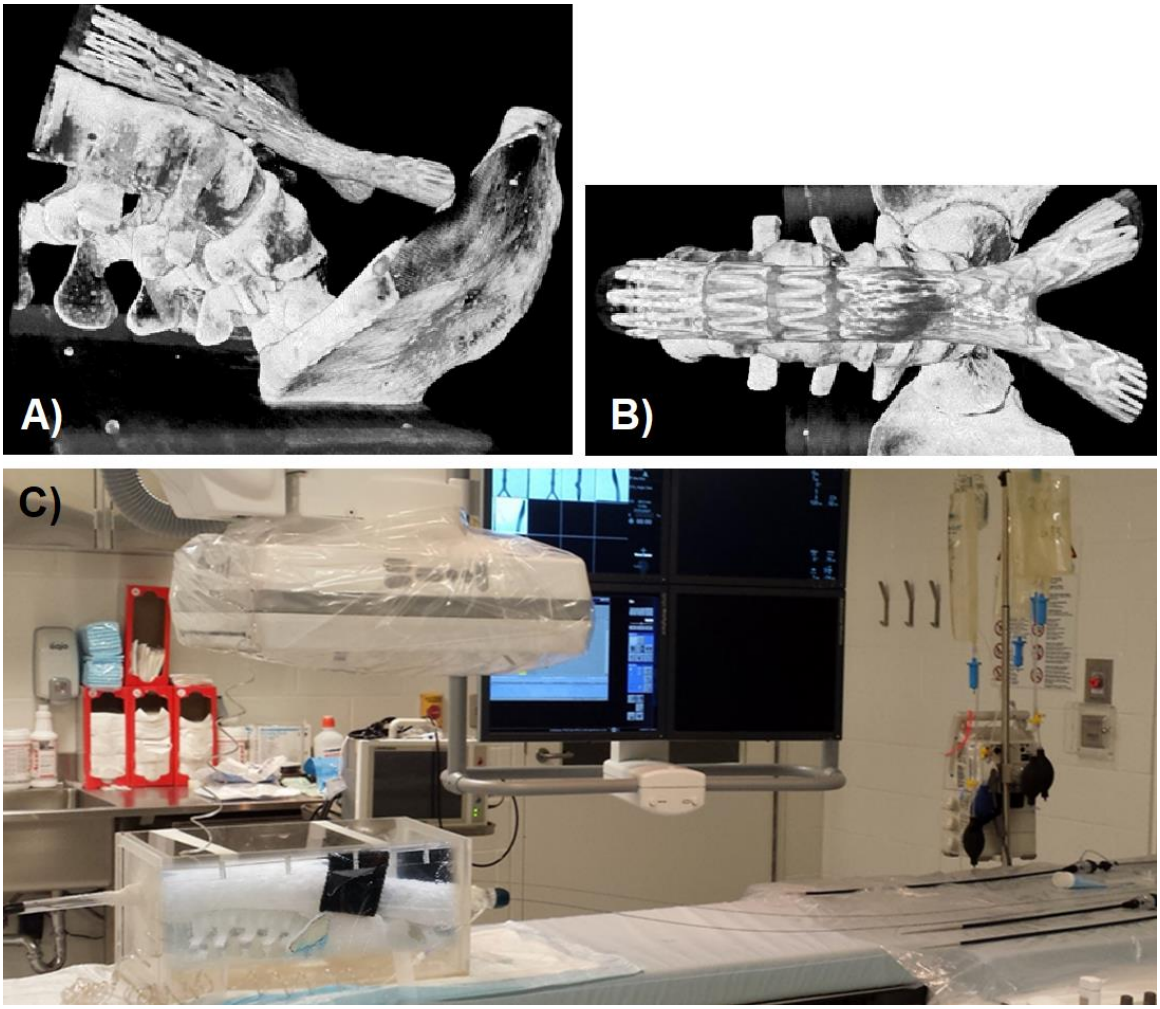

Figure 4.9: Realistic EVAR experiment: reconstructed 3D model illustrating the spine and the deployed SGs form the sagittal plane (A) and the coronal plane (B), and the clinical set-up for EVAR experiments with AMMs are shown in (C).

While keeping the abdominal pressure stable, the vessel expansion along with a gradual increase of luminal pressure (80 mmHg to 160 mmHg) was also recorded by CBCT scans prior to EVAR experiments. For each set of AMM, three zenith SG (main AAA body with bifurcation "TFFB-24-82-ZT", iliac arteries "ZSLE-20-56-ZT" and "ZSLE-24-74-ZT", Cook Medical, Bloomington, IN) were deployed over a Lunderquist Wire (Cook Medical). Note that, for each experiment, new sets of SG were deployed in a new PVA-C mockup in order to prevent any unexpected device damages while retrieving SGs, as well as damages on the aortic wall due to anchoring hooks from SGs. The main AAA body and the right iliac artery were inserted through the right limb of the AMM whereas the left iliac artery was inserted through the left limb of the AMM. One shot acquisitions and fluoroscopy scenes were recorded during different steps of EVAR: the insertion of guide wires, delivery device navigation, and SG deployment. Similarly, CBCT acquisitions were acquired both before and after these procedural steps.

To study the effect of surrounding tissue, two sets of AMMs were considered for the same EVAR treatments: one with surrounding abdominal fat and the other one without it. The centerline of lumen along the aorta at every stage was computed by the Vascular Modeling Toolkit (version 1.4.0). The displacement of centerline was obtained from the Hausdorff distance calculated by MATLAB (version R2018a). Of note, Hausdorff distance can describe how far two lines (subsets of data in a metric space) are separated from each other; more specifically, the greatest value among the distances from each point of one line to the closest point in the other line. In order to confirm our experimental observations with clinical data, three anonymous EVAR patients with AAA characteristics similar to our AMM (almost no Ca, small eccentric thrombus and 0.18~0.39 iliac tortuosity; note that our AMM has 0.22 iliac tortuosity) were selected from our patient database. Similar centerline extractions were repeated for each selected patient, and the centerline displacements at different EVAR stages were compared to relevant values from AMM experiments.

4.3 Results

4.3.1 Biomechanically Realistic

With the results of uniaxial tensile tests, the numbers of cryogenic cycles for specific applications (AAA wall, ILT and abdominal fat) can be determined. Standard deviations for our experimental results are very small and hence not shown in the following plots.

AAA wall

The elastic behavior of PVA-C cured with 6, 8 and 10 cryogenic cycles are compared to that of human AAA wall (157). An excellent agreement between eight-cycle PVA-C and human tissue is observed up till 20% strain (Fig. 4.10), indicating eight cryogenic cycles as the most suitable treatment to mimic AAA wall. Of note, although the elastic modulus of human tissue increases much faster after 25% strain, the stress-strain curve of PVA-C with eight cryogenic cycles displays

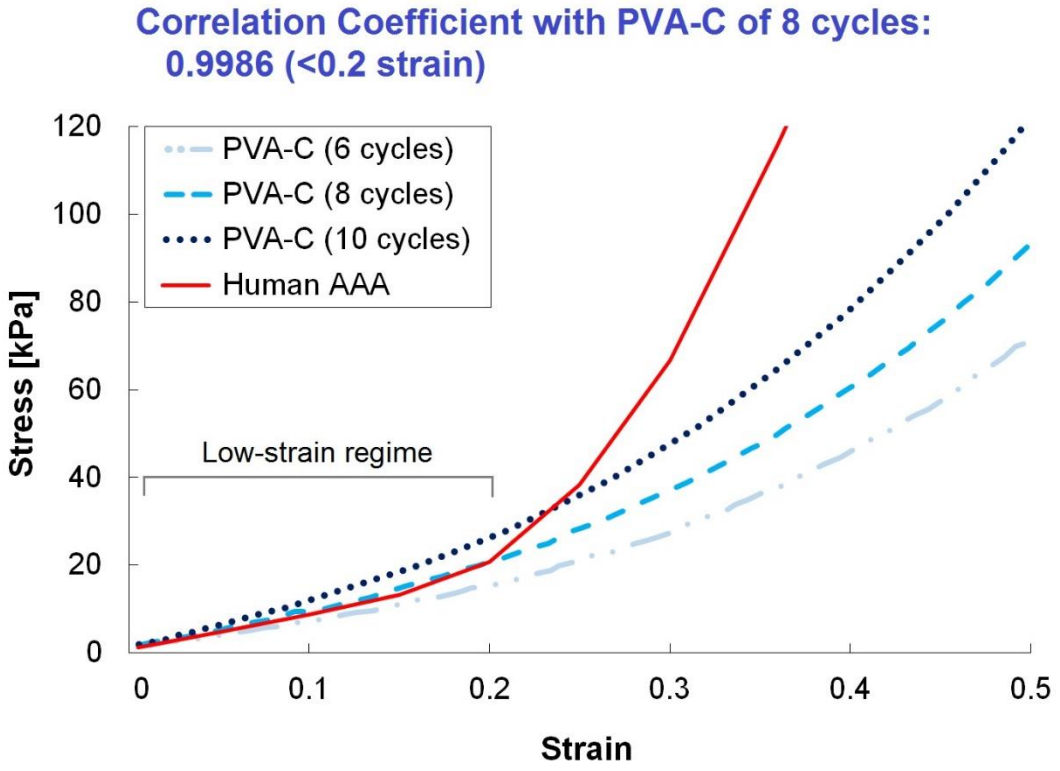

Figure 4.10: Stress-strain behavior of PVA-C gel with 6, 8 and 10 cryogenic cycles compared to that of human AAA tissue from literature.

the best match with that of human AAA tissue under 20% strain. Keeping in mind that the objective in this study is to develop an AMM to investigate the effects of EVAR, and a 10% ~ 20% oversizing is the recommended standard for aortic SG selection (253), which implies a maximum of 15% strain in the AAA wall along circumferential direction. Therefore, PVA-C with eight cycles of cryogenic treatment can sufficiently approximate the mechanical response of human AAA wall in this study.

Intraluminal Thrombus

The stress-strain behavior of our PVA-C with 4 and 5 cryogenic cycles is found to be closest to those of the human ILT reported in the literature (65). Although ILT has been well characterized as an inhomogeneous material consisting of multiple layers with variable stiffness and thickness, reproducing these microscopic details may not result in significantly different AAA responses

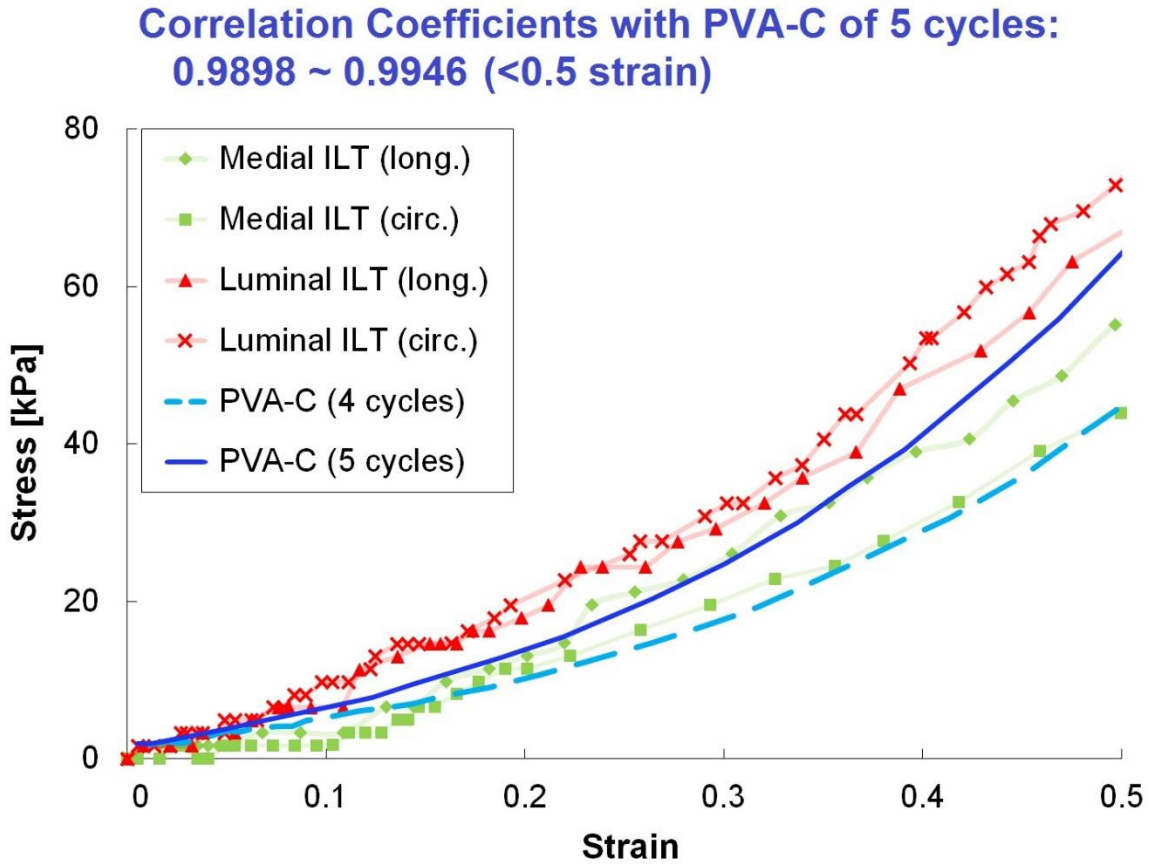

Figure 4.11: Stress-strain behavior of PVA-C gel with 4 and 5 cryogenic cycles compared to that of human ILT (long.: longitudinal direction; circ.: circumferential direction) from literature.

during EVAR. Hence, assuming the ILT to be homogeneous and isotropic, our experimental results suggest that PVA-C with five cryogenic cycles better represents the averaged stress-strain behavior reported from literature (Fig. 4.11) and thus, is selected to mimic the human ILT in our AMM.

Abdominal Fat

Comparing the uniaxial tensile stress of PVA-C under two cryogenic cycles to that of human abdominal fat (192), one can notice that the stress-strain curve of this PVA-C lies between the curves of human fat in both longitudinal and circumferential directions (Fig. 4.12), confirming it to be the optimal selection to approximate human abdominal fat. Similar to the ILT, the abdominal fat is also assumed to be isotropic in our AMM, regardless of its more complex nature, as the abdominal fat is speculated to simply provide a structural support and resistance during EVAR.

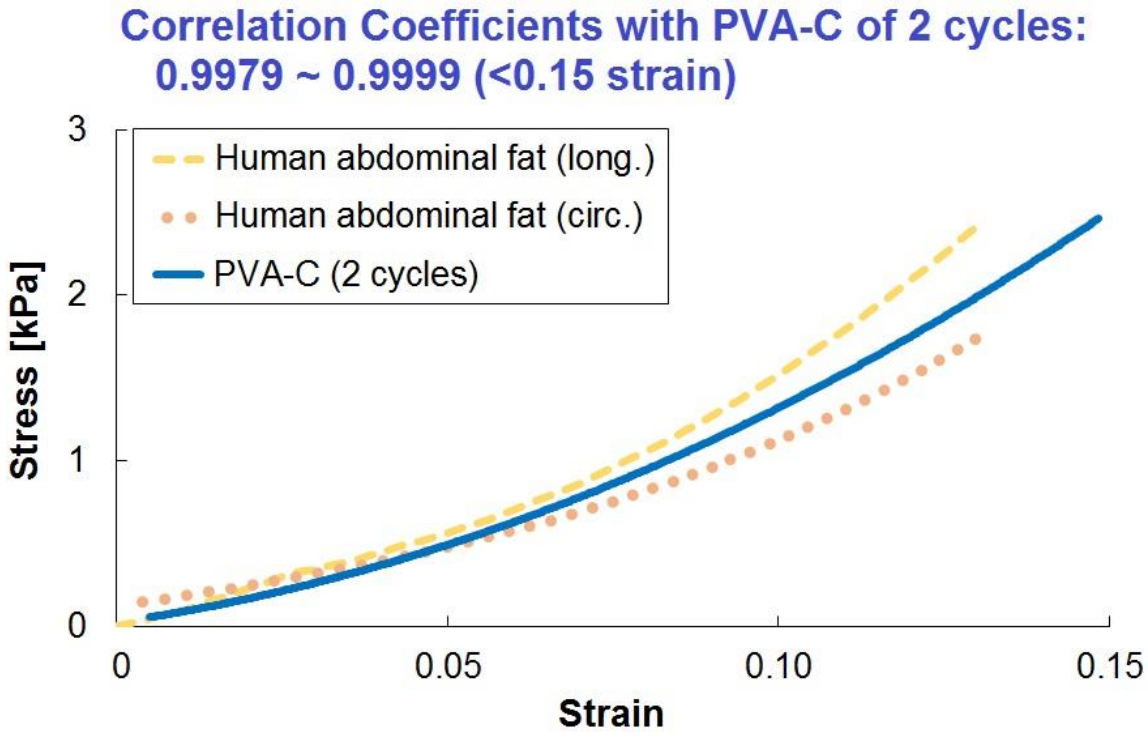

Figure 4.12: Stress-strain behavior of PVA-C gel with 2 cryogenic cycles compared to that of human abdominal fat (long.: longitudinal direction; circ.: circumferential direction) from literature.

Surface Friction

The friction behavior between the catheter sheath and our PVA-C, silicone or human aortic tissue are generally comparable with values reported in literature (254,255). In the situation of smooth catheter navigation (equivalent to a normal load of 0.1 N), as shown in the left plot of Figure 4.13, our results clearly indicate that friction coefficients of PVA-C at various sliding velocities match the values of human AAA wall much more closely than those of tissue-mimicking silicone (values averaged over three types of silicone). Hence, PVA-C is confirmed to be an ideal candidate for mockups to investigate the biomechanical interaction between human vessel and endovascular devices.

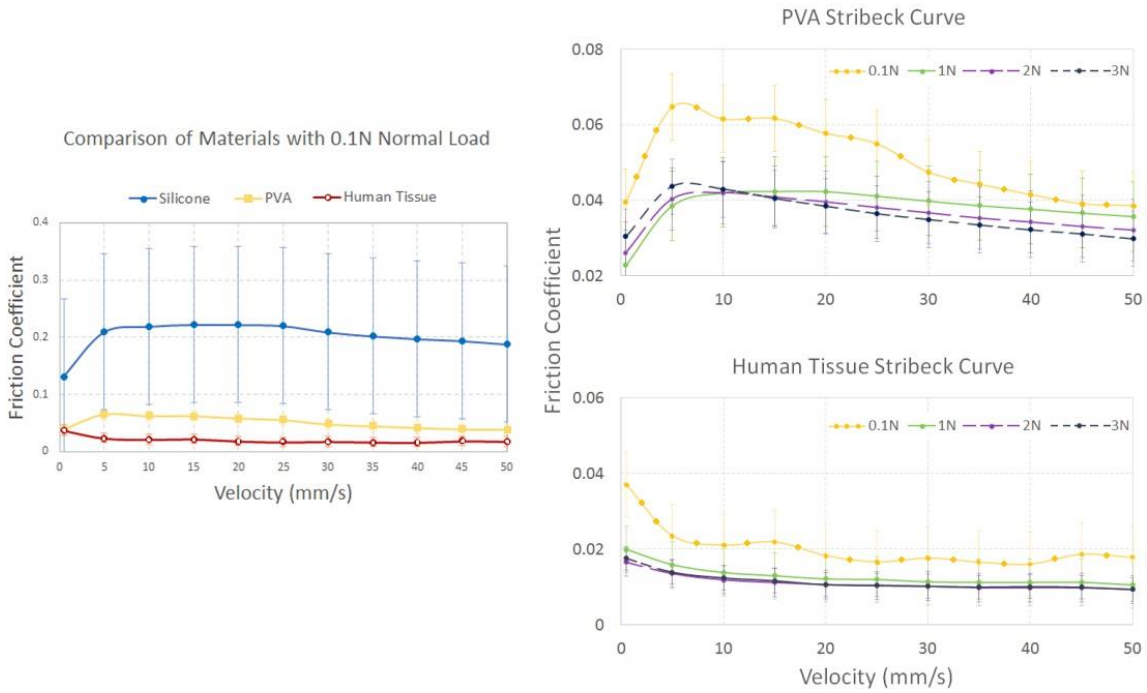

Figure 4.13: Comparison of friction coefficients between different materials under 0.1N normal load (left); comparison of Stribeck curves of PVA-C and human aortic tissue (right) under various loads (0.1N to 3N).

In addition, the Stribeck curves (Fig. 4.13 right plots) describing the relationships between sliding velocities and friction coefficients indicate that the friction coefficient generally decreases as velocity increases, except for PVA-C and silicon with the sliding speed less than 5 mm/s. In fact, the maximum peak of friction coefficient at a certain velocity, observed in the case of PVA-C and silicone, reveals that all tests in this study remain in the region of elastic friction. Unlike the hydrodynamic lubrication friction which normally occurs at a much higher range of sliding

velocities, surface characteristics are the main determinant factors for elastic friction behavior, indirectly confirming PVA-C provides the surface characteristics comparable to human AAA wall.

Of note, friction measurements with all three types of silicone under normal load greater than 0.1N were not completed because the friction force exceeded the range of load cell. Besides, since 0.1N is a relatively small weight, sliding motions can be significantly influenced by the surface flatness, where higher force is required to overcome a tiny bump along the sliding path, potentially resulting in the upward shifts in Stribeck curves. Interestingly, such a shift is more pronounced in the case of PVA-C with lower velocities, implying its slightly more uneven surface finish in comparison with the human tissue measured in this study.

4.3.2 Anthropomorphic System

Anatomically & Pathologically Realistic

The PVA-C vessel with bifurcating iliac arteries has been fabricated using detachable molds with the inter-locking system. As a result of the thin molds with smooth surface, the thickness of final AMM aortic wall, after eight cryogenic cycles, remained unchanged (1.98 ± 0.02 mm).

Meanwhile, the relatively softer ILT has also been created through fewer cycles of cryogenic treatment and cross-linked firmly onto the vessel wall through the multi-layer molding technique. Of note, extra caution must be taken when changing molds during the multi-layer molding sequence, where PVA-C under few cryogenic cycles are relatively fragile; a small defect induced during this process may result in regional biomechanical weakness in the final PVA-C mockup.

AAA mockup with PVA-C abdominal fat has been assembled accordingly into this anthropomorphic system. Water has been injected into the AAA mockup as well as the surrounding space, to reproduce distinct static luminal and abdominal pressures; no leak through the vessel wall has been observed. In addition, no pressure change has been recorded in the vessel, as well as the surrounding space, confirming the complete assembly of the AMM.

In conclusion, an AMM representing the major anatomical (aneurismal and bifurcating vessel with surrounding tissues) and pathological (ILT, intraluminal and abdominal pressures)

characteristics of AAA has been successfully developed using our proposed method, as illustrated in Figure 4.6.

System Fabrication Time, Storage & Cost

With the described methodology, it will only take a week to fabricate each hydrogel mockup, and a few weeks to develop the reusable patient-inspired molds and the anthropomorphic system. However, this time estimation also greatly depends on the skills and experiences of the mockup developer.

Based on our laboratory experience, if all PVA-C components are stored in cool and clean water without fungi contamination (anti-algae aquarium product may be used) and direct sun light, the structural integrity as well as mechanical properties can be well preserved for at least a year, whereas the long-term (>1 year) mechanical properties remain to be accessed.

In terms for material cost, the PVA powder used for the vessel, ILT and surrounding fat all together cost under $100 for each mockup, keeping in mind that PVA-C fat can be used for different vascular mockups. For a set of patient-inspired molds, the material cost is around $200, with an existing 3D printer. The anthropomorphic system is designed and fabricated in-house as well, with features allowing the compatibility with a wide range of AAA mockups (variations in mockup material, dimensions, geometries, intraluminal and abdominal pressures). The material cost for this system (excluding pressure transducer and controller) is around $400, in which many components can be reused for different AAA mockups. Nevertheless, engineers and technicians have been involved in the entire AMM research and development process, the associated labor cost must be adjusted independently.

4.3.3 Mockup EVAR Experiments

To mimic a cardiac cycle with the intraluminal pressure varied between 80mmHg (diastolic) and 160 mmHg (systolic), a pressure gradient of 80 mmHg has been applied. As shown in Figure 4.14, vessel expansion is minimal in the case with surrounding fat, resulting in an increase of 1.8% in diameter and 3.4% in area, with a 0.4 overall distensibility (change in area divided by pressure gradient, unit in $10^{-5}Pa^{-1}$). In the contrary, significant vessel expansion can be found in the case

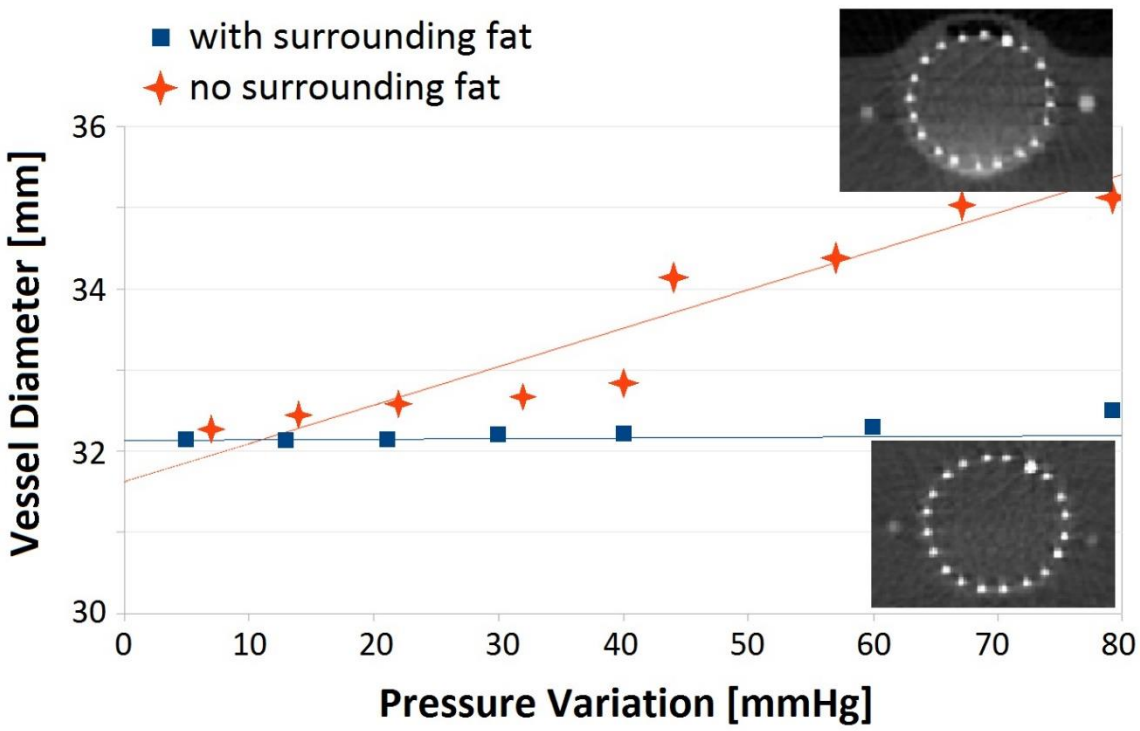

Figure 4.14: PVA-C vessel expansion with intraluminal pressure. Two dots outside the lumen indicate the locations of renal artery ostia.

without surrounding fat, giving rise to an increase of 9.4% in diameter and 21% in area, with a 2.1 overall distensibility.

While performing EVAR using our AMM without surrounding fat, the vessel deformation during SG deployment is more vigorous than what we normally observe clinically. By comparing the aortic centerlines at different navigation and deployment stages to the one at initial stage, we observe the maximum displacement occurred at the deployment stage, indicated by the greatest Hausdorff distance (29.6 mm) between the lumen at those stages, as shown in Figure 4.15. While the surrounding abdominal fat is present, the range of motion during EVAR appeared within the expectation of our medical specialists. Similarly, the maximum centerline displacement is also found at deployment stage with a Hausdorff distance of 6.7 mm, significantly smaller than the case without surrounding fat. While applying the same method to evaluate clinical data (patients with similar AAA characteristics), the maximum centerline displacements for all selected patients are found during SG deployment as well, with the Hausdorff distances being 6.8 mm, 7.2 mm and 12.3 mm. Therefore, the aortic centerline displacements during EVAR in the case of AMM with

surrounding abdominal fat better agree with the range of aortic centerline deviation observed clinically.

To conclude, not only the spine provides an essential structural support for the AAA, but also the surrounding abdominal fat has significant contributions in regulating vessel expansion as well as counteracting with endovascular devices during EVAR.

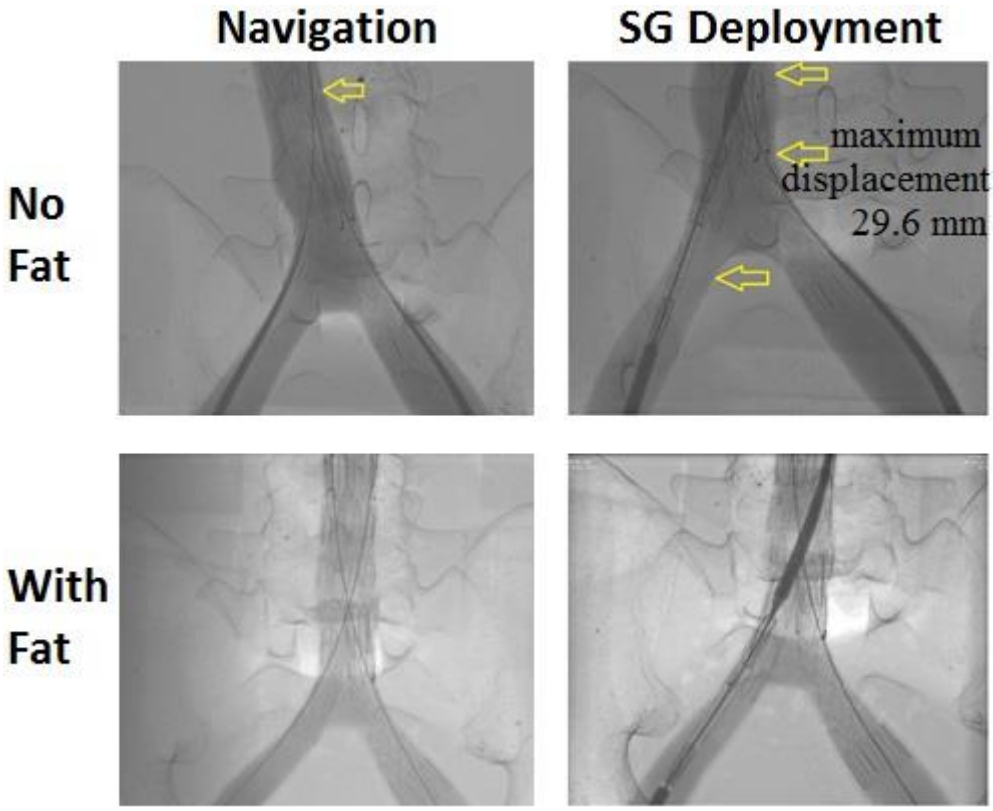

Figure 4.15: CT images illustrating vessel displacement and deformation during EVAR navigation (with guidewires inside) and SG deployment (with guidewires and catheters inside) stages. Top images refer to the case without surrounding fat, bottom images refer to the corresponding moments in the case with surrounding fat.

4.4 Summary

In this chapter, the entire design and development approach of the hydrogel-based AMM consisting of a patient-inspired AAA geometry and several major diseased characteristics is presented.

- First, different PVA-C cryogenic treatments in order to best reproduce the biomechanical behavior (stiffness and friction) of various components in human AAA (aortic wall, ILT and abdominal fat) are identified.

- Subsequently, the design concepts and fabrication process of 3D molds creating the desired mockup geometry, as well as those of the specific sequence to combined PVA-C with different mechanical properties, are fully illustrated.

- Finally, the custom-made anthropomorphic system to encase the AAA mockup and surrounding tissues, providing not only realistic pressurized environment but also convenient access with endovascular devices, is demonstrated in detail. Specific steps to assemble the whole patient-inspired AMM are also discussed thoroughly.

To the best of our knowledge, this study presents the most comprehensive aortic mockup to date, in which the major mechanical, anatomical and pathological characteristics of human AAA, as well as the compatibility with different imaging modalities are all taken into consideration. Hence, such AMM can provide an excellent in-vitro environment for numerical model validations, medical device evaluations, academic demonstrations and medical trainings.

Upon the successful AMM development, EVAR experiments have been performed in a clinical set-up by endovascular specialists. The biomechanical interactions between endovascular devices and the AAA with and without the surrounding abdominal fat is explored extensively, followed by validation with clinical data from patients with similar AAA characteristics. Excessive vessel expansions observed in the case without the abdominal fat raises the concern on determining the zero-pressure geometry for numerical studies. The drastic AAA displacements confirm the essential role of surrounding tissues, both the spine and the abdominal fat, to account for realistic

interactions with endovascular devices. In conclusion, the importance to include surrounding tissues for EVAR assessment using numerical simulation tools is highlighted.

5

PATIENT-SPECIFIC ANTHROMORPHIC MOCKUP FOR AAA

This chapter presents the process of selecting, designing and developing a patient-specific AMM, based on our knowledge and technique gained from the patient-inspired AMM explained in the previous chapter. In particular, large aneurysm, iliac tortuosity and calcifications are the main features added on top of the simplified patient-inspired AMM. Substantial challenges, strategies and limitations to include those features in AMM are discussed thoroughly. Preliminary results demonstrated at the end of this chapter, confirming the feasibility of our proposed method in creating the patient-specific AMM for AAA.

5.1 Motivations

Upon the successful creation of the patient-inspired AMM, extending the current work into a patient-specific model that addresses the following selection criteria would be of great interest.

- First, vessel tortuosity is a common phenomenon in AAA patients. However, the challenge and limitation in simulating the access of endovascular devices in tortuous iliac arteries persist, rendering in-vitro evaluations with vascular mockups ideal for those cases.

- Second, the size of aneurysm and ILT in our patient-inspired AMM are relatively small, further extend those dimension may be beneficial to investigate the case of severe AAA.

- Third, as one of the major characteristics in AAA wall degeneration, Ca may directly affect the interaction with endovascular devices. Of note, Ca is not considered in our patient-inspired AMM due to the huge variability of Ca characteristics in AAA, such as the difference in density, size, geometric configuration, location and distribution pattern (as demonstrated in Chapter 3). Hence, the possibility to include Ca in AMM may provide an in-vitro platform for research with more specific focus, for example the biomechanical effect of certain Ca characteristic on AAA rupture, as well as the interaction with different medical devices.

5.2 Methodology

5.2.1 Patient Selection

A patient-specific model has been selected from our patient data (Fig. 5.1), according to the desired features mentioned above, as well as the symbolic characteristics summarized from the Ca analysis Chapter 3. Specific criteria are listed as follows.

- Significant tortuosity in the iliac arteries

- Decent ILT mass and Ca volumes (greater than medium Ca)

- Ca flakes around the renal artery ostia, bifurcation and iliac arteries

- Good quality in clinical CT scan (slice thickness & voxel spacing below 1 mm)
- Availability of pre- and post-delivery CT scans for clinical validation

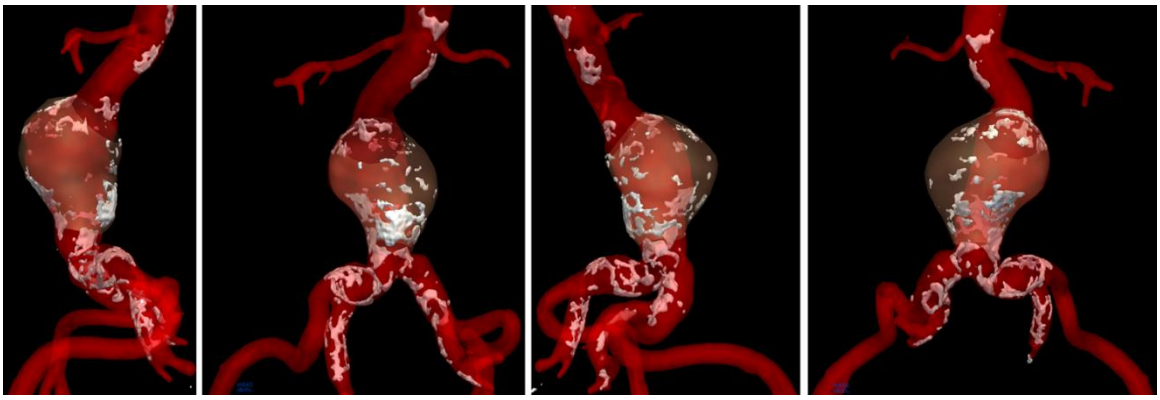

Figure 5.1: Selected patient-specific AAA model (solid red: lumen; semi-translucent red: ILT; white: Ca).

Due to the geometrical complexity in this patient-specific model, extensive time and efforts have been invested into image rendering from clinical data, 3D model generation, mold design and fabrication.

5.2.2 Surface Rendering & 3D Model Reconstruction

In order to design molds for a patient-specific geometry, first, a native continuous surface in 3D must be created from the clinical CT scans in 2D. This is also a prerequisite step for patient-specific numerical simulations, in which the surface smoothness is normally less critical. To the best of our knowledge, there is not yet a software to complete this task, particularly for a complex geometry involving tortuous vessels and inclusions having irregular shapes (ILT and Ca). As such, after testing with several combinations of surface rendering software, we have finally set up the following routine which appeared to be the best approach for our purpose (illustrated in Fig. 5.2).

1) Extract original 3D mesh (lumen, ILT and Ca) from 2D clinical data using ORS (Object Research System Inc., Canada) segmentation software, then inspect, clean and slightly smoothen this mesh with MeshLab (National Research Council, Italy).

2) Apply an in-house developed Python script to generate small native surfaces from the clean mesh, then combine them into a continuous surface with the Virtual Topology tool in Abaqus (Dassault Systèmes., France).

3) Re-mesh this large joint surface again with optimum element size and type in Abaqus; note that most mold design software cannot handle very heavy mesh, this is an important step to reduce the size of mesh without compromising too much anatomical details in the real geometry, many trial-and-error attempts would be expected.

4) Inspect and clean the re-meshed surface in Meshmixer (Autodesk Inc., USA) again, to avoid large curvatures, jumps, overlaps and singularities, particularly at the boundaries of Ca and ILT; the inner mold can be designed after this step.

5) Create splines and patches by "filling operation" in Meshmixer, to generate multiple surfaces of different mold layers with protruded areas indicating Ca or ILT, allowing subsequent offsets using SolidWorks (Dassault Systèmes, France) to design the outer molds.

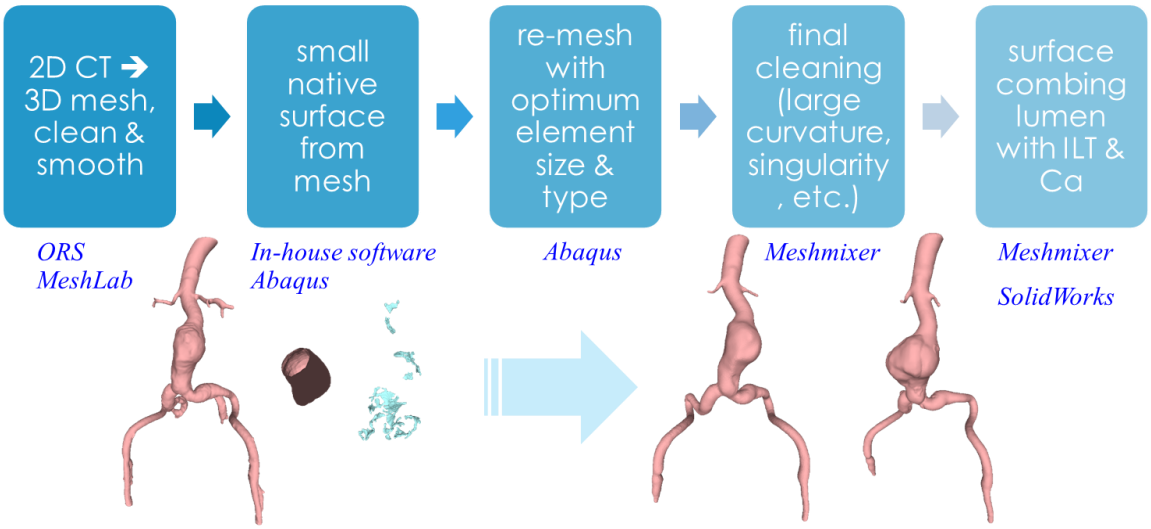

Figure 5.2: Flow charts illustrating the surface rendering routine to create native 3D surfaces of the lumen combining the ILT and Ca, from 2D clinical CT scans.

Although this process was tedious and time-consuming, the resulted surface was quite smooth with adequate details for Ca flakes and ILT, thus this routine could be also recommended for any design of patient-specific medical devices.

5.2.3 Molds Design & Development

Similar mold design concepts for the patient-inspired AMM were adopted, which consisted of an inner mold, and two sets of outer molds split in at least two halves (depending on the tortuosity of iliac arteries), as illustrated in Figure 5.3.

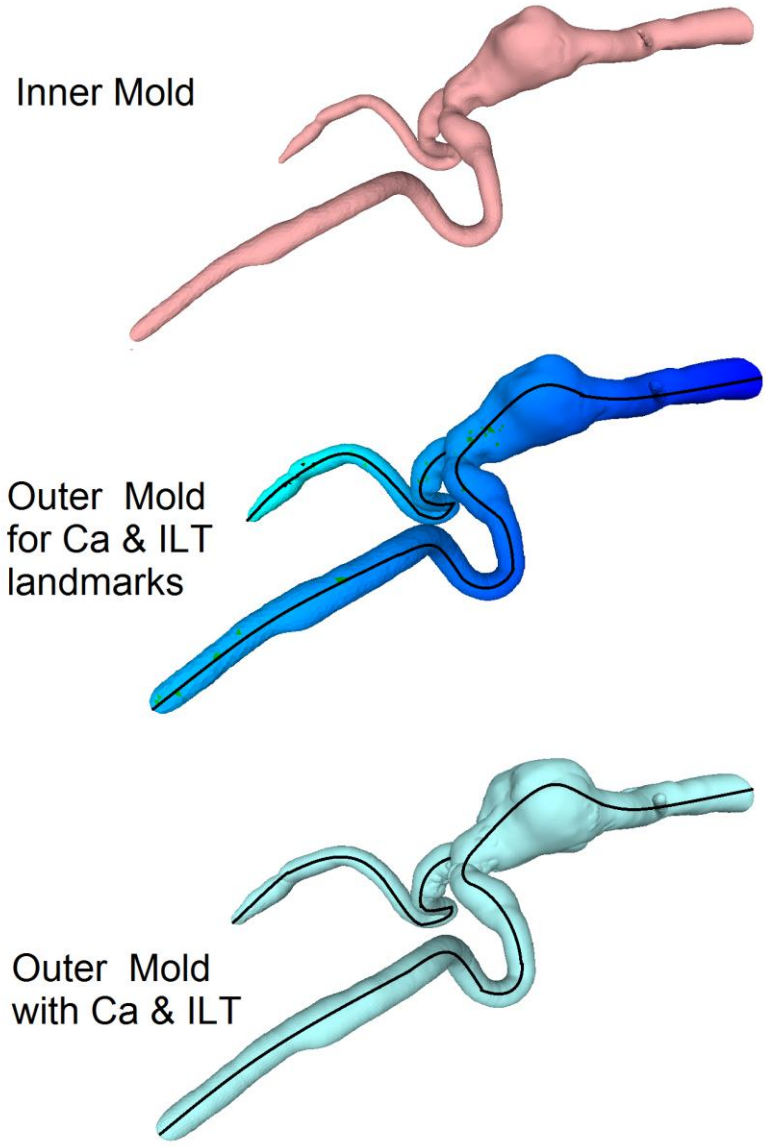

Figure 5.3: Mold design for the selected patient-specific AAA. The inner mold is shown at top (pink mold), outer molds creating landmarks for ILT are shown in middle (blue mold), and those curing the ILT onto AAA wall are shown at bottom (turquois molds, with slightly larger bulge due to ILT). The black lines drawn on the outer molds indicate the parting lines of the outer molds.

For the outer molds, one set was designed without considering the ILT, to create landmarks for the ILT at the first 3 cycles, shown as the blue mold in Figure 5.3. The second set was designed with the presence of ILT, allowing to cure PVA-C at that location during later cryogenic cycles, shown as the turquois mold in Figure 5.3. Of note, the parting line separating the outer molds were delicately designed with an aim to minimize the number of parts yet allow relatively easy detaching process.

Since the patient-specific AMM consisted of a relatively large aneurysm and very tortuous iliac arteries, the corresponding design of inter-connected inner molds required more detachable components and thus, elevating the risk of molds misalignment and the associated leaking of PVA solution. As such, using dissolvable material for the entire inner mold became an ideal option. Having tested with a number of dissolvable molding materials (sugar paste, low temperature wax, various dissolvable 3D printed support materials), we decided to use the water-soluble 3D printed PVA (natural PVA 3 mm filament, eSUN, China). By 3D printing the inner mold in this material, we not only created the complex 3D structure rapidly and accurately, but also protected the PVA-C from any chemical (alkaline dissolving agent for some 3D printed materials) or physical (heat or breaking apart manually) damages during the dissolving process. On the other hand, the inner mold was printed with 1.5 mm shell thickness and 20% honeycomb infill, providing an adequate mechanical strength with the minimum material to be dissolved. In order to accelerate the dissolving speed for such a big model, a system allowing clean water to be circulated continuously through the honeycomb structure was designed (Fig. 5.4), where the time to dissolve the entire inner mold has been dramatically reduced from a week to few days.

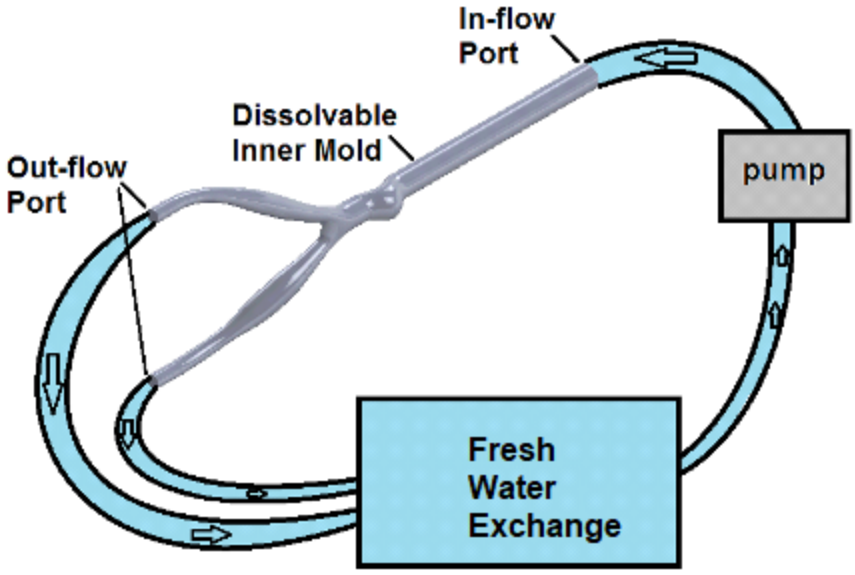

Figure 5.4: Schematic illustration of the dissolving system for dissolvable molds.

5.2.4 Mock Calcification

The ability to include Ca in AMM would be highly desired, and we are among the very first ones to design and develop an artificial calcified aortic tissue. Different fabrication methods were proposed, and the associated mechanical strength was tested and compared to relevant values on human samples from literature.

Calcified PVA-C

Two approaches to mimic the aortic Ca in PVA-C mockup were proposed as follows.

1) Since calcium carbonate ($CaCO_3$) has demonstrated similar elemental composition to human arterial Ca (27), it was selected to be the main constituent for the calcified PVA-C. Specifically, $CaCO_3$ powder was mixed directly with warm PVA solution (~30ºC) until homogeneous, then filled in a customized plastic mold for 8 cycles of cryogenic treatments to mimic diffuse calcium deposition. In order to mimic various degree of Ca, samples were prepared in different $CaCO_3$ weight concentrations, with the ratios of $CaCO_3$ powder to PVA solution being 1:1, 2:1, 3:1 and 4:1.

2) Since 3D printing technology could facilitate the reproduction of amorphous patient-specific Ca shapes, curing PVA-C with a 3D printed Ca inclusion embedded inside the specimen was also proposed. Assuming different density of ABS filaments could represent different degree of Ca, thin plate (<1 mm thick) and grid (~2 mm overall thickness) were designed, as illustrated in Figure 5.5. Printed parts were then inserted into the customized plastic mold filled with PVA solution for 8 cycles of cryogenic treatments.

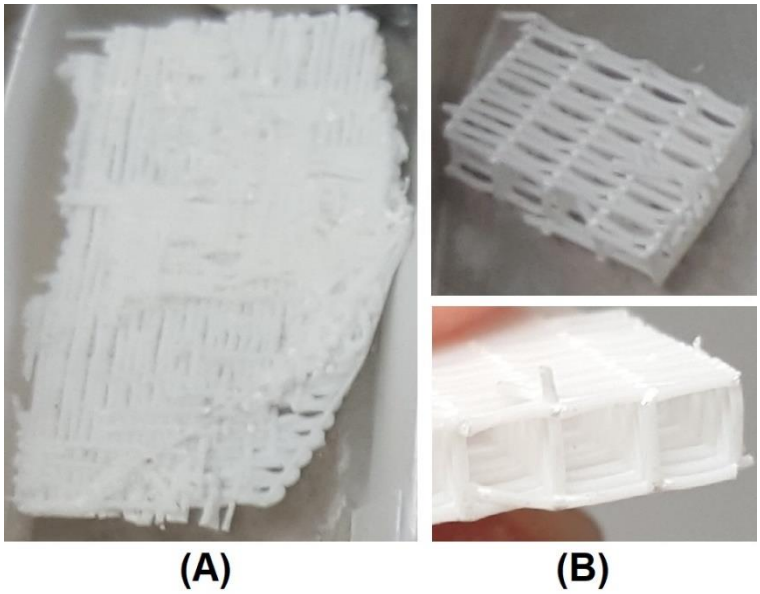

Figure 5.5: 3D printed ABS thin plate (A) and grid (B) as the core of calcified PVA-C specimen.

Mechanical Tests

All samples were prepared in the same dimension (40 mm x 10 mm x 3 mm, AAA wall with Ca are normally thicker) and three samples were repeated for each type of calcified PVA-C design. Uniaxial tensile tests similar to those for PVA-C wall, ILT and abdominal fat were performed (details explained in Chapter 4.2.2). Due to the insignificant soft-tissue behavior in those calcified samples, as well as the brittleness of certain samples, no preconditioning cycle was considered. Each sample underwent one loading cycle at a constant speed of 0.1 mm/S, with 10 Hz data acquisition, until sample failure or reaching one of the equipment limits (load or displacement).

5.3 Results

5.3.1 Molds Development

After many trials with various design prototypes, the final set of inner and outer molds have been developed, as shown in Figure 5.6. Due to the geometrical complexity in patient-specific anatomy, extensive time and efforts have been invested into image rendering from clinical data, mold design and fabrication. New challenges during this patient-specific mold design and prototyping are explained as follows.

- In order to develop CAD_{ENG} for the patient-specific molds, a native and refined surface must be generated from clinical data, with sufficient details representing the realistic anatomical characteristics while still able to be further processed with computer-aided engineering design software. Considerable attention must be paid to the transition from Ca inclusions to the aortic wall, where large curvature, singularities and sharp angles are very common at this boundary.

- Keeping in mind that the surface smoothness of molds is very crucial to eliminate bubbles during PVA-C fabrication, the printed water-soluble inner mold must be gently cleaned by water without affecting much of its dimension. Moreover, a very thin coat of varnish is applied evenly on the smoothened surface, to avoid any possible mutual contamination between the PVA solution (high water content) and the water-soluble mold.

- Unlike molds for the patient-inspired model, caps at all ends to align and seal the inner and outer molds are integrated into the inner mold for this patient-specific model. Note that several channels are also designed at the proximal end of inner mold to allow injection of PVA solutions. This new feature not only facilitates the mold assembling process, but also further reduce the total number of parts and thus, minimize any change of PVA solution leaking through gaps between the molds.

- For the outer molds, more intense surface treatments (explained in Chapter 4) are required, compared to the patient-inspired molds. As surface texture remains a big limitation in the current 3D printing technology, the number of Ca in irregular shape and the curvy nature of human aortic wall, together greatly elevate the challenge in obtaining a printed surface with acceptable quality.

- With the outer molds that split in two halves (indicated in the schematic mold design in Fig. 5.3), some minor cuts by the outer mold edge around the most tortuous area of iliac arteries have been observed while removing the outer molds. Therefore, the posterior part of outer molds is further divided into two segments at the most tortuous area (shown in Fig. 5.6), to allow easier detaching process without damaging the PVA-C mockup.

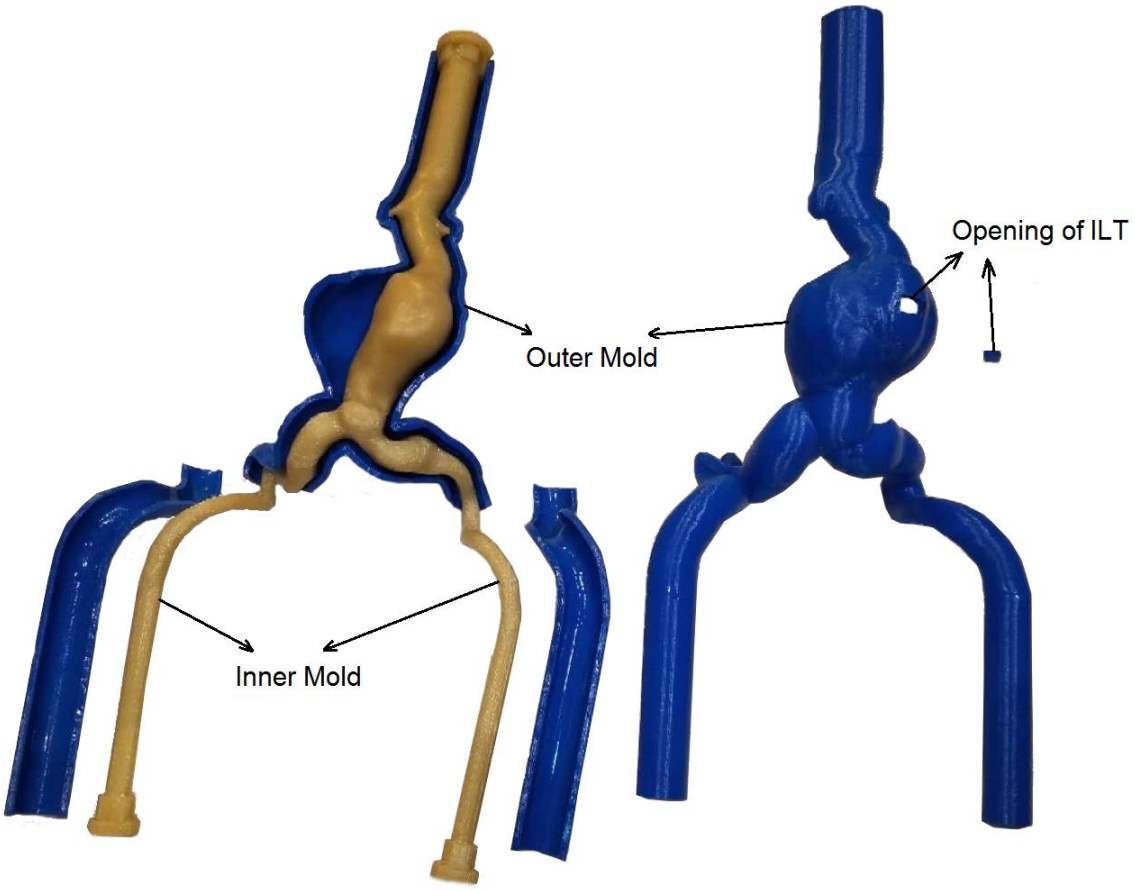

Figure 5.6: Final versions of refined molds developed for the patient-specific model. Outer molds are in blue, with further divided segments at the posterior side of tortuous iliac arteries; inner molds are in light brown.

As a result of the successful patient-specific molds development, subsequent fabrication of the PVA-C mockup, assembling to the existing anthropomorphic system, as well as corresponding in-vitro EVAR experiments, may all be accomplished in the near future.

5.3.2 Calcification Mechanical Properties

The uniaxial tensile test results in Figure 5.7 clearly reveal that higher concentration of $CaCO_3$ increases the stiffness of calcified samples, with the gradually rising slope of the stress-strain curve. Besides, the stress-strain behavior appears more linear with higher loads of $CaCO_3$, implying that the signature hyperelastic behavior of PVA-C, mimicking human vascular tissues, gradually diminishes. However, samples with higher $CaCO_3$ ratio fail at a lower strain, indicating the higher brittleness regardless of the greater concentration of Ca. It reflects that manually bonding Ca particles via PVA cryogenic process is far less sufficient to reproduce the material toughness as a result of natural Ca development process. Surprisingly, the stress-strain curves of ratios 2:1 and 3:1 almost overlap, but the one with lower $CaCO_3$ can sustain up till a greater strain, suggesting the saturation level of the $CaCO_3$ powder in PVA solution, where the hyper-elasticity starts to reduce.

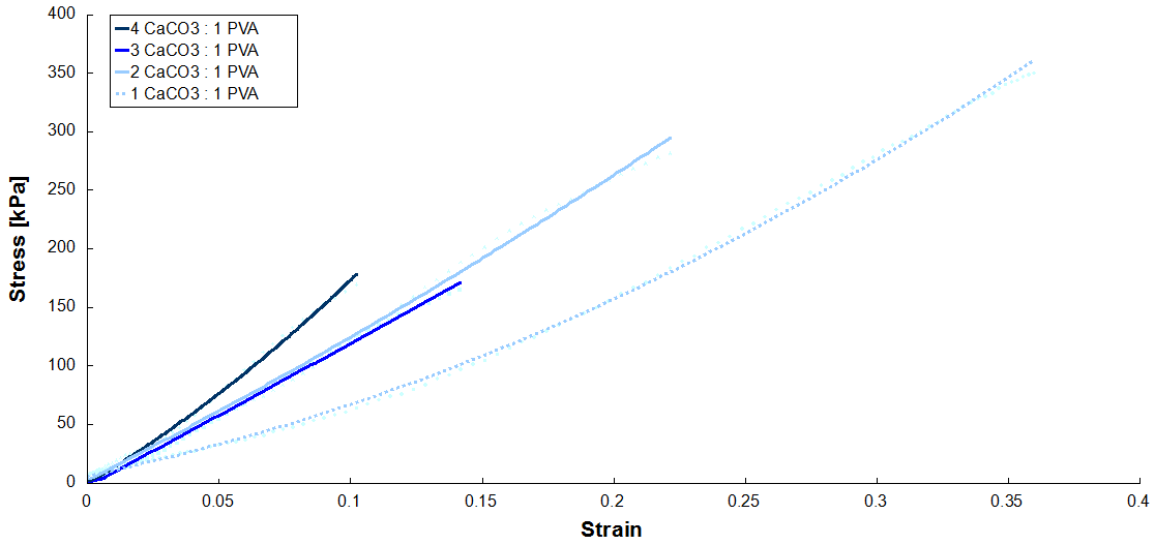

Figure 5.7: Stress-strain behaviors of calcified PVA-C samples made of different $CaCO_3$–to–PVA ratios.

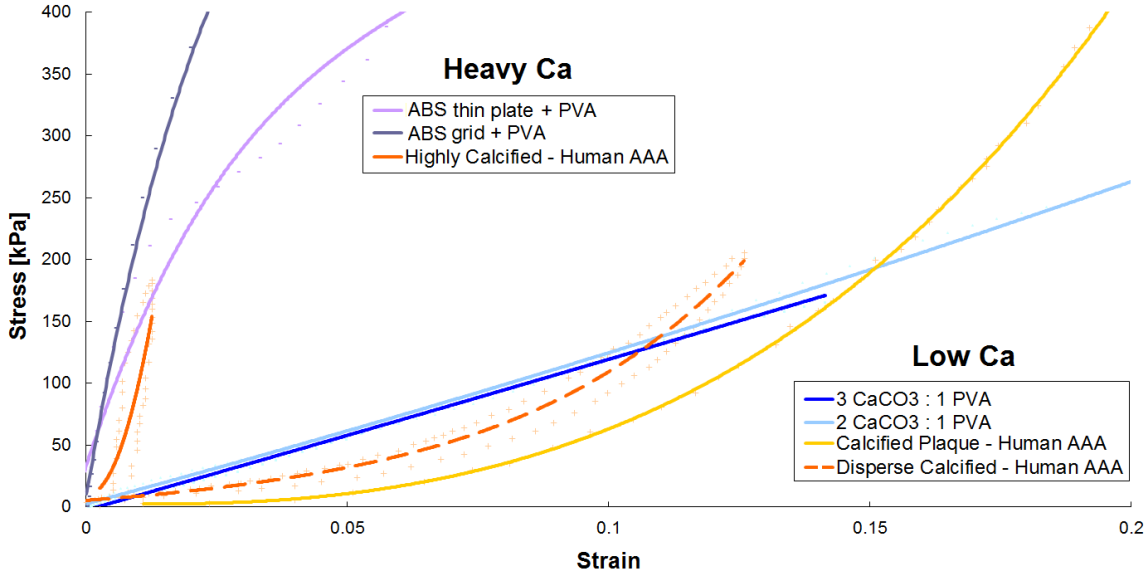

Figure 5.8: Stress-strain curves of calcified PAV-C samples (both with $CaCO_3$ mixture and ABS inclusions) in comparison with the literature values of human Ca in AAA.

The stress-strain behaviors of calcified PVA-C samples made of $CaCO_3$ mixture and ABS inclusion are illustrated in Figure 5.8, with further comparison to literature values of different degree of Ca in human AAA (73,189). Very little information on the material properties of Ca in human AAA can be found, in which a relatively wide range of mechanical strength has been reported. It is speculated that the density, dimension, as well as the micro-structure of Ca, all contribute to this variability. Nevertheless, our calcified PVA-C samples appear to exhibit stress-strain behaviors within the range reported from literatures. Among all four $CaCO_3$-to-PVA ratios, samples with 2:1 ratio seems to best approximate the dispersed calcified AAA and the calcified plaque, namely the low Ca case. On the other hand, the heavy Ca case represents the mechanical response from pure and dense Ca, for which the material strength is too high to achieve using $CaCO_3$ mixture. Nevertheless, the calcified PVA-C samples with embedded ABS inclusions (both thin plate and grid) show promising results, exhibiting the mechanical strength as high as those of the high Ca cases. Interestingly, ABS grid appears to provide slightly higher stiffness than the thin plate. It is speculated that, not only the inter-connected mesh can help redistribute loads from one direction, but the porous nature of grid may also result in a better integration with the surrounding hydrogel and thus, delaying the initiation of tearing at the ABS-hydrogel interface. Of note, the shapes of those stress-strain curves both reflect the dominant mechanical behavior of ABS over the hyperelastic PVA-C. Our preliminary results confirms the feasibility of using 3D printed ABS

to mimic the mechanical response of dense Ca in AAA; however further revisions on the structural design of ABS grid may help to fine-tune this option.

According to the evaluation of mechanical strength for all proposed calcified PVA-C design, ABS grid is selected for our patient-specific model. Besides the advantage in efficient replication of the unique and irregular Ca shapes, it also facilitates the insertion process during PVA-C fabrication. Precisely, while aligning the inner and outer molds, ABS grid can be easily hold in place at any specific Ca location thanks to its relatively thicker form (compared to thin plate which may slide around); moreover, the permeability of grid allows PVA solution to flow through and fulfil any space between the inner and outer molds, resulting in a one-step development of Ca embedded into AAA wall. As such, a more refined porous design, using Voronoi partition method (Meshmixer) to divide each Ca into connected honey-comb-like voids with round edges, has been applied to each Ca model. More specifically, the original very fine mesh of each Ca inclusion was 80% reduced with a shape preserving algorithm (Meshmixer) before applying Voronoi partition (dual edges, hexagonal grid, element dimension 0.5 mm and element spacing 0.2 mm). While capturing the main geometrical characteristics of Ca inclusions, the resulting scaffolds were composed of grids with smooth edges and large enough opening, allowing PVA to readily flow through without creating bubbles. Consequently, 3D printed ABS grids for all Ca in our patient-specific model are gently smoothened (same treatment as explained in Chapter 4) and ready to be embedded during the fabrication of PVA-C mockup, as illustrated in Figure 5.9.

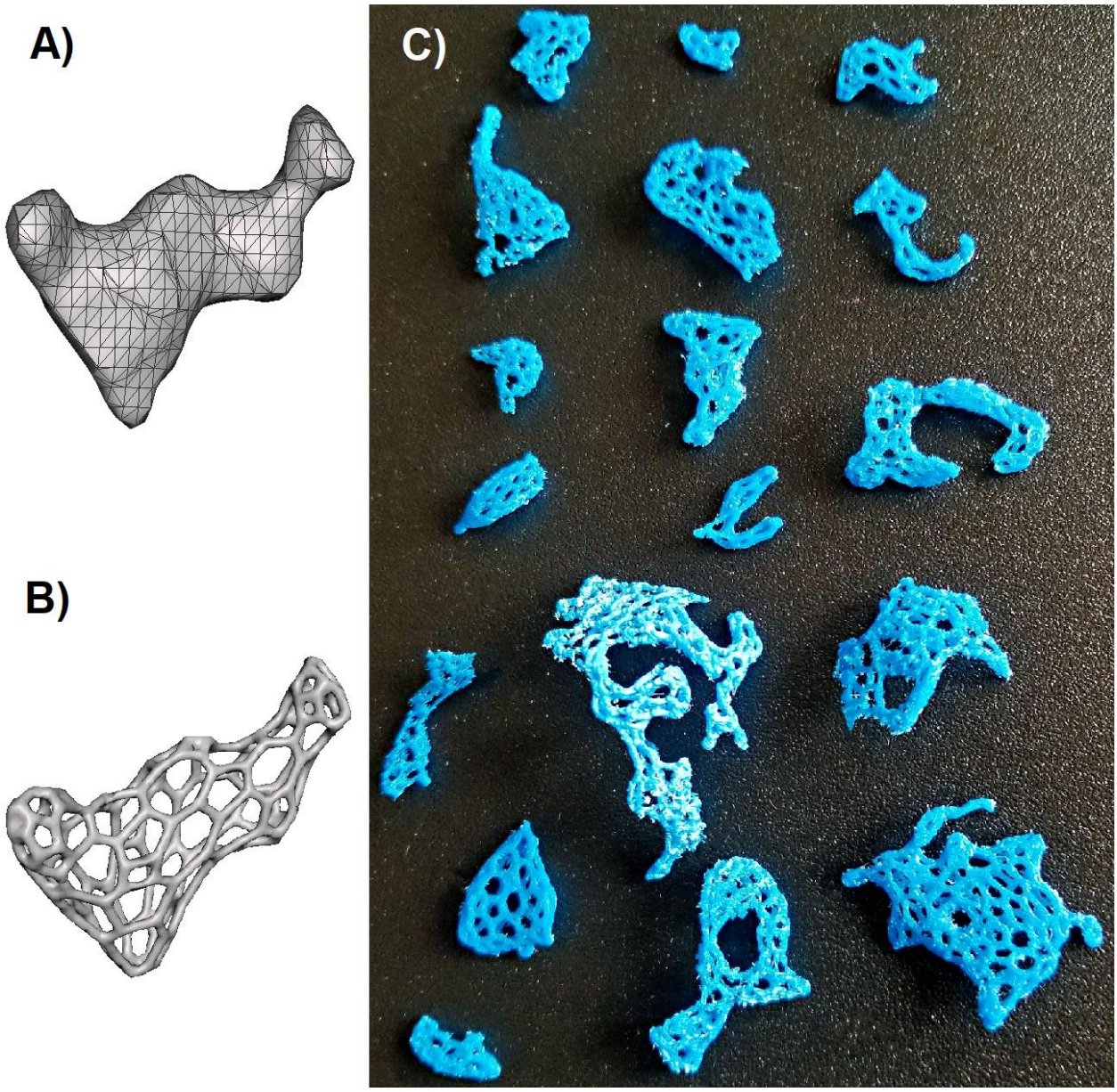

Figure 5.9: A) Illustration of the original mesh for a Ca inclusion; B) the corresponding Ca scaffold created by Voronoi partition; C) final 3D printed ABS grids, ready to develop Ca inclusions for the patient-specific PVA-C mockup.

5.4 Summary

This chapter mainly presents our preliminary attempts to develop the patient-specific AMM. Such patient-specific model is selected according to the additional pathological characteristics (large AAA, tortuous iliac arteries, severity of Ca) for which their effects on EVAR are challenging to be analyzed clinically or with numerical simulations.

First, a considerable amount of time and effort have been spent on creating the native, smooth and refined 3D surfaces from relatively coarse 2D clinical scans, with and without the presence of ILT and Ca. A novel strategy combining multiple image rendering and engineering design software has been proposed, which has proven to generate 3D surfaces with desired quality for subsequent mold design and development. Such strategy may also provide helpful guideline to design patient-specific medical devices.

After multiple iterations of mold design and prototyping, a final set of patient-specific mold has been developed. In comparison to the patient-inspired molds, new features such as the water-soluble inner mold with a rapid dissolving system, as well as the additional partition in the outer mold are presented. Precautions and solutions to overcome new challenges in 3D printing molds for patient-specific models with meticulous anatomical details are also suggested.

Finally, two novel approaches to develop calcified PVA-C for the patient-specific AMM have been proposed and evaluated. Specially, PVA-C with $CaCO_3$ mixture can mimic the mechanical response of low Ca (dispersed Ca and Ca plaques), whereas PVA-C with 3D printed ABS inclusions can reproduce the material strength of heavy Ca (pure Ca and highly calcified cases). Moreover, ABS grids in Voronoi patterns have also been successfully designed and developed for our patient-specific model.

In conclusion, this chapter presents a proof-of-concept study in creating a hydrogel based patient-specific AMM for future needs. Feasibility of our design concepts and development methodology have been demonstrated, providing valuable insights to future in-vitro analysis with patient-specific models.

6

DISCUSSION AND CONCLUSIONS

This chapter presents an overview of the original contributions of this research, with the potential clinical impact and significance being underlined. General discussions on the results of Ca analysis and AMM trials, the corresponding challenges and limitations are outlined. Future directions to expand the current research are recommended. Conclusions with respect to our research hypotheses and objectives are highlighted at the end.

6.1 Original Contributions

To date, the roles of Ca morphology and surrounding tissues of AAA with regards to EVAR treatments have not been investigated. Thus, it was hypothesized in this thesis that the morphological characteristics of Ca, together with its intrinsic properties, alter the global behavior of aortic wall and play an essential role in EVAR assessment. It was also hypothesized that incorporating the surrounding tissues improves the estimation of AAA deformation during EVAR. As such, the global objectives of this study are to gain more knowledge on the morphology of aortic Ca and its complex biomechanical interactions with endovascular devices, and to provide more insight on the biomechanical effects from surrounding tissues during EVAR. Consequently, the original contributions in generally knowledge and novel technology, in the context of those hypotheses and objectives, are outlined as follows.

First, to the best of the author's knowledge, this thesis presented the first thorough morphological characterization of Ca in AAAs, in terms of their volumes, shapes and locations. Unlike conventional methods in clinical evaluations of vascular Ca, a novel strategy, combining the quantitative analysis using 3D reconstructions from clinical CTs and the qualitative analysis through subsequent classifications of Ca shapes and locations, was proposed. Moreover, it allowed for the first successful attempt to study the combined effects of Ca morphological characteristics on the risk factors of AAA and EVAR complications. By taking specific combinations of Ca morphological data into account, the concerns raised from other clinical studies, regarding the influence of Ca in EVAR (such as: Ca location being more crucial than only considering the overall Ca extent (169); pounced Ca along iliac arteries being critical for device navigation and subsequent limb thrombosis (42); circumferential Ca around AAA neck being a predisposing factor for Type I endoleaks (52); and large Ca in the aneurysm sac being critical for sac shrinkage and subsequent Type II endoleaks) are confirmed and further refined (detailed discussion in Chapter 6.2.1). As a result, an approach to unify the contradictory understanding in Ca role was presented, providing not only an insight to improve the current evaluation of AAA rupture risk and EVAR assessment, but also a different perspective to investigate AAA pathophysiology.

Second, a novel hydrogel based anthropomorphic perfused mockup for AAA was presented in this thesis. Being mechanically, anatomically and pathologically realistic, this mockup provides

an ideal means to reverse engineering the biomechanical interaction of AAA and endovascular devices, while the cross-species and cross-specimen variabilities are eliminated. As such, the indispensable role of surrounding tissues, not only the spine but also the surrounding tissue, was discovered through EVAR experiments with this mockup. Such knowledge provides essential guidelines to refine the current computational models employed to study the biomechanics of AAA, as well as those in surgical planning platforms. Furthermore, a novel image rendering strategy, as well as two different approaches to include Ca in AMM were proposed. Such methodology may not only assist in developing a patient-specific AMM to address questions that are challenging to answer from clinical studies or numerical simulations, but also provide a valuable guideline to the design of patient-specific medical devices.

In summary, detailed original findings, outlined in the following Table 6.1, present potentially important implications to improve the overall quality of AAA evaluations, EVAR planning and outcome predictions.

	Original Findings/Contributions	**Implications**
Ca Analysis	• Ca exist in all AAAs, in which 25% are severely calcified.	• Ca needs to be considered in EVAR assessment.
	• Iliac arteries are the most common Ca location; bifurcation is the second common location. • Chance of having Ca at the proximal neck increases as the AAA becomes more calcified. • Chance of having Ca lateral to the ILT remains consistently low.	• Ca along the iliac arteries must be evaluated prior to EVAR. • For heavily calcified cases, attention must be also focused on Ca

Ca Analysis	• Most common location of Ca, in all shapes, changes from iliac arteries to aortic wall, as AAA becomes more calcified.	around the renal artery ostia.
	• As AAA becomes more calcified, the occurrence of a specific Ca shape at each location generally increases but not at the same pace, resulting in different representations of the common Ca shape across the AAA with different Ca loads. • Among all shapes, flake appears more dominant (except at the renal artery ostia for mild Ca), with 100% occurrence at certain locations upon reaching heavy Ca. • In general, flake is the most widespread Ca shape whereas strip is the least; stone is initially the most widespread shape at mild Ca, but reaches a plateau and becomes the least at severe Ca. • Along the development of Ca, the proportion of stone gradually decreases but that of strips increases; nevertheless, that of flake remains the same.	• A potential pathological evolution of Ca in AAA, with growing patterns from stone to strip, is suggested. • The importance of understanding the biomechanical effect of flake is highlighted.
	• For the same Ca shape (except stones), higher volume corresponds to higher risk of wall failure. • For the same Ca volume, flake imposes the highest risk of wall failure whereas stone bears the least risk.	• Ca geometrical configuration must be considered to evaluate AAA rupture risk.

Ca Analysis	• For Ca strip, higher risk of wall failure occurs when it orients along the direction of force.	
	• If the AAA is heavily and severely calcified, with more than 50% of Ca distributed below the bifurcation, the chance of having limb thrombosis is 60%. • If the AAA is heavily and severely calcified, with more than 20% of Ca and the presence of strip around the renal artery ostia, the chance of having peri-operative Type 1A Endoleak is 100%. • If the AAA is severely calcified, with less than 50% of Ca distributed below the bifurcation and the presence of Ca strip at the center, the chance of having post-operative Type 2 Endoleak is 50%.	• By excluding AAAs with specific combination of Ca morphological characteristics, the incidence of EVAR complications may be further reduced.
AMM Trials	• A hydrogel based perfused AMM for a patient-inspired AAA model is successfully developed. • Feasibility of the design concept and methodology to develop a similar AMM for the patient-specific AAA model are demonstrated.	• AMM is beneficial for issues that are challenging to verify with clinical studies and numerical simulations. • AMM may serve as a training and demonstration platform for medical specialists.

	• Surrounding abdominal fat prevents instantaneous vessel expansion under luminal pressure.	• Zero-pressure geometry must be considered for AAA simulations without surrounding tissues.
	• Surrounding tissues (fat and spine) are essential in withstanding forces from endovascular devices during EVAR procedure.	• Incorporating surrounding tissues in computational models may improve the accuracy of EVAR simulations.

Table 6.1: Summary of the original findings and contribution, with the corresponding implications or clinical significance.

6.2 Calcification Analysis

6.2.1 General Discussion on Results

The first part of thesis presents a novel approach combining the quantitative and qualitative analysis which has provided the very first comprehensive characterization of Ca physical morphology in AAA. Such detailed morphological data not only provide valuable insight to further investigate the pathogenesis of Ca, but also allow us to understand its biomechanical role from a different angle.

The presence of Ca in all AAA is confirmed, underlying the importance to consider any associated risks in predicting the interaction between AAA and endovascular devices. Risk of EVAR failures due to a single morphological factor has been suggested from literatures, which often bears relatively vague clinical implications; no attempt has been made on addressing multiple morphological factors simultaneously. A key message is then delivered: in order to best estimate the effect of Ca on EVAR, a multifactorial morphological index, combining the status of volume, shape and location, must be considered. As such, specific combinations of those morphological data have been found critical to certain EVAR complications: Type 1A is highly associated with severe Ca having more than 20% of its overall Ca distributed around the rental artery ostia, and with the presence of Ca strips; limb thrombosis is associated with severe Ca having more than half of its Ca distributed below the bifurcation; whereas for severe Ca having less than half of its Ca below the bifurcation, the presence of Ca strip at the center of AAA may induce the risk of Type 2 endoleaks. These morphological details along with their clinical implications allow efficient identification of the vulnerable case without extensive clinical experience nor costly computer simulations.

Moreover, this Ca analysis also reveals that, predictions based on a single or multiple morphological factors may lead to completely opposite results. For instance, simulations with our simplified models have indicated that, a patient with mild Ca but mostly in flakes or vertical strips has indeed higher risk of wall rupture than another patient with heavy Ca but mostly in stones. Although not common, both cases are possible scenario based on our clinical observations. Consequently, while taking the combined effects from multiple morphological characteristics into

account, some of the common expectations may be overturned, shedding a light on the contradicting interpretations of Ca role from literature.

Interesting clues on the development patterns of Ca are disclosed. Ca appears more and more pronounced from AAA neck towards iliac arteries, which is very noticeable in mild Ca but gradually evens out as AAA becomes more calcified. It is speculated that the absence of wall vascularization (via vasa vasorum) in the abdominal aorta, as well as the gradual increase of flow resistance below the renal arteries, both play an essential role. Moreover, shear stress and gradients are higher in the downstream tortuous vessels and the branch entrance due to the bifurcated turbulent flow, which favor Ca development as a result of the bio-mechanically induced cellular pathways; a roadmap of Ca development is therefore suggested. On the other hand, the transition observed in Ca shape extensiveness and proportion from the mildly to severely calcified cases, specifically, Ca stones gradually grow into strips and eventually flakes, reflects a growth pattern of Ca. Finally, AAA diameter is significantly larger in the case with higher Ca ratio at the region superior to the AAA. It is speculated that the more rigid AAA neck constricts the upstream blood flow and imposes a jet effect with subsequent vortex at the aneurysm sac, thereby promoting the aortic dilation. Further investigations into these observations would elicit more answers to the pathogenesis of Ca, as well as the preventive measures for AAA rupture.

6.2.2 Assumptions, Limitations and Challenges

The discoveries from Ca analysis and the corresponding clinical impacts are stated within the limits of the scope of study and the assumptions made.

Depending on the context of clinical studies, the threshold value utilized to segment Ca from the vessel wall may vary dramatically, from 130 to 1000 HU. First, the location of Ca is a determinant factor. For example, 130 HU is commonly used as the lower bound threshold for coronary artery calcium scoring, where micro-calcifications as well as any low-density Ca are all essential for prognosis in CAD. However, the goal of this study is to understand the role of Ca in AAA, and also from a macroscopic perspective: the volume, shape and location associated biomechanical effects on EVAR. Of note, the biomechanical role of low-density Ca and micro-calcifications in EVAR assessment may be trivial, as the corresponding mismatch in aortic wall compliance is relatively small, therefore not bringing a substantial value in this research. Second, patients selected in this study are not from a well-controlled group in terms of screening protocols, but rather from an unbiased representation of the total AAA population. As such, the amount of contrast used, clinical setup, as well as the screening time (year) were not consistent in this patient group. Apart from the 500 HU being applied in several similar studies, this value was also selected by balancing between the volumes of Ca detected from scans under very different conditions. Although it might not capture the most precise characteristics for each patient, the resulted segmentations should sufficiently represent the trend and distribution of Ca for this patient group.

For the classification of Ca loads, it was proposed primarily according to the distribution of Ca volumes in our patient group. Since image quality is the main the selection criterion for this patient group, no bias on any risk factors associated with Ca development is presented. Hence, findings from this patient group should reflect the real status from the AAA population. Moreover, clinical data was processed periodically wherein similar distributions were observed every time with an increased number of patients, justifying the reproducibility of this classification.

The ROI for segmentations was selected according to the area most commonly treated under EVAR (area covered by SG in general). As vessel tortuosity may vary greatly within the same ROI across a patient group, especially at the iliac arteries, Ca volume was further normalized by the

corresponding vessel volume to obtain a more reliable representation of the Ca status. Besides, the total Ca volume, even in a specific region defined in this thesis, from a big-tall male can be substantially higher than that from a short-skinny female, resulting in misinterpretation of the Ca distribution and severity. Hence, Ca ratio in each region (normalized by the total Ca volume) was employed, not only to evaluate the combined morphological effects, but also to eliminate such bias. Of note, some very rare situations (not seen in this study) may not be sufficiently captured, for example, a mild calcified AAA with Ca mostly around the proximal neck will have a very high Ca ratio in this region. Further normalizing this Ca ratio by the total AAA volume is therefore recommended, especially for future studies with a larger sample size, to more accurately reflect the Ca severity and distribution regardless of the huge variation in AAA geometry.

The choice of Ca locations were initially selected with the endovascular specialist according to their clinical significance. A thorough characterization on the distributions of Ca volumes, the occurrence and the extensiveness of different Ca shapes has been done with the reference of these locations. However, the diversity in locations, shapes and volumes all together resulted in a number of variables that is too large for our samples size (total number of patients we have). As such, based on the similarity in characteristics observed at certain locations, a further simplified location classification was proposed for the multifactorial statistical analysis. Although results with valuable clinical implications are derived with this simplified classification, and that fewer locations are more practical clinically, the entire analysis would not be reliable without the details obtained from the initial analysis with finer location divisions.

The triple-factors analysis, considering multiple Ca morphological characteristics simultaneously, has presented an interesting and insightful approach to evaluate the impact of Ca on EVAR; discoveries within the scope of this work have potential clinical significance. Given the small sample size on top of the relatively low occurrence of EVAR failure, future revisions and validation with a much larger sample size, will be crucial to draw stronger conclusions on the correlations between Ca morphological characteristics and EVAR outcomes. For any unbalanced research which often happens in clinical evaluations of some rare conditions, one solution would be to first collect more data so that the size of the smaller group (i.e., Type 1A endoleak) becomes sufficiently large (depending on the hypothesis and the number of independent variables), then

randomly sample the larger group from this population (i.e, no Type 1A endoleak) to get an equally sized comparison group.

Finite element analysis is utilized in this study to elucidate the combined effects of Ca shape and size, which is a challenging task for clinical analysis due to the variations of *in vivo* data. Assumptions (idealized geometries, simplified Ca-wall interface, absence of realistic pressurized environment, material models from literature, etc.) were made to lower computational cost, to exclude irrelevant factors and focus on the main concern. Of note, simulations with simplified models only provide a preliminary evidence, supporting ideas in the hypothesis from a numerical standpoint. More robust simulations with sophisticated models, especially the patient-specific geometry, will be beneficial to understand the complete mechanism with respect to the morphological effect.

Finally, time and human power are the biggest challenges in this Ca analysis. First, patient clinical data was collected from all sources to obtain comparable information in terms of demographics, Ca risk factors, comorbidities and EVAR complications. In addition, all collected data has been verified by at least two medical specialists for its validity. At the end of this review process, around 25% of all those patients were excluded. For example, smoking history and BMI (especially the height) were not always available; history of PVD and COPD were not easily accessible due to different hospital network; current status of CAD, CKD and diabetes were unclear (no follow-up and relevant pharmaceutical records). Of note, this 25% patients also included those with CT scans not meeting the selection criteria for this study (explained in Chapter 3). Second, segmentation of Ca was not fully automatic as we had to manually exclude the spine or calcified spots from tissues that are very close to the Ca in AAA. Similarly, at least two persons were then assigned to identify Ca in different shapes at different locations for each patient, to minimize the subjectivity of observer during the qualitative analysis. Substantial time, certain knowledge in clinical data evaluations and imaging analysis are all required for the above mention tasks, which strongly limit the potential to expand the scope of study. As a result, the ability to substitute this process by an artificial intelligence (AI) model through machine learning algorithm becomes especially advantageous. However, taking into account the number of variables along this process, a significant amount of data must be provided to allow sufficient training for the AI model and thus, a much bigger patient group will be required in the first place.

6.3 Anthropomorphic Mockup

6.3.1 General Discussion on Results

The second part of thesis presents the design and development of a PVA-C based AMM for AAA in a patient-inspired geometry, the subsequent EVAR experiments, as well as the proof-of-concept application for a patient-specific model. Of note, experimental results from our patient-inspired model, representing the most common anatomical and pathological characteristics (i.e. aneurysm sac, ILT, bifurcating iliac arteries, surrounding fat and spine), may sufficiently reflect the major biomechanical response of AAA during EVAR (i.e., aortic centerline displacement, vessel expansion). Whereas for certain patient-specific characteristics (i.e., irregular Ca pattern, iliac artery tortuosity), the variability is too large to evaluate any substantial impact on the overall AAA deformation.

In general, tensile test results match well with our previous observations in a more detailed study for PVA-C mechanical characterization (219), confirming the reproducibility of the desired elasticity in PVA-C. After iterations of mechanical testing, the optimal sets of cryogenic parameters have been determined for PVA-C, to mimic the mechanical response of AAA wall, ILT and surrounding abdominal fat, especially within the context of EVAR. In addition, two approaches creating calcified PVA-C have been suggested and confirmed to mimic the mechanical strength of Ca in various degree.

To date, most vascular mockups have been developed to address a single or few physiological parameters. For AAA which normally involves more parameters, the validity of using traditional mockups to reproduce the realistic biomechanical interaction with endovascular devices is in question. An extensive effort has therefore been made towards creating an AMM suitable for EVAR assessment in this study. Specifically, our AMM reproduces not only the anatomical characteristics, but also realistic mechanical behavior, especially the elasticity and friction, of the main AAA components (aortic wall and ILT) and surrounding structures (abdominal fat and spine). As friction is becoming a leading concern in Benchmark testing for medical device navigation (256), this AMM offers tremendous value to ameliorate the current design of EVAR catheters. By incorporating major surrounding structures, as well as the luminal and abdominal pressure into

this AMM, we provide by far the most sophisticated and comprehensive *in-vitro* model to study the biomechanical interaction between AAA and medical devices.

From our mock EVAR experiments, the biomechanical effects of surrounding structures, especially the surrounding fat, was elucidated. First, it helped to reduce instantaneous vessel expansion under luminal pressure, providing more realistic AAA responses compared to in vivo data (0.31~1.27 $10^{-5}Pa^{-1}$ distensibility and 0.3%~4.8% area change over a cardiac cycle) (257,258). The importance to consider zero-pressure geometry in simplified simulations without surrounding tissues was also underlined. Second, it helped to significantly resist forces associated with catheter navigation and SG deployment during EVAR. The difference in centerline deviations implies a dampening effect of the surrounding fat when an external force is introduced by catheter or SG, which provides an important framework to account for the interactions with those endovascular devices. Of note, surrounding tissues are still ignored or simplified as an artificial boundary condition in most studies of AAA biomechanics, especially when simulating the interaction with medical devices during EVAR (7,259), which can impact the predictive capability (59,260). Our results therefore provide an insight to refine existing numerical models for more realistic and accurate prediction in EVAR outcomes.

Finally, attempts to further extend and refine the current design concept to develop a patient-specific AMM have shown promising results. The feasibility of our revised methods, in particular, the use of a water-soluble inner mold is confirmed. Although the complete development of a patient-specific AMM is not demonstrated here, it should be relatively straightforward according to the methodology presented in this thesis. Moreover, a novel strategy combing various image rendering software has been proposed, successfully creating native and smooth 3D surfaces from relatively coarse 2D clinical scans. It then allows the possibility to further edit with regular engineering computer aided design (CAD_{ENG}) software, providing valuable pathway to the design of patient-specific medical devices.

6.3.2 Assumptions, Limitations and Challenges

Several limitations exist in the current study, especially for the friction tests. First, measurements with silicone under the normal load greater than 0.1 N was not possible, because the friction force became too high and exceeded the limit of load cell. Nevertheless, 0.1 N is too small to represent the navigation force in the case of tortuous iliac arteries, our observation thus confirms that tissue-mimicking silicone could not sufficiently mimic the frictional behavior of human vessel. Second, all Stribeck curves of 0.1 N normal load shift drastically upwards. It implies that the friction between the aortic wall and the catheter at low normal load was significantly affected by the surface flatness; it may also be influenced by the sensitivity of a high-precision load cell, which remains to be clarified in future. Third, the range of sliding velocity limited us from having a complete description of the PVA-C frictional behavior at both elastic friction and hydrodynamic lubrication regions. Stribeck curves from our results suggest that both materials are only under elastic friction (261), whereas hydrodynamic lubrication dominated by the lubricating liquid has never been reached in our experiments due to the limitation in sliding velocity amplitude. Nevertheless, according to the comments and experience from our endovascular specialists, the sliding speeds in this study cover far beyond the catheter navigation speed in clinical practice.

Another assumption was made for the overall expandability of the mockup. Although PVA-C fat has been confirmed to sufficiently mimic the elasticity of human perivascular fat, the overall expandability, taken into account the surrounding organs and skin, was achieved by gently wrapping PVA-C fat cubes around the vessel with a cotton mesh. Further validation on the overall expandability with literature values or in-vivo data will be helpful to support this assumption.

A big advantage of our AMM is the durability and material cost, as explained in Chapter 4; however, some of this advantage is loss in the patient-specific case, because the water-soluble inner mold is a single-use product. On the other hand, the success rate of PVA-C mockup fabrication, especially for such a delicate AMM, greatly depends on the skills and experience of the developer, mainly due to the number of challenges discussed as follows.

The biggest challenge in mold design is the inter-locking system of the detachable inner mold for our patient-inspired AMM; whereas the design of water-soluble inner mold for the patient-specific AMM is relatively simple. The inter-locking system should not only address the aneurismal and bifurcating characteristics of AAA, but also facilitate the demolding process. Although PVA-C is deformable, minor damage can be incurred while removing the inner mold and can cause hydrogel tearing under pressure. Hence, sharp edges and corners were avoided in each inter-locking component. Besides, the connections between components were designed in a laminated manner to prevent leaking of the PVA solution, as well as bending or deflection along the assembled mold.

Moreover, some challenges in mold development are also worth noting. One is the printing orientation, especially for the inter-locking system. As one of the limitations in FDM (fused deposition modeling) printing technology, the finished product is often weaker along the vertical direction. Thus, the printing orientation was carefully selected to maximize the strength and durability of molds, especially at the connection tips of inner molds. Second, as a well-known issue for all PVA-C hydrogel fabrication, bubble formation has been a major obstacle in the journey of our AMM development, because any tiny voids created inside the thin PVA-C wall can easily initiate rupture under pressure. The success rate of mockup development was not under control until a series of post-processing steps were well established, specifically, the manual sanding, acetone-treatment, as well as thin varnish coating.

Finally, due to time and certain equipment limitations (unknown issues of the programmable fridge towards the end of this study), the final assembled patient-specific AMM was not presented here. Nevertheless, solutions to the foreseeable hurdles have been proposed and evaluated, for example the final mold design and fabrication, the concept of dissolvable mold to reproduce the complex geometry, the approaches to include Ca as well as the actual models. With dedicated craftsmanship, time, and proper equipment, this patient-specific AMM could be readily developed.

Despite the current limitations and challenges in development, being biomechanically, anatomically and pathologically realistic, this AMM can provide an excellent *in-vitro* environment for numerical model validation, medical device evaluation, academic demonstration and medical training.

6.4 Recommendations For Future Works

Coming along with the novel approach to analyze Ca and the original creation of AMM presented in this thesis, a door towards refinement on these novelties, as well as further discoveries in relevant domains is open. Based on the limitations and challenges discussed in the previous section, future works are recommended but not limited to the following.

First, a more profound study on the thresholds separating Ca from the human aortic vessel under different clinical settings, specifically, the amount of contrast used, will be critical for many clinical researches on Ca. In addition, it is more recommended with freshly harvested Ca from human AAA (more likely from open surgeries where a portion of the tissue may be removed) to minimize any cross-species variabilities. Moreover, it allows to better understand the relationship between the density of Ca and the corresponding imaging manifestation, which will be insightful to classify Ca with respect to its intensity.

The quantitative and qualitative analysis presented in this study provides a helpful guideline for future clinical studies in this field. In particular, a protocol defining the group of patients with a more controlled imaging procedure (contrast used, imaging device and settings, time range, etc.) and the availability of patient demographic data, comorbidities and follow-ups after EVAR is preferred, to minimize the unnecessary time spent on processing data that turns out not qualified for subsequent studies.

Conducting similar Ca analysis with a much increased sample size is highly recommended, mainly to train AI models for two different applications. First, to facilitate or even substitute the time-consuming Ca segmentation and classification procedure. Second, to provide reliable predictions on EVAR complications and complexity. The latter will require an even larger sample size, or a very specific patient group, due to the low incidence of certain EVAR complications. Nevertheless, both AI models will be especially beneficial for direct clinical evaluation in future, providing additional values to the relatively simple Ca scoring system without using any patient-specific numerical simulations.

As some interesting clues in the development patterns of Ca are revealed in this study, further investigations in the pathogenesis of Ca, taking into account both the hemodynamic effects and

the bio-mechanically induced cellular pathways in the aortic wall, will converge our knowledge of the initiation and progression of Ca in AAA.

The proposed representative models and the significant representations of Ca shapes distribution display the most common Ca characteristics that may have important clinical implications. It is therefore highly suggested to implement them in AMM for *in-vitro* evaluations, or in more sophisticated computational models for simulations, to reveal any other significant effects of Ca under different circumstances.

As the scope of friction tests presented in this study are limited by certain equipment setups, revisiting the measurement with low normal load will provide a clearer evidence comparing the frictional behavior of different materials (human tissues, PVA-C and silicone). In addition, extending the sliding velocity to cover the hydrodynamic lubrication regions may allow for more complete characterization of the friction profile (Stribeck curve) between walls and endovascular devices.

Although EVAR in-vitro experiments have only been performed under the static pressure in this study, our pressurizing system with features connecting the perfused mockup provides a potential for future exploration in a dynamic environment. More specifically, a pulsatile pump can be incorporated to reproduce the diastolic and systolic flow, with blood mimicking fluid (especially the viscosity) to investigate the hemodynamic profile during EVAR.

Last but not least, the patient-specific AMM should be the major task to be completed in the soon future, with the molds already prepared and methodology evaluated in this study. Subsequent validation with clinical data is also required. As this patient model presents the main wall degeneration characteristics of AAA, especially in terms of Ca morphological characteristics, EVAR experimental results may unravel the role of wall biomechanics in EVAR assessment, particularly at the pre-delivery and delivery stages. To date, the boundary of Ca and the tortuosity of iliac arteries are the main obstacles in simulating endovascular device navigation. This patient-specific AMM, having both decent amount of Ca and tortuous iliac arteries, will provide guidance to fine-tune existing numerical models, which may ultimately improve procedure planning, outcomes prediction, effectiveness and durability of EVAR procedures.

6.5 Summary

In conclusion, the thesis presented the first quantitative and qualitative analysis on Ca in AAA, providing a thorough characterization of Ca physical morphology. The effects from a single, double and multiple morphological characteristics of Ca have been associated with different clinical manifestations, especially EVAR complications. By considering specific combination of those morphological characteristics, some common expectations based on the intrinsic material property could also be inverted. It is confirmed that not only the intrinsic properties but also the morphological characteristics of Ca together alter the global behavior of aortic wall and play an essential role in EVAR assessment.

In addition, the thesis presented by far the most comprehensive AMM for AAA, reproducing realistic deformation responses, frictional behavior, anatomical and diseased characteristics observed with AAAs. The biomechanical interaction between AAA and endovascular devices during EVAR has been evaluated using this AMM, with and without the surrounding fat. The results underlined the indispensable role of surrounding tissues, not only the spine but also the abdominal fat, as to account for realistic interactions with endovascular devices.

The discoveries and novel approaches within the scope of the thesis have potential clinical significance which, with future revisions and validation, could improve the current knowledge in vascular biomechanics and EVAR assessment.

REFERENCES

1. The top 10 causes of death [Internet]. [cited 2019 Mar 22]. Available from: https://www.who.int/news-room/fact-sheets/detail/the-top-10-causes-of-death

2. Kent KC. Abdominal aortic aneurysms. N Engl J Med. 2014 Nov 27;371(22):2101–8.

3. Canadian Task Force on Preventive Health Care | Abdominal aortic aneurysm—clinician summary [Internet]. [cited 2019 Mar 22]. Available from: https://canadiantaskforce.ca/abdominal-aortic-aneurysm-clinician-summary/

4. NVSS - Mortality tables - leading causes of death - LCWK1 [Internet]. 2019 [cited 2019 Mar 22]. Available from: https://www.cdc.gov/nchs/nvss/mortality/lcwk1.htm

5. Salata K, Hussain MA, Mestral C de, Greco E, Aljabri BA, Mamdani M, et al. Comparison of outcomes in elective endovascular aortic repair vs open surgical repair of abdominal aortic aneurysms. JAMA Netw Open. 2019 Jul 3;2(7):e196578–e196578.

6. Sidloff David, Stather Philip, Dattani Nikesh, Bown Matthew, Thompson John, Sayers Robert, et al. Aneurysm global epidemiology study. Circulation. 2014 Feb 18;129(7):747–53.

7. Roy D, Holzapfel GA, Kauffmann C, Soulez G. Finite element analysis of abdominal aortic aneurysms: geometrical and structural reconstruction with application of an anisotropic material model. IMA J Appl Math. 2014 Oct 1;79(5):1011–26.

8. Walker TG, Kalva SP, Yeddula K, Wicky S, Kundu S, Drescher P, et al. Clinical practice guidelines for endovascular abdominal aortic aneurysm repair: written by the standards of practice committee for the society of interventional radiology and endorsed by the cardiovascular and interventional radiological society of Europe and the Canadian Interventional Radiology Association. J Vasc Interv Radiol. 2010 Nov 1;21(11):1632–55.

9. Karthikesalingam A, Holt PJ, Vidal-Diez A, Ozdemir BA, Poloniecki JD, Hinchliffe RJ, et al. Mortality from ruptured abdominal aortic aneurysms: clinical lessons from a comparison of outcomes in England and the USA. The Lancet. 2014 Mar 15;383(9921):963–9.

10. Li X, Zhao G, Zhang J, Duan Z, Xin S. Prevalence and trends of the abdominal aortic aneurysms epidemic in general population - a meta-analysis. PLOS ONE. 2013 Dec 2;8(12):e81260.

11. Aggarwal S, Qamar A, Sharma V, Sharma A. Abdominal aortic aneurysm: a comprehensive review. Exp Clin Cardiol. 2011;16(1):11–5.

12. Kubota Y, Folsom AR, Matsushita K, Couper D, Tang W. Prospective study of lung function and abdominal aortic aneurysm risk: The Atherosclerosis Risk in Communities study. Atherosclerosis. 2018 Jan 1;268:225–30.

13. Aortic Aneurysm Fact Sheet | Data & Statistics | DHDSP | CDC [Internet]. 2018 [cited 2019 Mar 26]. Available from: https://www.cdc.gov/dhdsp/data_statistics/fact_sheets/fs_aortic_aneurysm.htm

14. He CM, Roach MR. The composition and mechanical properties of abdominal aortic aneurysms. J Vasc Surg. 1994 Jul;20(1):6–13.

15. Chamberlain CM, Ang LS, Boivin WA, Cooper DM, Williams SJ, Zhao H, et al. Perforin-independent extracellular Granzyme B activity contributes to abdominal aortic aneurysm. Am J Pathol. 2010 Feb;176(2):1038–49.

16. Rahimi SA. Abdominal aortic aneurysm: practice essentials, background, anatomy. 2019 Feb 2 [cited 2019 Mar 26]; Available from: https://emedicine.medscape.com/article/1979501-overview

17. Folkesson M. Significance of intraluminal thrombus in abdominal aortic aneurysm [Internet]. Inst för molekylär medicin och kirurgi / Dept of Molecular Medicine and Surgery; 2013 [cited 2019 Mar 26]. Available from: http://openarchive.ki.se/xmlui/handle/10616/41265

18. Piechota-Polanczyk A, Jozkowicz A, Nowak W, Eilenberg W, Neumayer C, Malinski T, et al. The abdominal aortic aneurysm and intraluminal thrombus: current concepts of development and treatment. Front Cardiovasc Med [Internet]. 2015 May 26 [cited 2019 Mar 26];2. Available from: https://www.ncbi.nlm.nih.gov/pmc/articles/PMC4671358/

19. Tomazic BB. Physiochemical principles of cardiovascular calcification. Z Für Kardiologie. 2001;90 Suppl 3:68–80.

20. Peters F, Epple M. Simulating arterial wall calcification in vitro: biomimetic crystallization of calcium phosphates under controlled conditions. Z Für Kardiologie. 2001;90 Suppl 3:81–5.

21. Lindholt JS. Aneurysmal wall calcification predicts natural history of small abdominal aortic aneurysms. Atherosclerosis. 2008 Apr;197(2):673–8.

22. Dautova Y, Kozlova D, Skepper JN, Epple M, Bootman MD, Proudfoot D. Fetuin-A and albumin alter cytotoxic effects of calcium phosphate nanoparticles on human vascular smooth muscle cells. PLoS ONE. 2014 May 21;9(5):e97565.

23. Li Y, Wang X, Zhu M, Yang C-Q, Lu A, Li K, et al. Mineralogical characterization of calcification in cardiovascular aortic atherosclerotic plaque: A case study. Mineral Mag. 2014 Aug 1;78(4):775–86.

24. Doherty TM, Fitzpatrick LA, Inoue D, Qiao J-H, Fishbein MC, Detrano RC, et al. Molecular, endocrine, and genetic mechanisms of arterial calcification. Endocr Rev. 2004 Aug;25(4):629–72.

25. Proudfoot D, Shanahan CM. Biology of calcification in vascular cells: intima versus media. Herz. 2001 Jun;26(4):245–51.

26. Sakalihasan N, Michel JB. Functional imaging of atherosclerosis to advance vascular biology. Eur J Vasc Endovasc Surg. 2009 Jun;37(6):728–34.

27. Marra SP, Daghlian CP, Fillinger MF, Kennedy FE. Elemental composition, morphology and mechanical properties of calcified deposits obtained from abdominal aortic aneurysms. Acta Biomater. 2006 Sep;2(5):515–20.

28. Parr A, Mclaughlin S, Mclaughlin M, MChir JG. Aortic calcification and abdominal aortic aneurysm expansion. Atherosclerosis. 2009 Feb;202(2):350.

29. Blankensteijn JD, de Jong SECA, Prinssen M, van der Ham AC, Buth J, van Sterkenburg SMM, et al. Two-year outcomes after conventional or endovascular repair of abdominal aortic aneurysms. N Engl J Med. 2005 Jun 9;352(23):2398–405.

30. Franks SC, Sutton AJ, Bown MJ, Sayers RD. Systematic review and meta-analysis of 12 years of endovascular abdominal aortic aneurysm repair. Eur J Vasc Endovasc Surg. 2007 Feb;33(2):154–71.

31. Stroupe KT, Lederle FA, Matsumura JS, Kyriakides TC, Jonk YC, Ge L, et al. Cost-effectiveness of open versus endovascular repair of abdominal aortic aneurysm in the OVER trial. J Vasc Surg. 2012 Oct;56(4):901-909.e2.

32. Lederle FA, Freischlag JA, Kyriakides TC, Matsumura JS, Padberg FT, Kohler TR, et al. Long-term comparison of endovascular and open repair of abdominal aortic aneurysm. N Engl J Med. 2012 Nov 22;367(21):1988–97.

33. Vogel TR, Symons RG, Flum DR. Longitudinal outcomes after endovascular repair of abdominal aortic aneurysms. Vasc Endovascular Surg. 2008 Nov;42(5):412–9.

34. Becquemin J-P. The ACE trial: a randomized comparison of open versus endovascular repair in good risk patients with abdominal aortic aneurysm. J Vasc Surg. 2009 Jul;50(1):222–4; discussion 224.

35. De Bruin JL, Baas AF, Buth J, Prinssen M, Verhoeven ELG, Cuypers PWM, et al. Long-term outcome of open or endovascular repair of abdominal aortic aneurysm. N Engl J Med. 2010 May 20;362(20):1881–9.

36. Greenhalgh RM, Brown LC, Powel JT, Thompson SG, Epstein D, Sculpher MJ. Endovascular versus open repair of abdominal aortic aneurysm. N Engl J Med. 2010 May 20;362(20):1863–71.

37. Stather PW, Sidloff D, Dattani N, Choke E, Bown MJ, Sayers RD. Systematic review and meta-analysis of the early and late outcomes of open and endovascular repair of abdominal aortic aneurysm. Br J Surg. 2013 Jun;100(7):863–72.

38. Eliason JL, Clouse WD. Current management of infrarenal abdominal aortic aneurysms. Surg Clin North Am. 2007 Oct;87(5):1017–33, viii.

39. Eliason JL, Upchurch GR. Endovascular treatment of aortic aneurysms: state of the art. Curr Treat Options Cardiovasc Med. 2009 Apr;11(2):136–45.

40. Becquemin J-P, Pillet J-C, Lescalie F, Sapoval M, Goueffic Y, Lermusiaux P, et al. A randomized controlled trial of endovascular aneurysm repair versus open surgery for abdominal aortic aneurysms in low- to moderate-risk patients. J Vasc Surg. 2011 May;53(5):1167-1173.e1.

41. Lederle FA, Stroupe KT, Open Versus Endovascular Repair (OVER) Veterans Affairs Cooperative Study Group. Cost-effectiveness at two years in the VA Open Versus Endovascular Repair Trial. Eur J Vasc Endovasc Surg Off J Eur Soc Vasc Surg. 2012 Dec;44(6):543–8.

42. Chaikof EL, Fillinger MF, Matsumura JS, Rutherford RB, White GH, Blankensteijn JD, et al. Identifying and grading factors that modify the outcome of endovascular aortic aneurysm repair. J Vasc Surg. 2002 May;35(5):1061–6.

43. Vercauteren Sven RW, De Roover D. Preclosure for PEVAR [Internet]. 2014 Mar [cited 2014 Dec 6]. Available from: http://evtoday.com/2014/03/preclosure-for-pevar/

44. Mousa AY, Campbell JE, Broce M, Abu-Halimah S, Stone PA, Hass SM, et al. Predictors of percutaneous access failure requiring open femoral surgical conversion during endovascular aortic aneurysm repair. J Vasc Surg. 2013 Nov;58(5):1213–9.

45. Teh LG, Sieunarine K, van Schie G, Goodman MA, Lawrence-Brown M, Prendergast FJ, et al. Use of the percutaneous vascular surgery device for closure of femoral access sites during endovascular aneurysm repair: lessons from our experience. Eur J Vasc Endovasc Surg Off J Eur Soc Vasc Surg. 2001 Nov;22(5):418–23.

46. Petrik PV, Moore WS. Endoleaks following endovascular repair of abdominal aortic aneurysm: the predictive value of preoperative anatomic factors--a review of 100 cases. J Vasc Surg. 2001 Apr;33(4):739–44.

47. Volodos NL, Shekhanin VE, Karpovich IP, Troian VI, Gur'ev IA. A self-fixing synthetic blood vessel endoprosthesis. Vestn Khir Im I I Grek. 1986 Nov;137(11):123–5.

48. Wain RA, Marin ML, Ohki T, Sanchez LA, Lyon RT, Rozenblit A, et al. Endoleaks after endovascular graft treatment of aortic aneurysms: Classification, risk factors, and outcome. J Vasc Surg. 1998 Jan;27(1):69–80.

49. Wyss TR, Dick F, Brown LC, Greenhalgh RM. The influence of thrombus, calcification, angulation, and tortuosity of attachment sites on the time to the first graft-related complication after endovascular aneurysm repair. J Vasc Surg. 2011 Oct;54(4):965–71.

50. Valenti D, Golzarian J. Endoleak: Definition, Diagnosis, and Management. In: MD JG, MD SS, MD MJS, editors. Vascular Embolotherapy [Internet]. Springer Berlin Heidelberg; 2006 [cited 2014 Dec 6]. p. 235–51. (Medical Radiology).
Available from: http://link.springer.com/chapter/10.1007/3-540-33256-1_19

51. Antoniou GA, Georgiadis GS, Antoniou SA, Kuhan G, Murray D. A meta-analysis of outcomes of endovascular abdominal aortic aneurysm repair in patients with hostile and friendly neck anatomy. J Vasc Surg. 2013 Feb;57(2):527–38.

52. Sampaio SM, Panneton JM, Mozes GI, Andrews JC, Bower TC, Karla M, et al. Proximal Type I endoleak after endovascular abdominal aortic aneurysm repair: predictive factors. Ann Vasc Surg. 2004 Nov;18(6):621–8.

53. Wyss TR, Brown LC, Powell JT, Greenhalgh RM. Rate and predictability of graft rupture after endovascular and open abdominal aortic aneurysm repair: data from the EVAR Trials. Ann Surg. 2010 Nov;252(5):805–12.

54. Blankensteijn JD, Mali WP, Eikelboom BC. The Utrecht endovascular technologies (EVT) experience. J Mal Vasc. 1998 Dec;23(5):381–4.

55. Broeders IA, Blankensteijn JD, Gvakharia A, May J, Bell PR, Swedenborg J, et al. The efficacy of transfemoral endovascular aneurysm management: a study on size changes of the abdominal aorta during mid-term follow-up. Eur J Vasc Endovasc Surg Off J Eur Soc Vasc Surg. 1997 Aug;14(2):84–90.

56. Love M, Wray A, Worthington M, Ellis P. Failure of aneurysm sac shrinkage after endovascular repair; the effect of mural calcification. Clin Radiol. 2005 Dec;60(12):1290–4.

57. Pitton MB, Scheschkowski T, Ring M, Herber S, Oberholzer K, Leicher-Düber A, et al. Ten-year follow-up of endovascular aneurysm treatment with Talent stent-grafts. Cardiovasc Intervent Radiol. 2009 Sep;32(5):906–17.

58. Kwon ST, Burek W, Dupay AC, Farsad M, Baek S, Park E-A, et al. Interaction of expanding abdominal aortic aneurysm with surrounding tissue: Retrospective CT image studies. J Nat Sci. 2015 Aug;1(8):e150.

59. Mohammadi H, Lessard S, Therasse E, Mongrain R, Soulez G. A numerical preoperative planning model to predict arterial deformations in endovascular aortic aneurysm repair. Ann Biomed Eng. 2018 Dec 1;46(12):2148–61.

60. Jones GT. The Pathohistology of Abdominal Aortic Aneurysm. In: diagnosis, screening and treatment of abdominal, thoracoabdominal and thoracic aortic aneurysms. InTech; 2011.

61. Holzapfel GA. Structural and numerical models for the (visco)elastic response of arterial walls with residual stresses. In: Holzapfel GA, Ogden RW, editors. Biomechanics of Soft Tissue in Cardiovascular Systems [Internet]. Springer Vienna; 2003 [cited 2014 Dec 11]. p. 109–84. (International Centre for Mechanical Sciences). Available from: http://link.springer.com/chapter/10.1007/978-3-7091-2736-0_4

62. Roy D, Kauffmann C, Delorme S, Lerouge S, Cloutier G, Soulez G. A literature review of the numerical analysis of abdominal aortic aneurysms treated with endovascular stent grafts. Comput Math Methods Med [Internet]. 2012 [cited 2018 Dec 4];2012. Available from: https://www.ncbi.nlm.nih.gov/pmc/articles/PMC3445816/

63. Harter LP, Gross BH, Callen PW, Barth RA. Ultrasonic evaluation of abdominal aortic thrombus. J Ultrasound Med Off J Am Inst Ultrasound Med. 1982 Oct;1(8):315–8.

64. Achille PD, Tellides G, Figueroa CA, Humphrey JD. A haemodynamic predictor of intraluminal thrombus formation in abdominal aortic aneurysms. Proc R Soc Lond Math Phys Eng Sci. 2014 Dec 8;470(2172):20140163.

65. Wang DHJ, Makaroun M, Webster MW, Vorp DA. Mechanical properties and microstructure of intraluminal thrombus from abdominal aortic aneurysm. J Biomech Eng. 2001 Jun 21;123(6):536–9.

66. Di Martino ES, Guadagni G, Fumero A, Ballerini G, Spirito R, Biglioli P, et al. Fluid-structure interaction within realistic three-dimensional models of the aneurysmatic aorta as a guidance to assess the risk of rupture of the aneurysm. Med Eng Phys. 2001 Nov;23(9):647–55.

67. Li Z-Y, U-King-Im J, Tang TY, Soh E, See TC, Gillard JH. Impact of calcification and intraluminal thrombus on the computed wall stresses of abdominal aortic aneurysm. J Vasc Surg. 2008 May;47(5):928–35.

68. van Dam EA, Dams SD, Peters GWM, Rutten MCM, Schurink GWH, Buth J, et al. Non-linear viscoelastic behavior of abdominal aortic aneurysm thrombus. Biomech Model Mechanobiol. 2008 Apr;7(2):127–37.

69. Schurink GW, van Baalen JM, Visser MJ, van Bockel JH. Thrombus within an aortic aneurysm does not reduce pressure on the aneurysmal wall. J Vasc Surg. 2000 Mar;31(3):501–6.

70. Sander de Putter FN van de V. Local influence of calcifications on the wall mechanics of abdominal aortic aneurysm. 2006;

71. Speelman L, Bohra A, Bosboom EMH, Schurink GWH, van de Vosse FN, Makaorun MS, et al. Effects of wall calcifications in patient-specific wall stress analyses of abdominal aortic aneurysms. J Biomech Eng. 2007 Feb;129(1):105–9.

72. Xenos M, Rambhia SH, Alemu Y, Einav S, Labropoulos N, Tassiopoulos A, et al. Patient-based abdominal aortic aneurysm rupture risk prediction with fluid structure interaction modeling. Ann Biomed Eng. 2010 Nov;38(11):3323–37.

73. Maier A, Gee MW, Reeps C, Eckstein H-H, Wall WA. Impact of calcifications on patient-specific wall stress analysis of abdominal aortic aneurysms. Biomech Model Mechanobiol. 2010 Oct;9(5):511–21.

74. Holzapfel GA, Sommer G, Regitnig P. Anisotropic mechanical properties of tissue components in human atherosclerotic plaques. J Biomech Eng. 2004 Oct;126(5):657–65.

75. Beattie D, Xu C, Vito R, Glagov S, Whang MC. Mechanical analysis of heterogeneous, atherosclerotic human aorta. J Biomech Eng. 1998 Oct;120(5):602–7.

76. Inzoli F, Boschetti F, Zappa M, Longo T, Fumero R. Biomechanical factors in abdominal aortic aneurysm rupture. Eur J Vasc Surg. 1993 Nov;7(6):667–74.

77. Holzapfel GA, Gasser TC, Ogden RW. A new constitutive framework for arterial wall mechanics and a comparative study of material models. J Elast Phys Sci Solids. 2000 Jul 1;61(1):1–48.

78. Schriefl AJ, Zeindlinger G, Pierce DM, Regitnig P, Holzapfel GA. Determination of the layer-specific distributed collagen fibre orientations in human thoracic and abdominal aortas and common iliac arteries. J R Soc Interface. 2011 Dec 14;rsif20110727.

79. Rahimi SA, Rowe VL. Abdominal aortic aneurysm. 2015 Jan 30 [cited 2015 Mar 29]; Available from: http://emedicine.medscape.com/article/1979501-overview#aw2aab6b2b3

80. Brook WH. Vasa vasorum of the abdominal aorta and inferior vena cava of the rat: an india ink injection study. Vasc Endovascular Surg. 1978 Nov 1;12(6):385–91.

81. Scotland RS, Vallance PJ, Ahluwalia A. Endogenous factors involved in regulation of tone of arterial vasa vasorum: implications for conduit vessel physiology. Cardiovasc Res. 2000 Jun;46(3):403–11.

82. Wolinsky H, Glagov S. Nature of species differences in the medial distribution of aortic vasa vasorum in mammals. Circ Res. 1967 Apr;20(4):409–21.

83. Wolinsky H, Glagov S. Comparison of abdominal and thoracic aortic medial structure in mammals. Circ Res. 1969 Dec 1;25(6):677–86.

84. Kumar V, Abbas AK, Aster JC. Robbins and Cotran Pathologic Basis of Disease [Internet]. 9th Edition. ELSEVIER; 2015. 1408 p.
Available from: http://elsevier.ca/product.jsp?isbn=9780323266161

85. Roy D, Holzapfel GA, Kauffmann C, Soulez G. Finite element analysis of abdominal aortic aneurysms: geometrical and structural reconstruction with application of an anisotropic material model. IMA J Appl Math. 2014 Oct 1;79(5):1011–26.

86. Lederle FA, Johnson GR, Wilson SE, Chute EP, Littooy FN, Bandyk D, et al. Prevalence and associations of abdominal aortic aneurysm detected through screening. Aneurysm Detection and Management (ADAM) Veterans Affairs Cooperative Study Group. Ann Intern Med. 1997 Mar 15;126(6):441–9.

87. Kobeissi E, Hibino M, Pan H, Aune D. Blood pressure, hypertension and the risk of abdominal aortic aneurysms: a systematic review and meta-analysis of cohort studies. Eur J Epidemiol. 2019 Jun;34(6):547–55.

88. Toghill BJ, Saratzis A, Bown MJ. Abdominal aortic aneurysm—an independent disease to atherosclerosis? Cardiovasc Pathol. 2017 Mar 1;27:71–5.

89. Takagi H, Umemoto T. Association of peripheral artery disease with abdominal aortic aneurysm growth. J Vasc Surg. 2016 Aug 1;64(2):506–13.

90. Matsushita K, Kwak L, Ballew SH, Grams ME, Selvin E, Folsom AR, et al. Chronic kidney disease measures and the risk of abdominal aortic aneurysm. Atherosclerosis. 2018 Dec 1;279:107–13.

91. Meijer CA, Kokje VBC, van Tongeren RBM, Hamming JF, van Bockel JH, Möller GM, et al. An association between chronic obstructive pulmonary disease and abdominal aortic aneurysm beyond smoking: results from a case–control study. Eur J Vasc Endovasc Surg. 2012 Aug 1;44(2):153–7.

92. Ailawadi G, Eliason JL, Upchurch GR. Current concepts in the pathogenesis of abdominal aortic aneurysm. J Vasc Surg. 2003 Sep;38(3):584–8.

93. van Oijen C, van de Vosse FN, Baaijens FPT. Mechanics and design of fiber-reinforced vascuolar prostheses [Internet]. Technische Universiteit Eindhoven; 2003 [cited 2014 Dec 11]. Available from: http://purl.tue.nl/590739068707428.pdf

94. Roy D, Kauffmann C, Delorme S, Lerouge S, Cloutier G, Soulez G. A literature review of the numerical analysis of abdominal aortic aneurysms treated with endovascular stent grafts. Comput Math Methods Med [Internet]. 2012 [cited 2019 Feb 27];2012. Available from: https://www.ncbi.nlm.nih.gov/pmc/articles/PMC3445816/

95. Wassef M, Baxter BT, Chisholm RL, Dalman RL, Fillinger MF, Heinecke J, et al. Pathogenesis of abdominal aortic aneurysms: A multidisciplinary research program supported by the National Heart, Lung, and Blood Institute. J Vasc Surg. 2001 Oct;34(4):730–8.

96. Sayers RD. Aortic aneurysms, inflammatory pathways and nitric oxide. Ann R Coll Surg Engl. 2002 Jul;84(4):239–46.

97. Lizarbe TR, Tarín C, Gómez M, Lavin B, Aracil E, Orte LM, et al. Nitric oxide induces the progression of abdominal aortic aneurysms through the matrix metalloproteinase inducer EMMPRIN. Am J Pathol. 2009 Oct;175(4):1421–30.

98. Johanning JM, Armstrong PJ, Franklin DP, Han DC, Carey DJ, Elmore JR. Nitric oxide in experimental aneurysm formation: early events and consequences of nitric oxide inhibition. Ann Vasc Surg. 2002 Jan;16(1):65–72.

99. Miller FJ, Sharp WJ, Fang X, Oberley LW, Oberley TD, Weintraub NL. Oxidative stress in human abdominal aortic aneurysms: a potential mediator of aneurysmal remodeling. Arterioscler Thromb Vasc Biol. 2002 Apr 1;22(4):560–5.

100. Miller FJ. Aortic aneurysms. Arterioscler Thromb Vasc Biol. 2002 Dec 1;22(12):1948–9.

101. Moore JE, Ku DN, Zarins CK, Glagov S. Pulsatile flow visualization in the abdominal aorta under differing physiologic conditions: implications for increased susceptibility to atherosclerosis. J Biomech Eng. 1992 Aug;114(3):391–7.

102. Hsieh H-J, Liu C-A, Huang B, Tseng AH, Wang DL. Shear-induced endothelial mechanotransduction: the interplay between reactive oxygen species (ROS) and nitric oxide (NO) and the pathophysiological implications. J Biomed Sci. 2014 Jan 13;21(1):3.

103. Michel J-B, Martin-Ventura J-L, Egido J, Sakalihasan N, Treska V, Lindholt J, et al. Novel aspects of the pathogenesis of aneurysms of the abdominal aorta in humans. Cardiovasc Res. 2011 Apr 1;90(1):18–27.

104. Adolph R, Vorp DA, Steed DL, Webster MW, Kameneva MV, Watkins SC. Cellular content and permeability of intraluminal thrombus in abdominal aortic aneurysm. J Vasc Surg. 1997 May 1;25(5):916–26.

105. Liu O, Jia L, Liu X, Wang Y, Wang X, Qin Y, et al. Clopidogrel, a platelet P2Y12 receptor inhibitor, reduces vascular inflammation and angiotensin II induced-abdominal aortic aneurysm progression. PloS One. 2012;7(12):e51707.

106. Vorp DA, Lee PC, Wang DH, Makaroun MS, Nemoto EM, Ogawa S, et al. Association of intraluminal thrombus in abdominal aortic aneurysm with local hypoxia and wall weakening. J Vasc Surg. 2001 Aug;34(2):291–9.

107. Jayalath RW, Mangan SH, Golledge J. Aortic calcification. Eur J Vasc Endovasc Surg. 2005 Nov;30(5):476–88.

108. Kim E-D, Kim JS, Kim S-S, Jung J-G, Yun S-J, Kim J-Y, et al. Association of abdominal aortic calcification with lifestyle and risk factors of cardiovascular disease. Korean J Fam Med. 2013 May;34(3):213–20.

109. Figueiredo CP, Rajamannan NM, Lopes JB, Caparbo VF, Takayama L, Kuroishi ME, et al. Serum phosphate and hip bone mineral density as additional factors for high vascular calcification scores in a community-dwelling: the São Paulo Ageing & Health Study (SPAH). Bone. 2013 Jan;52(1):354–9.

110. Alrasadi K, Alwaili K, Awan Z, Valenti D, Couture P, Genest J. Aortic calcifications in familial hypercholesterolemia: potential role of the low-density lipoprotein receptor gene. Am Heart J. 2009 Jan;157(1):170–6.

111. Rutsch F, MacDougall M, Lu C, Buers I, Mamaeva O, Nitschke Y, et al. A specific IFIH1 gain-of-function mutation causes Singleton-Merten syndrome. Am J Hum Genet. 2015 Feb 5;96(2):275–82.

112. Szulc P. Abdominal aortic calcification: A reappraisal of epidemiological and pathophysiological data. Bone. 2016 Mar 1;84:25–37.

113. New SEP, Aikawa E. Role of extracellular vesicles in de novo mineralization an additional novel mechanism of cardiovascular calcification. Arterioscler Thromb Vasc Biol. 2013 Aug 1;33(8):1753–8.

114. Thompson B, Towler DA. Arterial calcification and bone physiology: role of the bone–vascular axis. Nat Rev Endocrinol. 2012 Sep;8(9):529–43.

115. Lei Y, Sinha A, Nosoudi N, Grover A, Vyavahare N. Hydroxyapatite and calcified elastin induce osteoblast-like differentiation in rat aortic smooth muscle cells. Exp Cell Res. 2014 Apr 15;323(1):198–208.

116. Sinha A, Vyavahare NR. High-glucose levels and elastin degradation products accelerate osteogenesis in vascular smooth muscle cells: Diab Vasc Dis Res [Internet]. 2013 Jun 10 [cited 2020 Apr 8];
Available from: https://journals.sagepub.com/doi/10.1177/1479164113485101

117. Hruska Keith A., Mathew Suresh, Saab Georges. Bone morphogenetic proteins in vascular calcification. Circ Res. 2005 Jul 22;97(2):105–14.

118. Lau WL, Festing MH, Giachelli CM. Phosphate and vascular calcification: emerging role of the sodium-dependent phosphate co-transporter PiT-1. Thromb Haemost. 2010;104(09):464–70.

119. Cola C, Almeida M, Li D, Romeo F, Mehta JL. Regulatory role of endothelium in the expression of genes affecting arterial calcification. Biochem Biophys Res Commun. 2004 Jul 23;320(2):424–7.

120. Rattazzi M, Faggin E, Buso R, Di Virgilio R, Puato M, Plebani M, et al. Atorvastatin reduces circulating osteoprogenitor cells and t-cell rankl expression in osteoporotic women: implications for the bone-vascular axis. Cardiovasc Ther. 2016 Feb;34(1):13–20.

121. Fadini Gian Paolo, Albiero Mattia, Menegazzo Lisa, Boscaro Elisa, Vigili de Kreutzenberg Saula, Agostini Carlo, et al. Widespread increase in myeloid calcifying cells contributes to ectopic vascular calcification in Type 2 diabetes. Circ Res. 2011 Apr 29;108(9):1112–21.

122. Eghbali-Fatourechi GZ, Lamsam J, Fraser D, Nagel D, Riggs BL, Khosla S. Circulating osteoblast-lineage cells in humans. N Engl J Med. 2005 May 12;352(19):1959–66.

123. Pikilidou M, Yavropoulou M, Antoniou M, Yovos J. The contribution of osteoprogenitor cells to arterial stiffness and hypertension. J Vasc Res. 2015;52(1):32–40.

124. Vasuri F, Fittipaldi S, Pasquinelli G. Arterial calcification: Finger-pointing at resident and circulating stem cells. World J Stem Cells. 2014 Nov 26;6(5):540–51.

125. Gössl M, Mödder UI, Atkinson EJ, Lerman A, Khosla S. Osteocalcin expression by circulating endothelial progenitor cells in patients with coronary atherosclerosis. J Am Coll Cardiol. 2008 Oct 14;52(16):1314–25.

126. Pal SN, Rush C, Parr A, Van Campenhout A, Golledge J. Osteocalcin positive mononuclear cells are associated with the severity of aortic calcification. Atherosclerosis. 2010 May;210(1):88–93.

127. Pal SN, Clancy P, Golledge J. Circulating concentrations of stem-cell-mobilizing cytokines are associated with levels of osteoprogenitor cells and aortic calcification severity. Circ J Off J Jpn Circ Soc. 2011;75(5):1227–34.

128. Otsuru S, Tamai K, Yamazaki T, Yoshikawa H, Kaneda Y. Bone marrow-derived osteoblast progenitor cells in circulating blood contribute to ectopic bone formation in mice. Biochem Biophys Res Commun. 2007 Mar 9;354(2):453–8.

129. Pignolo RJ, Kassem M. Circulating osteogenic cells: implications for injury, repair, and regeneration. J Bone Miner Res Off J Am Soc Bone Miner Res. 2011 Aug;26(8):1685–93.

130. Thanassoulis G, Massaro JM, Corsini E, Rogers I, Schlett CL, Meigs JB, et al. Periaortic adipose tissue and aortic dimensions in the Framingham Heart Study. J Am Heart Assoc. 2012 Dec;1(6):e000885.

131. Gil-Ortega M, Somoza B, Huang Y, Gollasch M, Fernández-Alfonso MS. Regional differences in perivascular adipose tissue impacting vascular homeostasis. Trends Endocrinol Metab. 2015 Jul 1;26(7):367–75.

132. Fitzgibbons TP, Kogan S, Aouadi M, Hendricks GM, Straubhaar J, Czech MP. Similarity of mouse perivascular and brown adipose tissues and their resistance to diet-induced inflammation. Am J Physiol - Heart Circ Physiol. 2011 Oct;301(4):H1425–37.

133. Padilla J, Jenkins NT, Vieira-Potter VJ, Laughlin MH. Divergent phenotype of rat thoracic and abdominal perivascular adipose tissues. Am J Physiol Regul Integr Comp Physiol. 2013 Apr 1;304(7):R543-552.

134. Horimatsu T, Kim HW, Weintraub NL. The Role of Perivascular Adipose Tissue in Non-atherosclerotic Vascular Disease. Front Physiol [Internet]. 2017 [cited 2019 Aug 3];8. Available from: https://www.frontiersin.org/articles/10.3389/fphys.2017.00969/full#B78

135. Szasz T, Clinton Webb R. Perivascular adipose tissue: more than just structural support. Clin Sci Lond Engl 1979. 2012 Jan;122(1):1–12.

136. Folkesson M, Vorkapic E, Gulbins E, Japtok L, Kleuser B, Welander M, et al. Inflammatory cells, ceramides, and expression of proteases in perivascular adipose tissue adjacent to human abdominal aortic aneurysms. J Vasc Surg. 2017 Apr 1;65(4):1171-1179.e1.

137. Police Sara B., Thatcher Sean E., Charnigo Richard, Daugherty Alan, Cassis Lisa A. Obesity promotes inflammation in periaortic adipose tissue and angiotensin ii-induced abdominal aortic aneurysm formation. Arterioscler Thromb Vasc Biol. 2009 Oct 1;29(10):1458–64.

138. Sano M, Sasaki T, Hirakawa S, Sakabe J, Ogawa M, Baba S, et al. Lymphangiogenesis and angiogenesis in abdominal aortic aneurysm. PLOS ONE. 2014 Mar 20;9(3):e89830.

139. Villacorta L, Chang L. The role of perivascular adipose tissue in vasoconstriction, arterial stiffness, and aneurysm. Horm Mol Biol Clin Investig. 2015 Feb;21(2):137–47.

140. Beck AW, Goodney PP, Nolan BW, Likosky DS, Eldrup-Jorgensen J, Cronenwett JL. Predicting 1-year mortality after elective abdominal aortic aneurysm repair. J Vasc Surg. 2009 Apr 1;49(4):838–44.

141. Greenhalgh RM, Brown LC, Powell JT, Thompson SG, Epstein D, Sculpher MJ. Endovascular versus open repair of abdominal aortic aneurysm. N Engl J Med. 2010 May 20;362(20):1863–71.

142. Acosta S, Lindblad B, Zdanowski Z. Predictors for outcome after open and endovascular repair of ruptured abdominal aortic aneurysms. Eur J Vasc Endovasc Surg. 2007 Mar 1;33(3):277–84.

143. Schermerhorn ML, Buck DB, O'Malley AJ, Curran T, McCallum JC, Darling J, et al. Long-term outcomes of abdominal aortic aneurysm in the medicare population. N Engl J Med. 2015 Jul 23;373(4):328–38.

144. Arnaoutakis DJ, Zammert M, Karthikesalingam A, Belkin M. Endovascular repair of abdominal aortic aneurysms. Best Pract Res Clin Anaesthesiol. 2016 Sep 1;30(3):331–40.

145. Herman CR, Charbonneau P, Hongku K, Dubois L, Hossain S, Lee K, et al. Any nonadherence to instructions for use predicts graft-related adverse events in patients undergoing elective endovascular aneurysm repair. J Vasc Surg. 2018 Jan 1;67(1):126–33.

146. Kansagra K, Kang J, Taon M-C, Ganguli S, Gandhi R, Vatakencherry G, et al. Advanced endografting techniques: snorkels, chimneys, periscopes, fenestrations, and branched endografts. Cardiovasc Diagn Ther. 2018 Apr;8(Suppl 1):S175–83.

147. Carpenter JP, Cuff R, Buckley C, Healey C, Hussain S, Reijnen MMPJ, et al. One-year pivotal trial outcomes of the Nellix system for endovascular aneurysm sealing. J Vasc Surg. 2017 Feb 1;65(2):330-336.e4.

148. Galiñanes EL, Hernandez E, Krajcer Z. Preliminary results of adjunctive use of endoanchors in the treatment of short neck and pararenal abdominal aortic aneurysms. Catheter Cardiovasc Interv. 2016 Mar 1;87(4):E154–9.

149. Daye D, Walker TG. Complications of endovascular aneurysm repair of the thoracic and abdominal aorta: evaluation and management. Cardiovasc Diagn Ther. 2018 Apr;8(Suppl 1):S138–56.

150. Chaikof EL, Dalman RL, Eskandari MK, Jackson BM, Lee WA, Mansour MA, et al. The Society for Vascular Surgery practice guidelines on the care of patients with an abdominal aortic aneurysm. J Vasc Surg. 2018 Jan 1;67(1):2-77.e2.

151. Reis PEO, Rotolo M, Aless, Veiga ra V, Netto JM, Maia VN, et al. Total abdominal aortic stent graft occlusion. J Vasc Endovasc Ther [Internet]. 2017 Dec 30 [cited 2020 Apr 11];2. Available from: https://vascular-endovascular-therapy.imedpub.com/abstract/total-abdominal-aortic-stent-graft-occlusion-21501.html

152. Mantas GK, Antonopoulos CN, Sfyroeras GS, Moulakakis KG, Kakisis JD, Mylonas SN, et al. Factors predisposing to endograft limb occlusion after endovascular aortic repair. Eur J Vasc Endovasc Surg Off J Eur Soc Vasc Surg. 2015 Jan;49(1):39–44.

153. Wang G, Zhai S, Li T, Li X, Lu D, Wang B, et al. Limb graft occlusion following endovascular aortic repair: Incidence, causes, treatment and prevention in a study cohort. Exp Ther Med. 2017 Aug;14(2):1763–8.

154. Bryce Y, Rogoff P, Romanelli D, Reichle R. Endovascular repair of abdominal aortic aneurysms: vascular anatomy, device selection, procedure, and procedure-specific complications. Radiogr Rev Publ Radiol Soc N Am Inc. 2015 Apr;35(2):593–615.

155. Vad S, Eskinazi A, Corbett T, McGloughlin T, Vande Geest JP. Determination of coefficient of friction for self-expanding stent-grafts. J Biomech Eng. 2010 Dec;132(12):121007.

156. Raghavan ML, Webster MW, Vorp DA. Ex vivo biomechanical behavior of abdominal aortic aneurysm: Assessment using a new mathematical model. Ann Biomed Eng. 1996 Sep 1;24(5):573–82.

157. Thubrikar MJ, Labrosse M, Robicsek F, Al-Soudi J, Fowler B. Mechanical properties of abdominal aortic aneurysm wall. J Med Eng Technol. 2001 Jan 1;25(4):133–42.

158. Vande Geest JP, Sacks MS, Vorp DA. The effects of aneurysm on the biaxial mechanical behavior of human abdominal aorta. J Biomech. 2006;39(7):1324–34.

159. Raghavan ML, Vorp DA. Toward a biomechanical tool to evaluate rupture potential of abdominal aortic aneurysm: identification of a finite strain constitutive model and evaluation of its applicability. J Biomech. 2000 Apr;33(4):475–82.

160. Raghavan ML, Fillinger MF, Marra SP, Naegelein BP, Kennedy FE. Automated methodology for determination of stress distribution in human abdominal aortic aneurysm. J Biomech Eng. 2005 Oct;127(5):868–71.

161. Raghavan ML, Vorp DA, Federle MP, Makaroun MS, Webster MW. Wall stress distribution on three-dimensionally reconstructed models of human abdominal aortic aneurysm. J Vasc Surg. 2000 Apr;31(4):760–9.

162. Fillinger MF, Raghavan ML, Marra SP, Cronenwett JL, Kennedy FE. In vivo analysis of mechanical wall stress and abdominal aortic aneurysm rupture risk. J Vasc Surg. 2002 Sep;36(3):589–97.

163. O′Leary SA, Kavanagh EG, Grace PA, McGloughlin TM, Doyle BJ. The biaxial mechanical behaviour of abdominal aortic aneurysm intraluminal thrombus: Classification of morphology and the determination of layer and region specific properties. J Biomech. 2014 Apr 11;47(6):1430–7.

164. Wang DHJ, Makaroun MS, Webster MW, Vorp DA. Effect of intraluminal thrombus on wall stress in patient-specific models of abdominal aortic aneurysm. J Vasc Surg. 2002 Sep;36(3):598–604.

165. Gasser TC, Görgülü G, Folkesson M, Swedenborg J. Failure properties of intraluminal thrombus in abdominal aortic aneurysm under static and pulsating mechanical loads. J Vasc Surg. 2008 Jul 1;48(1):179–88.

166. Haller SJ, Crawford JD, Courchaine KM, Bohannan CJ, Landry GJ, Moneta GL, et al. Intraluminal thrombus is associated with early rupture of abdominal aortic aneurysm. J Vasc Surg. 2018;67(4):1051-1058.e1.

167. Agatston AS, Janowitz WR, Hildner FJ, Zusmer NR, Viamonte M, Detrano R. Quantification of coronary artery calcium using ultrafast computed tomography. J Am Coll Cardiol. 1990 Mar 15;15(4):827–32.

168. Golestani R, Tio RA, Zeebregts CJ, Zeilstra A, Dierckx RA, Boersma HH, et al. Abdominal aortic calcification detected by dual X-ray absorptiometry: A strong predictor for cardiovascular events. Ann Med. 2010 Oct 1;42(7):539–45.

169. Nakayama A, Morita H, Hayashi N, Nomura Y, Hoshina K, Shigematsu K, et al. Inverse correlation between calcium accumulation and the expansion rate of abdominal aortic aneurysms. Circ J Off J Jpn Circ Soc. 2016;80(2):332–9.

170. Kurugol S, Come CE, Diaz AA, Ross JC, Kinney GL, Black-Shinn JL, et al. Automated quantitative 3D analysis of aorta size, morphology, and mural calcification distributions. Med Phys. 2015 Sep;42(9):5467–78.

171. Chowdhury MM, Zieliński LP, Sun JJ, Lambracos S, Boyle JR, Harrison SC, et al. Editor's Choice – Calcification of thoracic and abdominal aneurysms is associated with mortality and morbidity. Eur J Vasc Endovasc Surg. 2018 Jan;55(1):101–8.

172. Buijs RVC, Leemans EL, Greuter M, Tielliu IFJ, Zeebregts CJ, Willems TP. Quantification of abdominal aortic calcification: Inherent measurement errors in current computed tomography imaging. PLoS ONE [Internet]. 2018 Feb 28 [cited 2019 Jul 31];13(2). Available from: https://www.ncbi.nlm.nih.gov/pmc/articles/PMC5831389/

173. Komen N, Klitsie P, Hermans JJ, Niessen WJ, Kleinrensink GJ, Jeekel J, et al. Calcium scoring in unenhanced and enhanced CT data of the aorta-iliacal arteries: impact of image acquisition, reconstruction, and analysis parameter settings. Acta Radiol Stockh Swed 1987. 2011 Nov 1;52(9):943–50.

174. Weert TT de, Cakir H, Rozie S, Cretier S, Meijering E, Dippel DWJ, et al. Intracranial internal carotid artery calcifications: association with vascular risk factors and ischemic cerebrovascular disease. Am J Neuroradiol. 2009 Jan 1;30(1):177–84.

175. Schousboe JT, Wilson KE, Kiel DP. Detection of abdominal aortic calcification with lateral spine imaging using DXA. J Clin Densitom. 2006 Jul 1;9(3):302–8.

176. Schousboe JT, Taylor BC, Kiel DP, Ensrud KE, Wilson KE, McCloskey EV. Abdominal aortic calcification detected on lateral spine images from a bone densitometer predicts incident myocardial infarction or stroke in older women. J Bone Miner Res. 2008;23(3):409–16.

177. Kauppila LI, Polak JF, Cupples LA, Hannan MT, Kiel DP, Wilson PWF. New indices to classify location, severity and progression of calcific lesions in the abdominal aorta: a 25-year follow-up study. Atherosclerosis. 1997 Jul 25;132(2):245–50.

178. Friedlander AH, El Saden SM, Hazboun RC, Chang TI, Wong WK, Garrett NR. Detection of carotid artery calcification on the panoramic images of post-menopausal females is significantly associated with severe abdominal aortic calcification: a risk indicator of future adverse vascular events. Dentomaxillofacial Radiol [Internet]. 2015 Sep [cited 2020 Apr 12];44(7). Available from: https://www.ncbi.nlm.nih.gov/pmc/articles/PMC4628414/

179. Kiel DP, Kauppila LI, Cupples LA, Hannan MT, O'Donnell CJ, Wilson PWF. Bone loss and the progression of abdominal aortic calcification over a 25 year period: The Framingham heart study. Calcif Tissue Int. 2001 May 1;68(5):271–6.

180. Buijs RVC, Willems TP, Tio RA, Boersma HH, Tielliu IFJ, Slart RHJA, et al. Calcification as a risk factor for rupture of abdominal aortic aneurysm. Eur J Vasc Endovasc Surg. 2013 Nov 1;46(5):542–8.

181. Filis KA, Arko FR, Rubin GD, Zarins CK. Three-dimensional CT evaluation for endovascular abdominal aortic aneurysm repair. Quantitative assessment of the infrarenal aortic neck. Acta Chir Belg. 2003 Feb;103(1):81–6.

182. Balm R, Stokking R, Kaatee R, Blankensteijn JD, Eikelboom BC, van Leeuwen MS. Computed tomographic angiographic imaging of abdominal aortic aneurysms: Implications for transfemoral endovascular aneurysm management. J Vasc Surg. 1997 Aug;26(2):231–7.

183. Zarins CK, Bloch DA, Crabtree T, Matsumoto AH, White RA, Fogarty TJ. Stent graft migration after endovascular aneurysm repair: importance of proximal fixation. J Vasc Surg. 2003 Dec;38(6):1264–72; discussion 1272.

184. Raut SS, Chandra S, Shum J, Finol EA. The role of geometric and biomechanical factors in abdominal aortic aneurysm rupture risk assessment. Ann Biomed Eng. 2013 Jul 1;41(7):1459–77.

185. Farotto D, Segers P, Meuris B, Vander Sloten J, Famaey N. The role of biomechanics in aortic aneurysm management: requirements, open problems and future prospects. J Mech Behav Biomed Mater. 2018 Jan 1;77:295–307.

186. Domagala Z, Stepak H, Drapikowski P, Dzieciuchowicz L, Pyda M, Karmelita-Katulska K, et al. Biomechanical factors in Finite Element Analysis of abdominal aortic aneurysms. Acta Angiol. 2016;22(4):164–71.

187. Huang H, Virmani R, Younis H, Burke AP, Kamm RD, Lee RT. The impact of calcification on the biomechanical stability of atherosclerotic plaques. Circulation. 2001 Feb 27;103(8):1051–6.

188. Williamson SD, Lam Y, Younis HF, Huang H, Patel S, Kaazempur-Mofrad MR, et al. On the sensitivity of wall stresses in diseased arteries to variable material properties. J Biomech Eng. 2003 Feb;125(1):147–55.

189. Loree HM, Tobias BJ, Gibson LJ, Kamm RD, Small DM, Lee RT. Mechanical properties of model atherosclerotic lesion lipid pools. Arterioscler Thromb J Vasc Biol Am Heart Assoc. 1994 Feb;14(2):230–4.

190. O'Leary SA, Mulvihill JJ, Barrett HE, Kavanagh EG, Walsh MT, McGloughlin TM, et al. Determining the influence of calcification on the failure properties of abdominal aortic aneurysm (AAA) tissue. J Mech Behav Biomed Mater. 2015 Feb 1;42:154–67.

191. Barrett HE, Cunnane EM, Hidayat H, O'Brien JM, Moloney MA, Kavanagh EG, et al. On the influence of wall calcification and intraluminal thrombus on prediction of abdominal aortic aneurysm rupture. J Vasc Surg. 2018;67(4):1234-1246.e2.

192. Sommer G, Eder M, Kovacs L, Pathak H, Bonitz L, Mueller C, et al. Multiaxial mechanical properties and constitutive modeling of human adipose tissue: A basis for preoperative simulations in plastic and reconstructive surgery. Acta Biomater. 2013 Nov 1;9(11):9036–48.

193. Kim J, Peruski B, Hunley C, Kwon S, Baek S. Influence of surrounding tissues on biomechanics of aortic wall. Int J Exp Comput Biomech. 2013 Sep;2(2):105–17.

194. Lalka SG, Stockberger SM, Johnson MS, Hawes D, Aisen A, Trerotola SO. Phantom for Calibration of Preoperative Imaging Modalities in Endoluminal Stent-Graft Repair of Aortic Aneurysms. J Vasc Interv Radiol. 1998 Sep 1;9(5):799–807.

195. Sulaiman A, Boussel L, Taconnet F, Serfaty JM, Alsaid H, Attia C, et al. In vitro non-rigid life-size model of aortic arch aneurysm for endovascular prosthesis assessment. Eur J Cardiothorac Surg. 2008 Jan 1;33(1):53–7.

196. Russ C, Gessat M, Falk V, Szekely G. Rapid prototyping of silicone-based phantom models for stent simulation validation. In: 15th International Conference on Medical Image Computing and Computer Assisted Intervention (MICCAI), Nice, 1 October 2012 - 5 October 2012 [Internet]. Nice: University of Zurich; 2012 [cited 2019 Aug 13]. Available from: https://www.zora.uzh.ch/id/eprint/72940/

197. Paramasivam S, Baltsavias G, Psatha E, Matis G, Valavanis A. Silicone models as basic training and research aid in endovascular neurointervention—a single-center experience and review of the literature. Neurosurg Rev. 2014 Apr 1;37(2):331–7.

198. Wang Y, Joannic D, Juillion P, Monnet A, Delassus P, Lalande A, et al. Validation of the strain assessment of a phantom of abdominal aortic aneurysm: comparison of results obtained from magnetic resonance imaging and stereovision measurements. J Biomech Eng. 2018 Jan 17;140(3):031001-031001–9.

199. Allard L, Soulez G, Chayer B, Qin Z, Roy D, Cloutier G. A multimodality vascular imaging phantom of an abdominal aortic aneurysm with a visible thrombus. Med Phys. 2013 Jun 1;40(6Part1):063701.

200. Kung EO, Les AS, Medina F, Wicker RB, McConnell MV, Taylor CA. In vitro validation of finite element model of AAA hemodynamics incorporating realistic outlet boundary conditions. J Biomech Eng. 2011 Apr;133(4):041003.

201. Cloonan AJ, Shahmirzadi D, Li RX, Doyle BJ, Konofagou EE, McGloughlin TM. 3D-printed tissue-mimicking phantoms for medical imaging and computational validation applications. 3d Print Addit Manuf. 2014 Mar 1;1(1):14–23.

202. Biglino G, Verschueren P, Zegels R, Taylor AM, Schievano S. Rapid prototyping compliant arterial phantoms for in-vitro studies and device testing. J Cardiovasc Magn Reson. 2013 Jan 16;15(1):2.

203. Meess KM, Izzo RL, Dryjski ML, Curl RE, Harris LM, Springer M, et al. 3D printed abdominal aortic aneurysm phantom for image guided surgical planning with a patient specific fenestrated endovascular graft system. Proc SPIE-- Int Soc Opt Eng [Internet]. 2017 Feb 11 [cited 2018 Dec 3];10138.
Available from: https://www.ncbi.nlm.nih.gov/pmc/articles/PMC5476205/

204. Polanczyk A, Podgorski M, Polanczyk M, Piechota-Polanczyk A, Neumayer C, Stefanczyk L. A novel patient-specific human cardiovascular system phantom (HCSP) for reconstructions of pulsatile blood hemodynamic inside abdominal aortic aneurysm. IEEE Access. 2018;6:61896–903.

205. Filippou V, Tsoumpas C. Recent advances on the development of phantoms using 3D printing for imaging with CT, MRI, PET, SPECT, and ultrasound. Med Phys. 2018;45(9):e740–60.

206. Takashima K, Shimomura R, Kitou T, Terada H, Yoshinaka K, Ikeuchi K. Contact and friction between catheter and blood vessel. Tribol Int. 2007 Feb 1;40(2):319–28.

207. Ohta M, Handa A, Iwata H, Rüfenacht DA, Tsutsumi S. Poly-vinyl alcohol hydrogel vascular models for in vitro aneurysm simulations: the key to low friction surfaces. Technol Health Care. 2004 Jan 1;12(3):225–33.

208. Ashton Acton Q. Polyethylene Glycols—Advances in Research and Application. 2013th ed. ScholarlyEditions; 2013. 529 p.

209. Watase M, Nishinari K, Nambu M. Anomalous increase of the elastic modulus of frozen poly(vinyl alcohol) gels. CryoLetters. 1983;4:197–200.

210. Watase M, Nishinari K. Rheological and DSC changes in poly(vinyl alcohol) gels induced by immersion in water. J Polym Sci Polym Phys Ed. 1985;23(9):1803–11.

211. Watase M, Nishinari K. Large deformation of hydrogels of poly(vinyl alcohol), agarose and kappa-carrageenan. Makromol Chem. 1985;186(5):1081–6.

212. Watase M, Nishinari K. Effect of the degree of saponification on the rheological and thermal properties of poly(vinyl alcohol) gels. Makromol Chem. 1989;190(1):155–63.

213. Peppas NA, Stauffer SR. Reinforced uncrosslinked poly (vinyl alcohol) gels produced by cyclic freezing-thawing processes: a short review. J Controlled Release. 1991 Aug;16(3):305–10.

214. Watase M, Nishinari K. Thermal and rheological properties of poly(vinyl alcohol) hydrogels prepared by repeated cycles of freezing and thawing. Makromol Chem. 1988;189(4):871–80.

215. Ku DN, Braddon LG, Wootton DM. Poly(vinyl alcohol) cryogel [Internet]. US5981826 A, 1999 [cited 2014 Dec 12]. Available from: http://www.google.com/patents/US5981826

216. Stauffer SR, Peppast NA. Poly(vinyl alcohol) hydrogels prepared by freezing-thawing cyclic processing. Polymer. 1992 Sep;33(18):3932–6.

217. Lozinsky VI, Damshkaln LG. Study of cryostructuration of polymer systems. XVII. Poly(vinyl alcohol) cryogels: Dynamics of the cryotropic gel formation. J Appl Polym Sci. 2000;77(9):2017–23.

218. Wan WK, Campbell G, Zhang ZF, Hui AJ, Boughner DR. Optimizing the tensile properties of polyvinyl alcohol hydrogel for the construction of a bioprosthetic heart valve stent. J Biomed Mater Res. 2002;63(6):854–61.

219. Pazos V, Mongrain R, Tardif JC. Polyvinyl alcohol cryogel: optimizing the parameters of cryogenic treatment using hyperelastic models. J Mech Behav Biomed Mater. 2009 Oct;2(5):542–9.

220. Pazos V, Mongrain R, Tardif JC. Deformable mock stenotic artery with a lipid pool. J Biomech Eng. 2010 Mar;132(3):034501.

221. Pazos V, Mongrain R, Tardif J-C. Mechanical characterization of atherosclerotic arteries using finite-element modeling: feasibility study on mock arteries. IEEE Trans Biomed Eng. 2010 Jun;57(6):1520–8.

222. Youssef S. Experimental Analysis of a Mock Atherosclerotic Calcified Coronary Artery [Institut de Génie Biomédical Faculté de Médecine]. Université de Montréal; 2012.

223. Le Floc'h S, Cloutier G, Finet G, Tracqui P, Pettigrew RI, Ohayon J. On the potential of a new IVUS elasticity modulus imaging approach for detecting vulnerable atherosclerotic coronary plaques:in vitrovessel phantom study. Phys Med Biol. 2010 Sep;55(19):5701–5721.

224. Chayer B, Hoven M van den, Cardinal M-HR, Li H, Swillens A, Lopata R, et al. Atherosclerotic carotid bifurcation phantoms with stenotic soft inclusions for ultrasound flow and vessel wall elastography imaging. Phys Med Biol. 2019 May;64(9):095025.

225. Mix DS, Stoner MC, Day SW, Richards MS. Manufacturing abdominal aorta hydrogel tissue-mimicking phantoms for ultrasound elastography validation. JoVE J Vis Exp. 2018 Sep 19;(139):e57984.

226. Cloutier G, Soulez G, Qanadli SD, Teppaz P, Allard L, Qin Z, et al. A multimodality vascular imaging phantom with fiducial markers visible in DSA, CTA, MRA, and ultrasound. Med Phys. 2004 Jun 1;31(6):1424–33.

227. Ge L, Sotiropoulos F. Direction and magnitude of blood flow shear stresses on the leaflets of aortic valves: is there a link with valve calcification? J Biomech Eng [Internet]. 2010 Jan 1 [cited 2020 Apr 14];132(1). Available from: https://asmedigitalcollection.asme.org/biomechanical/article/132/1/014505/456201/Direction-and-Magnitude-of-Blood-Flow-Shear

228. Dua MM, Dalman RL. Hemodynamic influences on abdominal aortic aneurysm disease: application of biomechanics to aneurysm pathophysiology. Vascul Pharmacol. 2010;53(1–2):11–21.

229. Hwang JY. Doppler ultrasonography of the lower extremity arteries: anatomy and scanning guidelines. Ultrasonography. 2017 Apr;36(2):111.

230. Weerakkody Y. Renal arterial resistive index | Radiology Reference Article | Radiopaedia.org [Internet]. Radiopaedia. [cited 2020 Aug 18]. Available from: https://radiopaedia.org/articles/renal-arterial-resistive-index

231. Wasilewski J, Głowacki J, Poloński L. Not at random location of atherosclerotic lesions in thoracic aorta and their prognostic significance in relation to the risk of cardiovascular events. Pol J Radiol. 2013;78(2):38–42.

232. Lu D, Kassab GS. Role of shear stress and stretch in vascular mechanobiology. J R Soc Interface. 2011 Oct 7;8(63):1379–85.

233. Pyke KE, Tschakovsky ME. The relationship between shear stress and flow-mediated dilatation: implications for the assessment of endothelial function. J Physiol. 2005 Oct 15;568(Pt 2):357–69.

234. Papaioannou TG, Stefanadis C. Vascular wall shear stress: basic principles and methods. Hell J Cardiol HJC Hell Kardiologike Epitheorese. 2005 Feb;46(1):9–15.

235. Brassard J-J, Denis J-A, Therasse É, Beaudoin N, Blair J-F, Elkouri S. Fluoroscopy time during evar: can we do better? J Vasc Surg. 2015 Nov 1;62(5):1383.

236. Bryce Y, Schiro B, Cooper K, Ganguli S, Khayat M, Lam C (Ken), et al. Type II endoleaks: diagnosis and treatment algorithm. Cardiovasc Diagn Ther. 2018 Apr;8(Suppl 1):S131–7.

237. Bernad S, Bernad E-S, Barbat T, Brisan C, Albulescu V. An analysis of blood flow dynamics in AAA. Etiol Pathog Pathophysiol Aortic Aneurysms Aneurysm Rupture [Internet]. 2011 Jul 27 [cited 2020 Aug 23]; Available from: https://www.intechopen.com/books/etiology-pathogenesis-and-pathophysiology-of-aortic-aneurysms-and-aneurysm-rupture/an-analysis-of-blood-flow-dynamics-in-aaa

238. Volokh KY, Aboudi J. Aneurysm strength can decrease under calcification. J Mech Behav Biomed Mater. 2016 Apr 1;57:164–74.

239. Robertson AM, Duan X, Maiti S. Role of calcification in aneurysm failure - a case study. In 2017. p. 52–5.

240. Roy D. Mechanical simulation of the endovascular repair of abdominal aortic aneurysms [Internet]. 2015 [cited 2018 Nov 30].
Available from: https://papyrus.bib.umontreal.ca/xmlui/handle/1866/13804

241. Raghavan ML, Kratzberg J, Castro de Tolosa EM, Hanaoka MM, Walker P, da Silva ES. Regional distribution of wall thickness and failure properties of human abdominal aortic aneurysm. J Biomech. 2006 Jan 1;39(16):3010–6.

242. Heng MS, Fagan MJ, Collier JW, Desai G, McCollum PT, Chetter IC. Peak wall stress measurement in elective and acute abdominal aortic aneurysms. J Vasc Surg. 2008 Jan 1;47(1):17–22.

243. Metaxa E, Tzirakis K, Kontopodis N, Ioannou CV, Papaharilaou Y. Correlation of intraluminal thrombus deposition, biomechanics, and hemodynamics with surface growth and rupture in abdominal aortic aneurysm-application in a clinical paradigm. Ann Vasc Surg. 2018 Jan;46:357–66.

244. Disseldorp EMJ van, Petterson NJ, Rutten MCM, Vosse FN van de, Sambeek MRHM van, Lopata RGP. Patient specific wall stress analysis and mechanical characterization of abdominal aortic aneurysms using 4D Ultrasound. Eur J Vasc Endovasc Surg. 2016 Nov 1;52(5):635–42.

245. Martufi G, Satriano A, Moore RD, Vorp DA, Di Martino ES. Local quantification of wall thickness and intraluminal thrombus offer insight into the mechanical properties of the aneurysmal aorta. Ann Biomed Eng. 2015 Aug 1;43(8):1759–71.

246. Hinnen J-W, Koning OHJ, Visser MJT, Van Bockel HJ. Effect of intraluminal thrombus on pressure transmission in the abdominal aortic aneurysm. J Vasc Surg. 2005 Dec 1;42(6):1176–82.

247. Takashima K, Kitou T, Mori K, Ikeuchi K. Simulation and experimental observation of contact conditions between stents and artery models. Med Eng Phys. 2007 Apr 1;29(3):326–35.

248. Boby Chu, Rosaire Mongrain, Richard Leask, Olivier Bertrand. Stented coronary artery phantom for particle image velocimetry. CMBES Proc [Internet]. 2007 Dec 31 [cited 2020 Jan 12];30(1).
Available from: https://proceedings.cmbes.ca/index.php/proceedings/article/view/132

249. Yunker BE, Cordes D, Scherzinger AL, Dodd GD, Shandas R, Feng Y, et al. An investigation of industrial molding compounds for use in 3D ultrasound, MRI, and CT imaging phantoms. Med Phys [Internet]. 2013 May [cited 2019 Sep 3];40(5). Available from: https://www.ncbi.nlm.nih.gov/pmc/articles/PMC3651250/

250. Stepniak K, Ursani A, Paul N, Naguib H. Development of a phantom network for optimization of coronary artery disease imaging using computed tomography. Biomed Phys Eng Express. 2019 Jun;5(4):045019.

251. Roehmbauer B. Mathematical and experimental development oftwo different stent models for PlV application. [Montreal, Canada]: Department of Mechanical Engineering, Mcgill University; 2005.

252. Klein A. Segmentation and motion estimation of stent grafts in abdominal aortic aneurysms. 2011 Nov 22 [cited 2019 Aug 20]; Available from: https://research.utwente.nl/en/publications/segmentation-and-motion-estimation-of-stent-grafts-in-abdominal-a

253. van Prehn J, Schlösser FJV, Muhs BE, Verhagen HJM, Moll FL, van Herwaarden JA. Oversizing of aortic stent grafts for abdominal aneurysm repair: a systematic review of the benefits and risks. Eur J Vasc Endovasc Surg. 2009 Jul 1;38(1):42–53.

254. Kosukegawa H, Fridrici V, Kapsa P, Sutou Y, Adachi K, Ohta M. Friction properties of medical metallic alloys on soft tissue–mimicking poly(vinyl alcohol) hydrogel biomodel. Tribol Lett. 2013 Sep 1;51(3):311–21.

255. Niemczyk A, Fray ME, Franklin SE. Friction behaviour of hydrophilic lubricious coatings for medical device applications. Tribol Int. 2015;Complete(89):54–61.

256. Chen T, Lancaster M, Lin DSY, Doyle MG, Forbes TL, Amon CH. Measurement of frictional properties of aortic stent grafts and their delivery systems. J Med Devices [Internet]. 2019 Jun 1 [cited 2019 Sep 4];13(2). Available from: /medicaldevices/article/13/2/021008/727280/Measurement-of-Frictional-Properties-of-Aortic

257. Kontopodis N, Metaxa E, Pagonidis K, Ioannou C, Papaharilaou Y. Deformation and distensibility distribution along the abdominal aorta in the presence of aneurysmal dilatation. J Cardiovasc Surg (Torino). 2017 Feb;58(1):72–9.

258. Zha Y, Peng G, Li L, Yang C, Lu X, Peng Z. Quantitative aortic distensibility measurement using ct in patients with abdominal aortic aneurysm: reproducibility and clinical relevance. BioMed Res Int [Internet]. 2017 [cited 2019 Sep 4];2017. Available from: https://www.ncbi.nlm.nih.gov/pmc/articles/PMC5412143/

259. Gindre J, Bel-Brunon A, Rochette M, Lucas A, Kaladji A, Haigron P, et al. Patient-specific finite-element simulation of the insertion of guidewire during an evar procedure: guidewire position prediction validation on 28 cases. IEEE Trans Biomed Eng. 2017;64(5):1057–66.

260. Liu Y, Dang C, Garcia M, Gregersen H, Kassab GS. Surrounding tissues affect the passive mechanics of the vessel wall: theory and experiment. Am J Physiol Heart Circ Physiol. 2007 Dec;293(6):H3290-3300.

261. Gong JP. Friction and lubrication of hydrogels—its richness and complexity. Soft Matter. 2006 Jun 20;2(7):544–52.